Localized compliance of airways, applied to respiratory flow of patient with obstructive airway diseases

Toshihiro SERA

A Thesis Submitted for the Doctor of Philosophy Degree
in Graduate School of Science and Technology at Keio University

2003

Abstracts

Airway consists of a number of various compliant tubes from trachea to alveolus and airway compliance is very important factor in pulmonary dynamics and clinical application. This thesis focused on the localized compliance of airway, especially trachea and small airways, and applied to respiratory flow of patient with tracheostenosis. Since trachea is anatomical dead space and tracheal flow is much related to airways resistance, it is important to understand flow structure associated with the localized compliance of trachea. And the airway abnormality (surfactant abnormality and the deposition of fibrous tissue) occurs at small airways, and so the localized compliance of small airways itself has many clinical implications. To evaluate the localized compliance of small airways, especially, novel method to visualize small airways under near physiological conditions was developed.

A trachea primarily consists of tracheal cartilage rings and smooth muscle. Trachea of pigs was immersed in a saline solution, and the maximum deformations of tracheal cartilage rings and tracheal smooth muscle were measured by a laser displacement meter. Young’s modulus of tracheal cartilage rings (E_{TC}) and tracheal smooth muscle (E_{TS}) were determined based on the mechanical models and assuming the linear relationship of the pressure – deflection curve. The model for the deformation of smooth muscle is based on large deflections of uniformly distributed loaded rectangular plates with clamped edges, and the model for the deformation of cartilage rings is based on part of a cylindrical shell being supported along the edges and exposed to a uniformly distributed load normal to the surface. E_{TC} and E_{TS} were 5.8 ± 2.9 MPa and 0.65 ± 0.32 MPa, respectively.

To visualize and analyze the three-dimensional structure of the small airways that were embedded in parenchyma without dehydration and fixation, a two-step method was developed to visualize small airways in detail by staining the lung tissue with a radiopaque solution and then

visualizing the tissue with a cone-beam microfocal X-ray CT (Computed Tomography) system. To verify the applicability of this staining and CT imaging (SCT) method, the method was used to visualize small airways in excised rat lungs. By using the SCT method to obtain continuous CT images, three-dimensional branching and merging bronchi ranging from 500 μm to 150 μm (the airway generation (***Z***) = 8 ~ 16) were successfully reconstructed. And, the morphometry of the small airways (diameter, length, branching angle and gravity angle between the gravity direction and airway vector) was analyzed using the three-dimensional thinning algorithm. The SCT method is the first reported method that yields faithful high-resolution images of soft tissue geometry without fixation, and the three-dimensional morphometry of small airways is useful for studying the biomechanical dynamics in small airways.

Localized compliance of small airways was evaluated under “near” physiological conditions. The SCT method was used to analyze the changes in the diameter and length of the same small airways (~ 150 μm diameter) and then evaluated the localized compliance as a function of ***Z***. At smaller airways (D < 300 μm), compared with the diameter and length of the small airways at functional residual capacity (FRC), the diameter was 36% larger at end tidal inspiration (TV) and 89% at total lung capacity (TLC), and the length was 18% larger at TV and 43% at TLC. The diameter, especially at smaller airways, did not behave linearly with $(lung\ volume)^{1/3}$. With increasing lung pressure, the diameter changed dramatically at a particular pressure and the length changed approximately linearly during both inflation and deflation. The percentage of airway volume for the smaller airways did not behave linearly with that of lung volume. Smaller airways were generally more compliant than the larger airways with increasing ***Z*** and exhibited hysteresis in their diameter behavior. Compared with airways at lower ***Z***, those at higher ***Z*** deformed at a lower pressure. These results indicated that the smaller airways did not behave homogenously. Traditionally, the airflow is approximately zero and gas transport is dominated by simple diffusion. However these dramatic deformations of small airways during respiration may promote

complicated diffusion.

To investigate the effects of tracheal compliance on respiratory flow and, the flow fields in a mechanical realistic tracheostenosis model was clarified by using laser-Doppler velocimeter measurements. Spatial variation of wall distensibility was achieved in the model by varying the wall thickness based on the elastic modulus measured in pig airways. The shape of the model was based on CT images of a patient that had tracheostenosis. The spatial variation influenced the flow in the airway and the turbulence production rate decreased faster at smooth muscles due to the deformation of cross sections. Using the model, the mechanism of wheeze generation was discussed by focusing on the turbulence intensity. The respiratory sound, especially “wheezes”, is commonly related to obstructive airway diseases, and this generation is related to wall vibration and to flow structure around stenosis. The turbulence intensity in expiratory flow was about twice that in inspiratory flow, and larger vortices existed in post-stenosis in expiratory flow, and thus might contribute to wheeze generation.

Acknowledgements

First of all, I would like to thank my supervisor, Prof. Kazuo TANISHITA, for his encouragement and guidance during my research. He is remarkably generous with his time and wonderful knowledge, and teaches me the academic life.

I appreciate that Prof. Yutaka TOMITA, Assistant Prof. Takashi MAENO, Assistant Prof Shinnosuke OBI, and Assistant Prof. Kotaro OKA gave me many valuable comments and suggestions toward my thesis. Their comments were insightful, and have been very helpful to clarify the thesis.

I would like to thank Prof. Koichi KOBAYASHI and Assistant Prof. Hirohisa HORINOUCHI. They provided CT images of patient and discussed the lung sounds in chapter 5. I would also like to thank Prof. Robert SCHROTER for his professional advice in chapter 3 and 4. I appreciate the time and effort spent to discuss the lung compliance and review my manuscripts.

I am grateful to Dr. Hideki FUJIOKA. He visualized small airways using micro-CT and developed the software. I would also like to thank Dr. Hideo YOKOTA, Dr. Akitake MAKINOUCHI, Dr. Ryutaro HIMENO and the other members of Advanced Computed Center, Institute of Physical and Chemical Research (RIKEN) for their help and support during my experiments of micro- CT in chapter 3 and 4. I also thank Mr. Satoh for his effort to measure flow structure around stenosis in chapter 2 and 5.

I am grateful to the members of Tanishita Laboratory for their moral support and constructive discussion. The friendly atmosphere in the laboratory makes my academic life a very enjoyable time.

Finally, I would like to express my gratitude to my dearest friend Tomoko NISHIDA and to my parents for many years of encouragement and support.

Contents

List of Tables and Figures

List of Abbreviations and Symbols

a: radius of trachea

As: asymmetry of bifurcation

C: localized compliance

D: diameter of small airways

d_{TS}: maximum deflection of tracheal smooth muscle

d_{TC}: maximum deflection of a tracheal cartilage ring

E_{TC}: Young’s modulus of tracheal cartilage rings

E_{TS}: Young’s modulus of tracheal smooth muscle

h: wall thickness

h_0: surfactant layer thickness

k: square of wave speed ratio

L: length of small airways

M: ratio of wall mass to fluid mass

N: number of samples for velocity measurement

n: refractive index

P: lung pressure

Ptp: transmural pressure

q: uniformly distributed load on trachea

r: radial coordinate

S: axial position for the velocity measurement

u: secondary -averaged velocity component

$\grave{u}_{rms}$: secondary turbulence intensity

u: major axis of tracheal smooth muscle

V: lung volume

v: minor axis of tracheal smooth muscle

w: axial averaged velocity component

$\hat{W}$: amplitude of the average cross-section axial velocity

$\grave{w}_{rms}$: axial turbulence intensity

$\boldsymbol{Z}$: airway generation (counting the number of bifurcations from trachea)

z: axial coordinate

α: branching angle

β: gravity angle (between the gravity direction and airway vector)

δ_D: ratio of diameter increase

δ_L: ratio of length increase

ϕ: angle of the tracheal cartilage rings

γ: Poisson's ratio (= 0.5)

ν: kinematic viscosity

ρ: density of fluid

ρ_0: density of tracheal wall

Subscripts

0: trachea (Horsfield branching No. 1)

1: left main bronchus (No. 2)

10: right main bronchus (No. 10)

FRC: functional residual capacity

RV: residual volume

SCT: staining and CT imaging

TC: tracheal cartilage rings

TLC: total lung capacity

TS: tracheal smooth muscle

TV: sum of FRC and tidal volume (at end tidal inspiration)

VC: vital capacity

Vt: tidal volume

Chapter 1

General Introduction

1.1 Mechanism of Respiration

The primary function of the lung is gas exchange; it allows oxygen to move from air into blood in inspiration and carbon dioxide to move out in deflation, and oxygen and carbon dioxide move between alveolar wall and pulmonary capillary by simple diffusion. One of the most important factors during respiration is lung compliance. During inspiration the diaphragm is contracted and moves downward and the ribs are lifted, and so the lung expands and intrathoracic pressure falls. And so air is inspired. During expiration, reversely, the diaphragm relaxes and returns the equilibrium position, and so the lung contracts. And so air is passively expired.

The lung is divided conceptually into air containing volumes that describe the state of the lung under different conditions (Fig. 1-1). The sinusoidal curve represents the volume change during quiet breathing, called as the tidal volume (Vt). It is then the volume of air exhaled per one respiratory cycle. The gas remaining in the lung at the end of a normal tidal expiration is called Functional Residual Capacity (FRC), and that in the lung at the end of the maximal expiration is termed Residual Volume (RV). The volume at the end of a fully inflation is called as Total Lung Capacity (TLC), and the difference between TLC and RV is called as the Vital Capacity (VC).

1.2 Airway Structure

Pulmonary airways consist of tapered, curved, branching tubes of a range of length and diameter, which become narrower, shorter, and more numerous as they penetrate deeper into the lung (Fig. 1-2). The trachea divides into right and left main bronchi, which in turn bifurcate into lobe, then segmental bronchi. This process continues down to the terminal bronchioles, which are the smallest airways without alveoli. All of these bronchi make up the conducting airways. Their function is to lead inspired air to the gas exchanging regions of the lung (Fig. 1-3). Because the conducting airways contain no alveoli and therefore take no part in gas exchange, they constitute the anatomic dead space. Its volume is about 150 ml. The terminal bronchioles divide into respiratory bronchioles, which have occasional alveoli. Finally the respiratory bronchioles divide into the alveolar ducts, which are completely lined with alveoli. These regions where the gas exchange occurs are called as the respiratory zone, which makes up most of the lung, its volume being about 2.5 to 3 l.

It is well known that these complex branching networks affect the flow structure and gas transport, and so the airway morphometry has been studied for many years.

1.2.1 *Central Airways*

Airway geometry has been studied using measurements of mammalian-lung cast models (Weibel, 1963; Horsfield et al., 1971; Phalen et al., 1978). Models of the branching geometries from careful anatomical measurements include the symmetrical network of Weibel (1963) and the asymmetrical network of Horsfield et al. (1971). Weibel (1963) counted the number of bifurcations downward, beginning with the trachea as generation, then allowing the branching tree to evolve and plotted the mean diameter per generation and derived the following diameter-generation number relationship:

$$D(\boldsymbol{Z}) = D(0) \cdot 2^{-\boldsymbol{Z}/3}$$

where $D(\boldsymbol{Z})$ is the mean airway diameter in generation $\boldsymbol{Z}$. Horsfield et al. (1971) began at the terminal generations and ordered the airways by converging orders upward, considering the airways in the sense of a confluent river system. And they presented the branching angles and curvature ratio of central airways. These anatomical structures are expressed as the two-dimensional (non-planar) data. However the pulmonary dynamics strongly depends on the asymmetry and non-planarity of the bifurcation (Nishida et al., 1997; Comer et al., 2000; Caro et al., 2002). Recently Sauret et al. (2002) reported the three-dimensional geometry of the human conducting airways (***Z*** = 1 ~ 9) from computed tomographic (CT) images using the three-dimensional thinning (skeletonization) algorithm.

1.2.2 *Small Airways*

Small Airways are end of conducting zone (terminal bronchiole) and first of transitional zone (respiratory bronchiole) (Fig. 1-3). Analyzing the three-dimensional structure of small airways is difficult, and therefore various techniques have been used. Hammersley and Olson (1992) investigated the geometry of small airways of human using the cast model technique. Kriete et al. (2001) sliced the fixated lungs of rat and mouse into 70 μm thick and then visualized alveolar ducts and alveoli using a confocal laser scan microscope and microfocal CT system (micro-CT) (Fig. 1-4). While the imaging of airways radiographically involves insufflating the airways with a metal dust such as tantalum (Hughes et al., 1972; Naureckas et al., 1994), it is difficult to coat the small airway surfaces uniformly.

However, previous techniques, such as the cast model technique, deform the geometry during sample preparation. Moreover, small airways are flexible tissue, and thus their geometry varies markedly during respiration (Naureckas et al. 1994). Therefore, a visualization technique of small-airway geometry is needed so that identifies the airways in *in situ* conditions.

1.3 Lung Compliance

Lung compliance is one of the most important factors to understand lung mechanics. The compliance is an index of the elastic recoil of lung and determined by tissue elasticity and surface tension. The surface tension is determined by "pulmonary surfactant". Surfactant, which is composed of approximately 90% phospholipid, and dipalmitoyl phosphatidylcholine (DPPC) and 10% specific surfactant protein, is synthesized and secreted by type II pneumocytes and present in the fluid lining the surface of airways. The physiological advantage is to lead a low surface tension and so increases the lung compliance and promotes the lung stability. Furthermore lung compliance is a clinical diagnosis index. For example, acute respiratory distress syndrome is associated with the surfactant abnormality and airways collapse (Mason, 1987) and chronic airways inflammation is associated with the deposition of fibrous tissue (collagen and elastin) within airway wall (Mullen et al., 1985; Bosken et al., 1990). And the wall thickness of patients with asthma was thicker, and so their lung is less compliant (Roche, 1998; Niimi et al., 2000; Little et al., 2002; Corsico et al., 2003).

1.3.1 *Macroscopic Compliance*

Pressure–volume (*P*-*V*) curve (Fig. 1-5) is the simplest method to analyze the lung compliance macroscopically. Generally the overall compliance is determined by the gradient ($\Delta V/\Delta P$) of the *P*-*V* curve based on the relation between lung pressure and lung volume. And *P*-*V* curves that the lung follows during inflation and deflation are different, which is known as hysteresis. The lung volume at any pressure during inflation is larger than during deflation.

The important factor in *P*-*V* behavior is the surface tension. The lungs inflated with saline have a much larger compliance than the air-filled lungs, and don't exhibit hysteresis (Fig. 1-5). Because the saline abolished the surface tension forces, this observation meant that surface tension contributed a large part of the recoil force of the lung.

1.3.2 Localized *Compliance*

Airways consist of a number of various compliant tubes from trachea to alveolus. Table 1-1 shows the summary of airway wall structure and Fig. 1-6 shows the schematic wall structures of bronchus and bronchiole. Especially, bronchiole did not have cartilage. And the thickness of airway liquid is variable in airways. Jarayaman et al. (2001) developed novel fluorescent probes and microscopy methods to measure the thickness *in vivo* and reported that the depth in isolated human main bronchi was 55 ± 5 μm. And it is known that the depth at small airways is approximately 10 μm (Widdicombe JH. 2002). To evaluate respiratory function in detail, not only the macroscopic compliance but also the more localized compliance based on microscopic regions of airways needs to be determined. The localized compliance is an important factor to understand the pulmonary dynamics as well as a clinical index. Especially, this thesis focused on the trachea and small airways.

Trachea primarily consists of two different types of tissues: cartilage rings and smooth muscle (Fig. 1-7A). Cartilage rings form horseshoe-shaped structures in the cross-section and are stiffer than tracheal smooth muscles. The purpose of cartilage rings is to maintain the lumen and to resist airway collapse during maximal expiratory flow and during coughs. The muscles are used to vary the lumen of airways by constriction and relaxation. Trachea does not take part in gas exchange (anatomical dead space) and flow structure in trachea is much related to airway resistance, and so the mechanical properties (Young’s modulus) are studied for many years. Recent studies (James et al., 1987; Ishida et al., 1990; Art and Lekeux, 1991; Mitchell et al., 1999) on these mechanical properties revealed a relationship between the cross-section area of the trachea and transmural pressure in the trachea and this relationship determined the compliance of the trachea.

Small airways primarily consist of smooth muscle, not cartilage (Fig. 1-7B). Although the airway abnormality (surfactant abnormality and the deposition of fibrous tissue) occurs at microscopic level of a lung (bronchi and bronchiole) (Roche, 1998; Shaw et al., 2002; Taskin, 2002; Wright, 2002) (Fig. 1-8), it is difficult to detect small airway obstruction by the usual lung function tests (Macklem, 1998). In many respiratory diseases, significant compliance abnormalities mainly occur in localized regions of bronchi and bronchioles, and thus in addition to the overall compliance, the localized compliance of both parenchyma and small bronchi or bronchioles based on small scale observations must be identified. The technique of analyzing the localized compliance was developed about 30 years ago. Previously tantalum powder is insufflated into a lung as a contrast agent and the diameter and length changes of bronchial segments are analyzed from the bronchograms at various transmural pressures (Hughes et al., 1972; Menkes et al., 1972; Sittipong and Hyatt, 1974). However this measurement was limited to large bronchi over 1 mm. Previously to analyze the mechanical properties of the small airways, two methods were developed. One method was to visualize the dehydrated and fixated preparations using a microscope (Klingele and Staub, 1971; Okazawa et al., 2000). However, the preparation procedure significantly deforms the sample tissue, and observing the morphometric changes of the same airways at various lung volumes is extremely difficult. The other approach is to measure the mechanical properties of excised small airway segments *in vitro* (Tiddeens et al. 1999). However, *in situ*, the intrapulmonay airways are surrounded by lung parenchyma, and the effective microscopic airway compliance is influenced by the surrounding support (Fig. 1-7B). Hyatt and Flath (1966) and Takashima et al. (1975) reported that the microscopic compliance of small airways was influenced with lung parenchyma and that the intact airways are stiffer than the isolated airways.

1.5 Objectives

This thesis focused on localized compliance of airways, especially trachea and small airways. The localized compliance is a very important factor in physiological application and pulmonary dynamics, such as airway dynamics (Heil, 1999), airflow structure (Liu et al., 2002), aerosol deposition (Comer et al., 2000; Zhang et al., 2001) and surfactant delivery (Zhang et al., 2003). These dynamics can be clarified by *in situ* analysis of their physiological geometry and compliance.

Trachea, especially, consists of two different types of tissues: cartilage rings and smooth muscle, and this spatial variation of wall compliance affects the flow structure in trachea, which is much associated with airway resistance. Moreover respiratory diseases occur most frequently at small airways (Tashkin 2002), and then the localized compliance of small airways has clinical implications. Small airways are flexible tissue, and thus their geometry varies markedly during respiration (Naureckas et al. 1994). Therefore, a visualization technique of small-airway geometry is needed so that identifies the airways in *in situ* conditions.

Chapter 2 focused on the tracheal compliance. The Young's modulus of cartilage rings and smooth muscle were analyzed. In chapter 3, novel method to visualize small airways under "near" physiological condition without dehydration and fixation is presented. In chapter 4, using the novel visualization technique, the morphometric changes (length and diameter behavior) of small airways were measured during a stepwise inflation and deflation process, and the localized compliance of small airways (~ 150 μm diameter) were evaluated as a function of airway generation ($\boldsymbol{Z}$). Finally, chapter 5 focused on respiratory flow of patient with tracheostenosis to investigate the effects of tracheal compliance.

Table 1-1 The characteristics of airway wall structures.

	Trachea	Bronchus	Bronchiole	Respiratory Bronchiole
Goblet Cells	+++	++	+	Absent
Clara Cells	Absent	Absent	+	+
Muscularis mucosae	Absent	+	+++	+++
Mucous glands	+++	++	Absent	Absent
Cartilage	+++	++	Absent	Absent
Alveoli	Absent	Absent	Absent	+

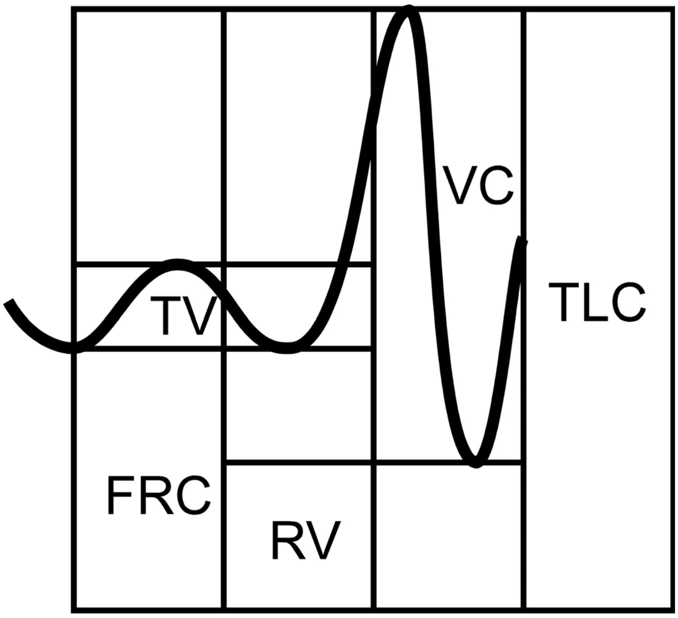

Fig. 1-1 Schematic diagram of the physiological lung volumes. (TV: tidal volume, FRC: functional residual capacity, RV: residual volume, VC: vital volume, TLC: total lung capacity)

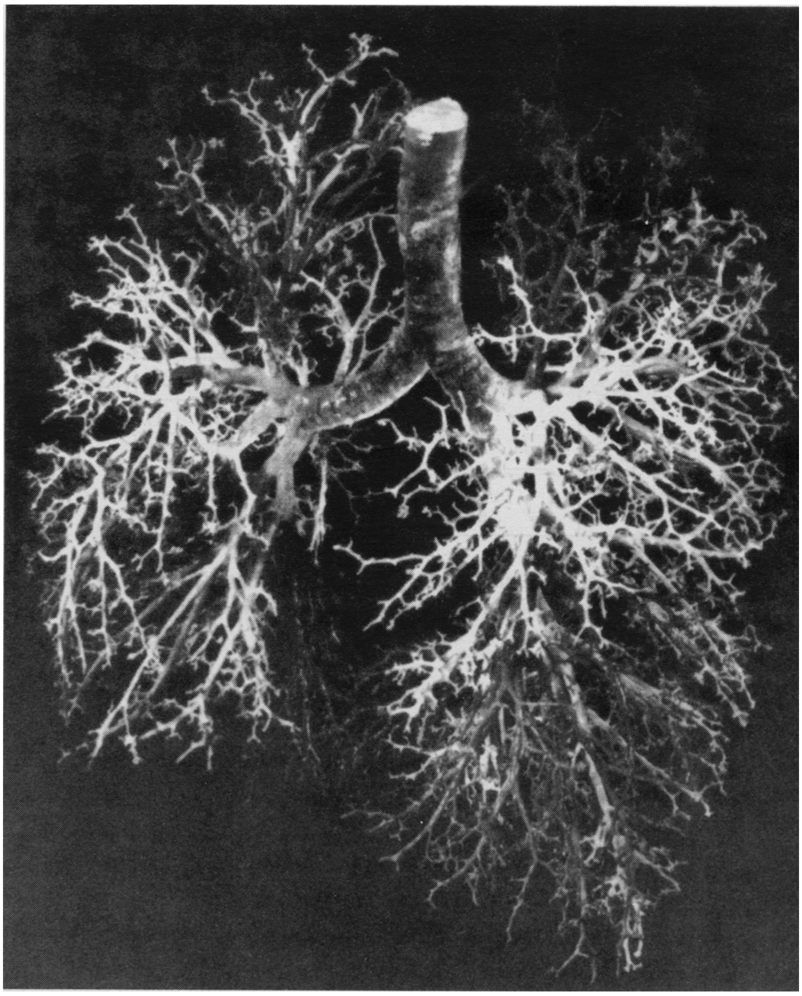

Fig. 1-2 Cast of the airways of a human lung. The conducting airways from trachea to the terminal bronchioles are seen. (West. 1999)

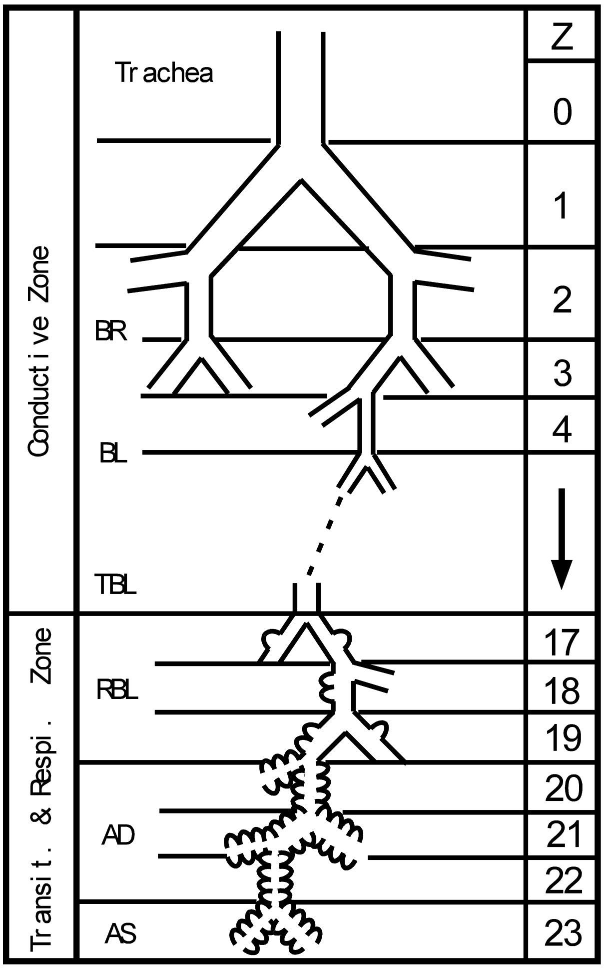

Fig. 1-3 Idealization of the human airways according to Weibel. The first 16 generations (***Z***) make up the conducting airways, and the last 7 generations, the transitional and respiratory zone. (Webel, 1963)

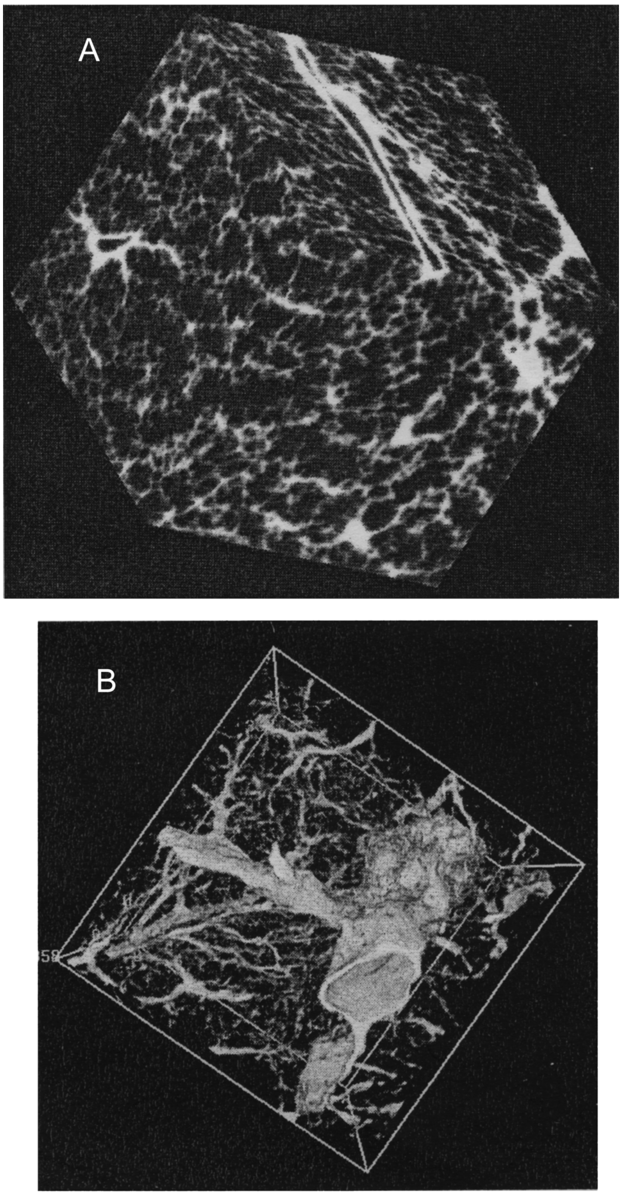

Fig. 1-4 Three dimensional structure of the human lung using (A) a confocal microscopy and (B) a microfocal X-ray tomography. The side length of the cube is about 5mm. (Kriete et al., 2001)

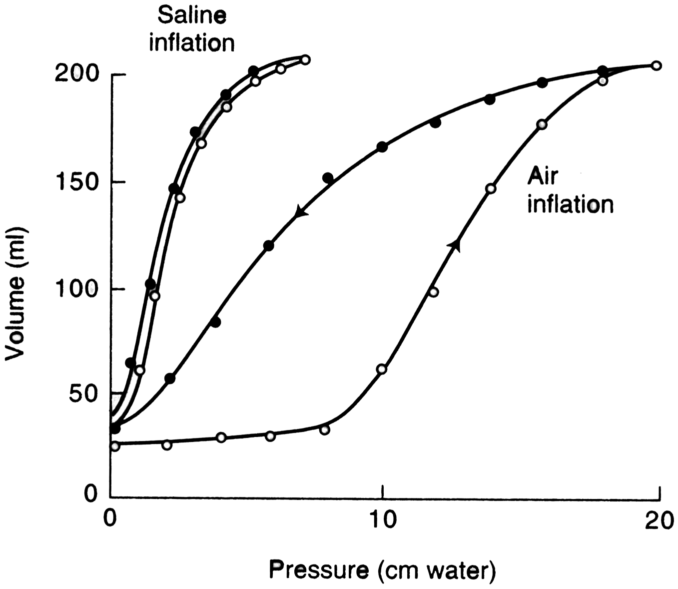

Fig. 1-5 Comparison of pressure – volume curve of air-filled and saline-filled lungs. Open circles: inflation, closed circles: deflation. (West, 1999)

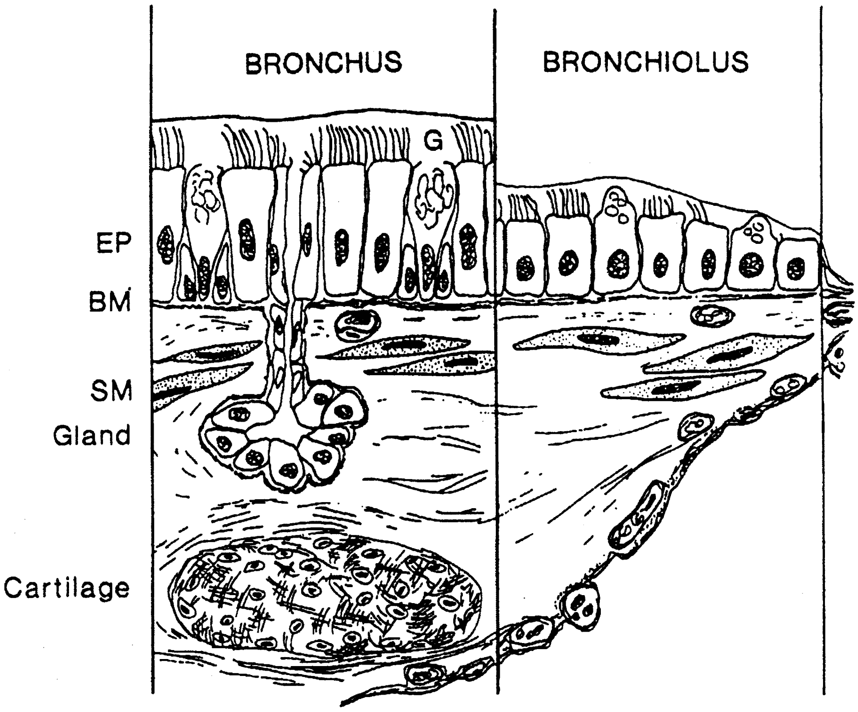

Fig. 1-6 The schematic wall structures of bronchus and bronchiole. (EP: epithelium, BM: basement membrane, SM: smooth muscle) (Kamm, 1999)

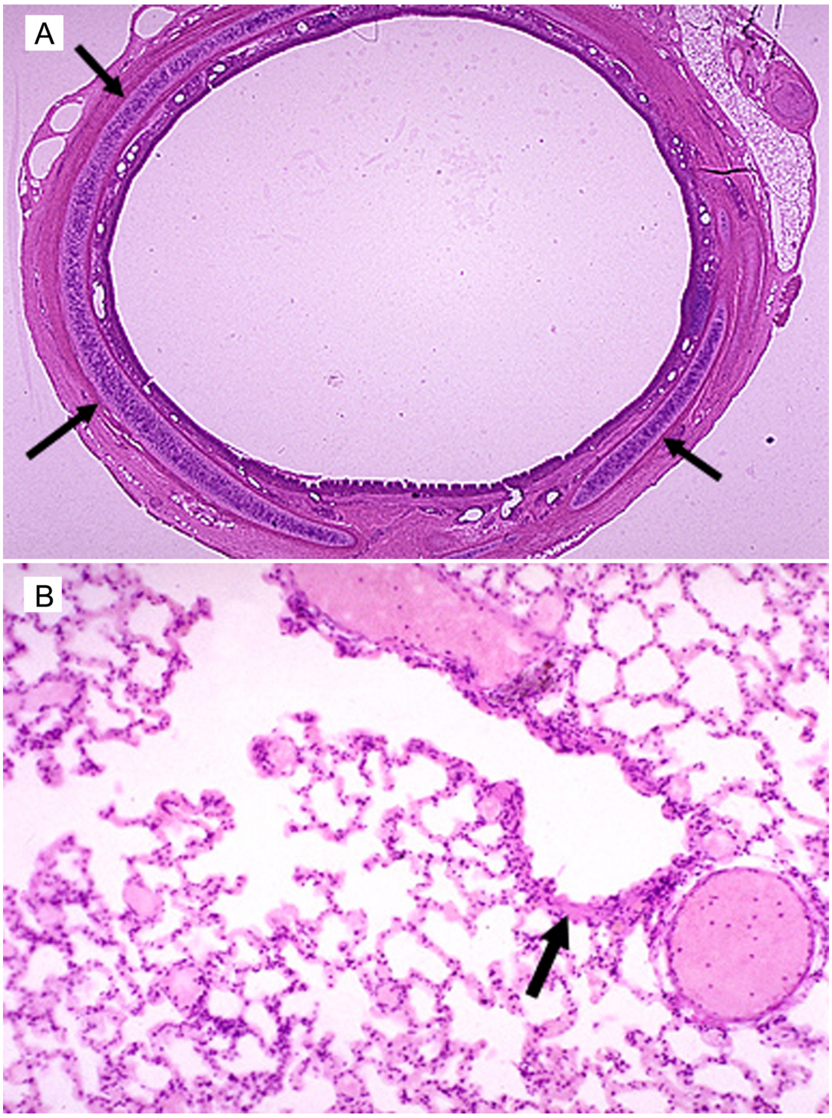

Fig. 1-7 Airway wall structures. A: trachea has cartilage (arrows) and smooth muscle, and B: small airway (arrow) has muscle but no cartilage in its wall.
(http://www.hms.harvard.edu/societies/castle/Room166/bodyblock/histology.)

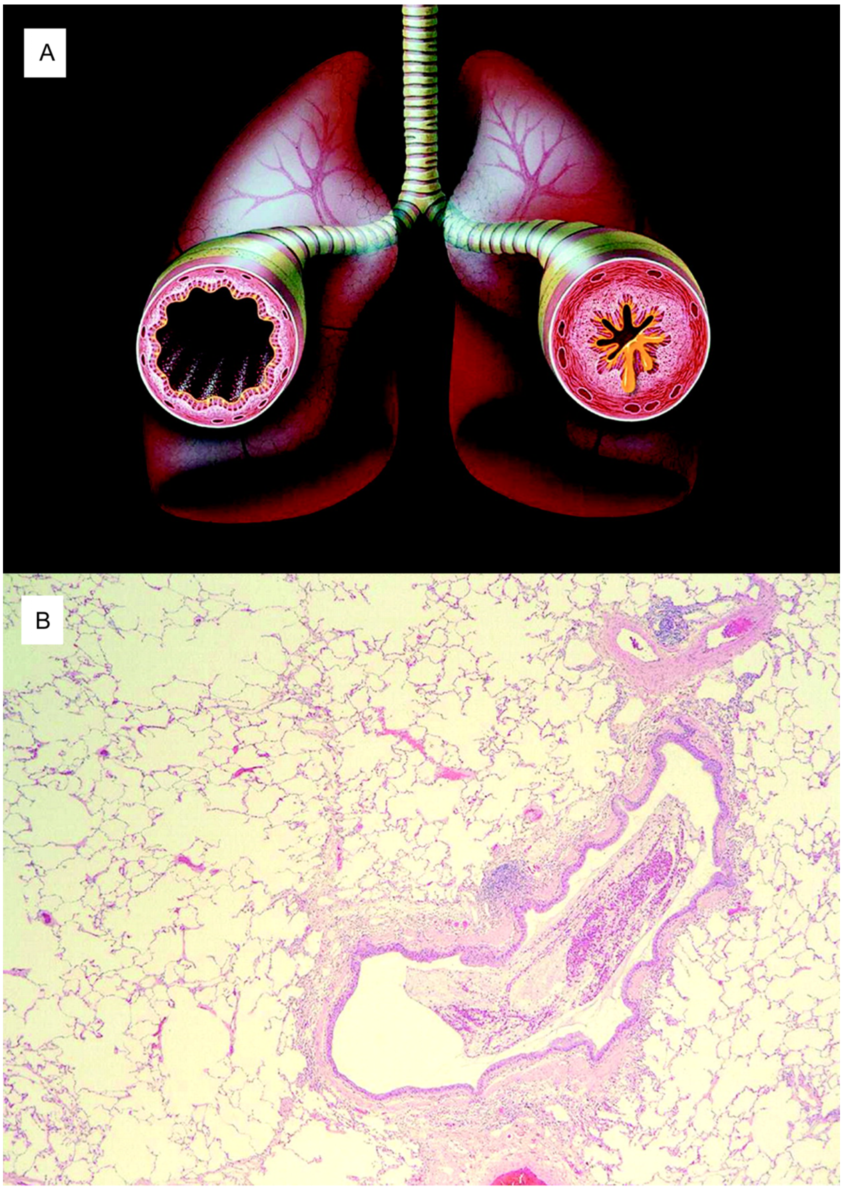

Fig. 1-8   Structural changes in small airways in asthma.
A: Schematic of small airway in the normal lung (left) and in asthma (right), and B: photograph of small airways in a case of asthma eosinophilic plugging, associated with inflammation and thickening of the airways wall. (Jeffery, 2001)

Reference

Art T, and Lekeux P. Mechanical properties of the isolated equine trachea. Res. Vet. Sci 51, 55-60, 1991.

Bosken CH, Wiggs BR, Paré PD, and Hogg JC. Small airway dimensions in smokers with obstruction to airflow. Am Rev Respir Dis 1142: 563-70, 1990.

Caro C, Schroter R, Watkins N, Sherwin S, and Sauret V. Inspiratory flow in bronchial airway models: bifurcation plane rotation. In Proceeding of the 4th World Congress of Biomechanics Calgary, 2002.

Comer JK, Kleinstreuer C, Hyun S, and Kim CS. Aerosol transport and deposition in sequentially bifurcating airways. J Biomech Eng 122(2), 152-158, 2000.

Corsico A, Milanese M, Baraldo S, Casoni GL, Papi A, Riccio AM, Cerveri I, Saetta M, and Brusasco V. Small airway morphology and lung function in the transition from normality to chronic airway obstruction. J Appl Physiol 95, 441-7, 2003.

Hammersley JR, and Olson DE. Physical models of the smaller pulmonary airways. J Appl Physiol 72(6), 2402-2414, 1992.

Heil M. Airway closure: occluding liquid bridges in strongly buckled elastic tubes. J Biomech Eng 121(5), 487-483, 1999.

Horsfield K, Dart G, Olson DE, Filly GF, and Cumming G. Models of the human bronchial tree. J Appl Physiol 31(2), 207-217, 1971.

Hughes JM, Hoppin FG Jr, and Wilson AG. Use of stereoscopic x-ray pairs for measurements of airway length and diameter in situ. Br J Radiol 45(535), 477-485, 1972.

Hyatt RE, and Flath RE. Influence of lung parenchyma on pressure-diameter behavior of dog bronchi. J Appl Physiol 21(5), 1448-1452, 1965.

Ishida K, Paré PD, Blogg T, and Schellenberg RR. Effects of elastic loading on porcine tracheal muscle mechanics. J Appl Physiol 69, 1033-1039, 1990.

James AL, Paré PD, Moreno RH, and Hogg JC. Quantitative measurement of smooth muscle shortening in isolated pig trachea. J Appl Physiol 63, 1360-1365, 1987.

Jayaraman S, Song Y, Vetrivel L, Shankar L, and Verkman AS. Noninvasive in vivo fluorescence measurement of airway-surface liquid depth, salt concentration, and pH. J. Clin. Invest 107, 317-324, 2001.

Jeffery PK. Remodeling in asthma and chronic obstructive lung disease. Am J Respir Crit Care Med 164, S28-S38, 2001.

Kamm RD, Airway wall mechanics. Annu. Rev. Biomed. Eng 1, 47-72, 1999.

Klingele TG, and Staub NC. Terminal bronchiole diameter changes with volume in isolated, air-filled lobes of cat lung. J Appl Physiol 30(2), 224-227, 1971.

Kriete A, Breithecker A, and Rau W. 3D imaging of lung tissue by confocal microscopy and micro-CT. In Proceedings of The International Society for Optical Engineering 4257, 469-476, 2001.

Little SA, Sproule MW, Cowan MD, Macleod KJ, Robertson M, Love JG, Chalmers GW, McSharry CP, and Thomson NC. High resolution computed tomographic assessment of airway wall thickness in chronic asthma: reproducibility and relationship with lung function and severity. Thorax 57(3). 247-253, 2002.

Liu Y, So RM and Zhang CH. Modeling the bifurcating flow in a human lung airway. J Biomech 35(4), 465-73, 2002.

Mason RJ. Surfactant in adult respiratory distress syndrome. Eur J Respir Dis Suppl 153, 229-36, 1987.

Macklem PT. The Physiology of Small Airways. Am. J. Respir. Crit. Care Med 157(5), S181-S183, 1998.

Menkes H, Gamsu G, Schroter R, Macklem PT. Interdependence of lung units in isolated dog lungs. J Appl Physiol 32(5): p. 675-80, 1972.

Mitchell HW, Turner DJ, Gray PR, and Mcfawn PK. Compliance and stability of the bronchial wall in a model of allergen-induced lung inflammation. J Appl Physiol 86, 932-937, 1999.

Mullen JB, Wright JL, Wiggs BR, Paré PD, and Hogg JC. Reassessment of inflammation of airways in chronic bronchitis. Br Med J 291, 1235-1239, 1985.

Naureckas E.T., Dawson C.A., Gerber B.S., Gaver III D.P., Gerber H.L., Linehan J.H., Solway J, and Samsel RW, Airway reopening pressure in isolated rat lungs. J Appl Physiol 76(3), 1372-1377, 1994.

Niimi A, Matsumoto H, Amitani R, Nakano Y, Mishima M, Minakuchi M, Nishimura K, Itoh H, and Izumi T. Airway wall thickness in asthma assessed by computed tomography. Relation to clinical indices. Am J Respir Crit Care Med 162(4), 1518-23, 2000.

Nishida M, Inaba Y, and Tanishta K. Gas dispersion in a model pulmonary bifurcation during oscillatory flow. J Biomech Eng 119, 309-316. 1997.

Okazawa M, Paré PD, and Lambert RK. Compliance of peripheral airways deduced from morphometry. J Appl Physiol 89, 2373-2381, 2000.

Phalen RF, Yeh HC, Schum GM, Raabe OG. Application of an idealized model to morphometry of the mammalian tracheobronchial tree. Anatomical Record 190(2), 167-176, 1978.

Roche WR. Inflammatory and Structural Changes in the Small Airways in Bronchial Asthma. Am Rev Respir Dis 157, S191-S194, 1998.

Sauret V, Halson PM, Brown IW, Fleming JS, and Baily AG. Study of the three-dimensional geometry of the central conducting airways in man using computed tomographic (CT) images. Journal of Anatomy 200, 123-134, 2002.

Shaw RJ, Djukanovic R, Tashkin DP, Millar AB, du Bois RM, and Orr PA. The role of small airways in lung disease. Respir Med 96(2):67-80, 2002.

Sittipong R, and Hyatt RE. Static mechanical behavior of bronchi in excised dog lung. J Appl Physiol 37(2) 201-206, 1974.

Takishima T, Sasaki H, and Sasaki T. Influence of lung parenchyma on collapsibility of dog bronchi. J Appl Physiol 38(5), 875-881, 1975.

Tashkin DP. The role of small airway inflammation in asthma. Allergy and Asthma Proceedings 23(4), 233-242, 2002.

Tiddens HA, Hofhuis W, Bogaard JM, Hop WC, de Bruin H, Willems LN, and de Jongste JC. Compliance, hysteresis, and collapsibility of human small airways. Am J Respir Crit Care Med 160, 1110-1118, 1999.

Weibel ER. Morphometry of the Human lung. New York: Academic, 136-143, 1963.

West JB. Respiratory Physiology –The essentials. Lippincott Williams & Wilkins, 2000.

Widdicombe JH. Regulation of the depth and composition of airway surface liquid. J Anat 201(4), 313-8, 2002.

Wright JL. Diseases of the small airways. Lung 179, 375-396, Springer-Verlag, NY, 2002.

Zhang YL, Matar OK, and Craster RV. A theoretical study of chemical delivery within the lung using exogenous surfactant. Med Eng Phys 25(2), 115-132, 2003.

Zhang Z, Kleinstreuer C, and Kim CS. Effects of curved inlet tubes on air flow and particle deposition in bifurcating lung models. J Biomech 34(5), 659-69, 2001.

Chapter 2

Measurements of Tracheal Compliance

2-1 Introduction

A trachea primarily consists of two different types of tissues: cartilage rings and smooth muscle (Figs. 1-7 and 2-1). In central airways, such as trachea and main bronchi, it is important to understand the mechanical property as the localized compliance, because these airways do not take part in gas exchange (anatomical dead space) and the flow structure in trachea is much related to airways resistance. The mechanical properties (Young's modulus) are useful to investigate flow structure in airways. Recent studies (James et al., 1987; Ishida et al., 1990; Art and Lekeux, 1991; Mitchell et al., 1999) on these mechanical properties revealed a relationship between the cross-section area of the trachea and transmural pressure in the trachea and this relationship determined the compliance of the trachea. Although such analysis helps clarify these mechanical properties, fundamental data on distensibility of cartilage rings and smooth muscle, such as Young's modulus, is still not accurately known. In this chapter, therefore, the Young's modulus of cartilage rings and smooth muscle were measured by using pig trachea directly.

2.2 Materials and Methods

2.2.1 *Measurement of Wall Distensibility*

Nine pig trachea were purchased from a slaughterhouse. Table 2-1 shows the geometry of the tracheal cartilage rings and smooth muscle of the pig airways. The relationship between displacement and transmural pressure was measured (within 6 h after the pigs were slaughtered) in the pig trachea by using the apparatus shown in Fig. 2-2. Each trachea was clamped to the straight tubes that are connected to the reservoirs in the pool filled with saline, and the tracheal smooth muscle was located at the top and the tracheal cartilage rings at the bottom of the pool. The deformation of tracheal cartilage rings (d_{TC}) and tracheal smooth muscle (d_{TS}) were measured by using a laser displacement meter (KEYENCE, LX2-03, Japan). The meter has a parallel laser beam design (transmitter and receiver) and provides an output proportional to the amount of the laser that reaches the receiver. This meter has a static shutter at the transmitter to restrict the laser sheet width when d_{TC} and d_{TS} were measured individually. Before measuring the deformation, this meter was calibrated in the pool filled with saline. After a trachea was placed horizontally in the pool filled with saline, d_{TC} and d_{TS} were measured by varying the transmural pressure, which was regulated by varying the height of two reservoirs filled with saline (an internal reservoir feeding the trachea and an external reservoir feeding the pool). Assuming a normal breathing, the transmural pressure ranged from 0 to 15 cmH_2O. Cartilage rings and smooth muscle are viscoelastic, and so d_{TC} and d_{TS} were measured statically at 2 min after the pressure was applied. The output was digitized with a 16-bit A/D converter (NIHON KOHDEN, LEG – 1000, Japan).

2.2.2 *Mechanical Models to Determine Elastic Modulus*

Two mechanical models were devised to determine the Young's modulus of tracheal smooth muscle (E_{TS}) and cartilage rings (E_{TC}) (Timoshenko and Woinowsky-krieger, 1959). The model for the deformation of smooth muscle, shown in Fig. 2-3A, is based on large deflections of uniformly distributed loaded (q) rectangular plates with clamped edges. In this case the deflection is no longer small in comparison with the plate thickness and the strain of the middle plane of the plate must be included and it is very difficult to solve the non-linear equations of equilibrium and moments. The principle of minimum potential energy was applied to obtain an approximate calculation of the deflection (u, v, w). The normal components of stresses in X, Y and Z directions are σ_x, σ_y, and σ_z, and shear stress are τ_{xy}, τ_{xz} and τ_{yz}. In this model the total energy Π is expressed by applying the principle of virtual displacements as follows.

$$\Pi = \frac{1}{2}\iiint\left[\frac{1}{E_{TS}}\left(\sigma_x{}^2 + \sigma_y{}^2 - 2\nu\sigma_x\sigma_y\right) + \frac{1}{G_{TS}}\tau_{xy}{}^2\right]dxdydz - \iint q d_{TS} dxdy \qquad (2.1)$$

G_{TS} is modulus of elasticity in shear. The unit strains in X, Y and Z directions are ε_x, ε_y and ε_z, and the shearing components are γ_{xy}, γ_{xz} and γ_{yz}. The equations of equilibrium are expressed as follows.

$$\varepsilon_x = \frac{\partial u}{\partial x} + \frac{1}{2}\left(\frac{\partial w}{\partial x}\right)^2 - z\frac{\partial^2 w}{\partial x^2}, \quad \varepsilon_y = \frac{\partial v}{\partial y} + \frac{1}{2}\left(\frac{\partial w}{\partial y}\right)^2 - z\frac{\partial^2 w}{\partial y^2},$$

$$\gamma_{xy} = \frac{\partial u}{\partial y} + \frac{\partial v}{\partial x} + \frac{\partial w}{\partial x}\frac{\partial w}{\partial y} - 2z\frac{\partial^2 w}{\partial x \partial y}, \qquad (2.2)$$

$$\sigma_x = \frac{E_{TS}}{1-\gamma^2}(\varepsilon_x + \nu\varepsilon_y), \quad \sigma_y = \frac{E_{TS}}{1-\gamma^2}(\varepsilon_y + \nu\varepsilon_x), \quad \tau_{xy} = \frac{E_{TS}}{2(1-\gamma)}\gamma_{xy},$$

To satisfy the boundary conditions and the conditions of symmetrical deformation, the displacement is specified as follows.

$$u = A\sin\frac{2\pi}{\mathrm{u}}x\cos\frac{\pi}{\mathrm{v}}y, \quad v = B\sin\frac{2\pi}{\mathrm{u}}y\cos\frac{\pi}{\mathrm{v}}x, \quad w = d_{TS}\cos\frac{\pi}{\mathrm{u}}x\cos\frac{\pi}{\mathrm{v}}y, \quad (2.3)$$

The total energy of the plate for a position of equilibrium is minimum.

$$\frac{\partial\Pi}{\partial A} = 0, \quad \frac{\partial\Pi}{\partial B} = 0, \quad \frac{\partial\Pi}{\partial d_{TS}} = 0, \qquad (2.4)$$

Finally the E_{TS} is derived from Eqs. (2.1), (2.2), (2.3) and (2.4) from d_{TS} and q.

$$E_{TS} = k\frac{q(1-\gamma^2)}{k_1 h d_{TS}{}^3 + k_2 h^3 d_{TS}} \quad (k, k_1, k_2 : \text{constant}, \ \gamma = 0.5) \qquad (2.5)$$

where k, k_1, and k_2 are constants and depend on the shape of the smooth muscle, such as major axis (u), and minor axis (v).

The model for the deformation of cartilage rings, shown in Fig. 2-3B, is based on part of a cylindrical shell being supported along the edges and exposed to a uniformly distributed load (q) normal to the surface. In this model, the equations of equilibrium and moments can be finally written as follows.

$$\frac{\partial^2 u}{\partial x^2} + \frac{1-\nu}{2a^2}\frac{\partial^2 u}{\partial \varphi^2} + \frac{1+\nu}{2a}\frac{\partial^2 v}{\partial x \partial \varphi} - \frac{\nu}{a}\frac{\partial w}{\partial x} = 0$$

$$\begin{gathered}\frac{1+\nu}{2}\frac{\partial^2 u}{\partial x\partial\varphi}+a\frac{1-\nu}{2}\frac{\partial^2 v}{\partial x^2}+\frac{1}{a}\frac{\partial^2 v}{\partial\varphi^2}-\frac{1}{a}\frac{\partial w}{\partial\varphi}=0\\ \nu\frac{\partial u}{\partial x}+\frac{\partial v}{a\partial\varphi}-\frac{w}{a}-\frac{h^2}{12}\left(a\frac{\partial^4 w}{\partial x^4}+\frac{2}{a}\frac{\partial^4 w}{\partial x^2\partial\varphi^2}+\frac{\partial^4 w}{a^3\partial\varphi^4}\right)=-\frac{aq(1-\gamma^2)}{Eh}\end{gathered} \tag{2.6}$$

To satisfy the boundary conditions and the conditions of symmetrical deformation, the displacement (u, v, w) is specified as follows.

$$u=A\sin\frac{\pi\varphi}{\phi}\cos\frac{\pi x}{\mathrm{u}},\quad v=B\cos\frac{\pi\varphi}{\phi}\sin\frac{\pi x}{\mathrm{u}},\quad w=d_{TC}\sin\frac{\pi\varphi}{\phi}\sin\frac{\pi x}{\mathrm{u}}, \tag{2.7}$$

Finally the E_{TC} is derived from Eqs. (e) and (f) from d_{TC} and q.

$$E_{TC}=j\frac{qa^2(1-\gamma^2)}{d_{TC}h}\quad (j:\text{ constant, } \gamma=0.5) \tag{2.8}$$

where j is a constant and depends on the shape of the cartilage rings, such as angle (α), major axis (u) and minor axis (v).

2.3 Results and Discussion

Fig. 2-4 shows the calibration of a laser displacement meter. Fig. 2-5 shows the deflection of tracheal cartilage rings (d_{TC}) and tracheal smooth muscle (d_{TS}) as a function of the transmural pressure (*Ptp*). The rate of increase in d_{TC}, and d_{TS} decreased with pressure, which is consistent with previously published results (Ishida et al., 1990). At low pressure (0–3 cmH$_2$O) d_{TC} and d_{TS} linearly increased with pressure, and dd_{TS}/dP_{TP} was about 15 times larger than dd_{TC}/dP_{TP}. Using Eqs. (2.5) & (2.8) and this linear relationship between the transmural pressure and the deflection, the calculated E_{TC} and E_{TS} were 5.8 ± 2.9 MPa and 0.65 ± 0.32 MPa, respectively.

To determine E_{TS} and E_{TC}, the each simple mechanical model with clamped edges were devised and they were calculated using the linear relationship between the pressure and defection. If the cartilage rings doesn't connect to the smooth muscle and the edges are not fixed, the maximum deflection at the edges is 0.22 mm (Fig. 2-5). For the smooth muscle, this deflection is significantly smaller than the maximum defection (3.4 mm). Since the cartilage rings are much harder than smooth muscle, the deformation of the cartilage rings is not influenced with that of the smooth muscle. And for low-pressure region, the displacement was fairly small and the trachea did not become bend.

The tracheal cartilage rings itself consists of many cartilage rings and smooth muscle, and strictly it is not a continuous cylindrical shell. However, the cartilage ring is much harder than smooth muscle, and so the deformation of tracheal cartilage rings is mainly influenced with the cartilage ring. And so assuming that the tracheal cartilage rings was a simple cylindrical shell, E_{TC} and E_{TS} were analyzed. And because fabricating a model that had uniform thickness was difficult, an average thickness of the cartilage rings and smooth muscle was adapted. Thus, the values of E_{TC} and E_{TS} are each lumped average value of all of the smooth muscle and cartilage rings, respectively.

The most important factor of the mechanical models to determine the Young's modulus was tracheal geometry (length, diameter and angle). Especially, E_{TC} was influenced by the number of cartilage rings. The tracheal geometry of human is similar to that of pig.

Lambert and Baile (1991) reported an estimated averaged Young's modulus of tracheal cartilage rings of 4.4 ± 2.3 MPa, which is similar to E_{TC} (5.8 ± 2.9 MPa in this chapter). Their apparatus was designed to apply preset deformations to tracheal cartilage rings and to monitor the deformation force, and they calculated Young's modulus from the load–deformation behavior based on thin curved beam theory. Rains et al. (1992) examined the Young's modulus of 1.5 cm strip cut from tracheal cartilage rings of 10 individuals that ranged from 17 to 81 yr in age. They reported age-related changes in the biomechanical properties of the Young's modulus, which ranged between 1 and 15 MPa, a range that includes our E_{TC}.

In general, lung compliance is determined by wall elasticity and surface tension. Jayaraman et al., (2002) recently developed novel fluorescent probes and microscopy methods to measure the thickness of surface liquid *in vivo*, and reported that the depth of isolated human main bronchi was 55 ± 5 μm. This depth is much smaller than tracheal diameter (approximately 20 mm). And then localized compliance of trachea is hardly determined by surface tension but wall elasticity. In this chapter, especially, the Young's modulus was measured as wall elasticity. The Young's modulus is useful to analyze flow structure and airway resistance.

2-4 Summary

In this chapter, the Young's modulus of cartilage rings and of smooth muscle were analyzed by using pig trachea, and E_{TC} and E_{TS} were 5.8 ± 2.9 MPa and 0.65 ± 0.32 MPa respectively. The deformation of smooth muscle were approximately 10 times as large as that of cartilage rings. These results suggested that the localized variation of wall compliance effects the airflow structure.

Table 2-1 Geometry of tracheal cartilage rings and smooth muscle of pigs. Values are average ± S.D. (n = 9).

	Length [mm]	Diameter [mm]	Breadth [mm]	Thickness [mm]	Angle [degree]	Density [kg/m^3]
Cartilage rings	94.5±8.9	19.4±1.8	-	2.3±0.4	261.2±5.6	1365.6± 164.7
Smooth muscle	94.5±8.9	-	6.9±2.0	1.1±0.2	-	968.7± 151.5

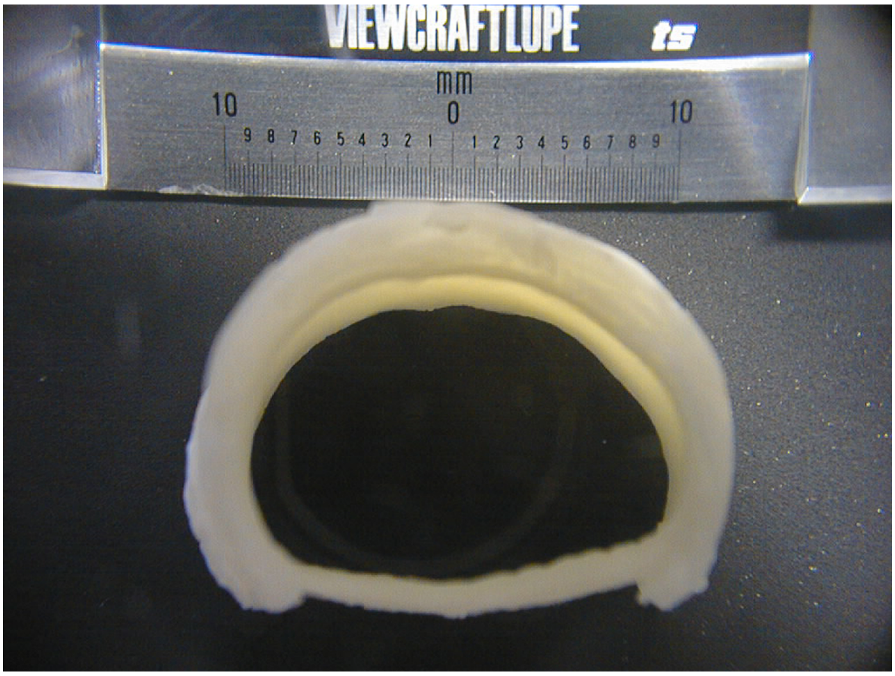

Fig. 2-1 Photograph of tracheal cartilage rings and smooth muscle of pig.

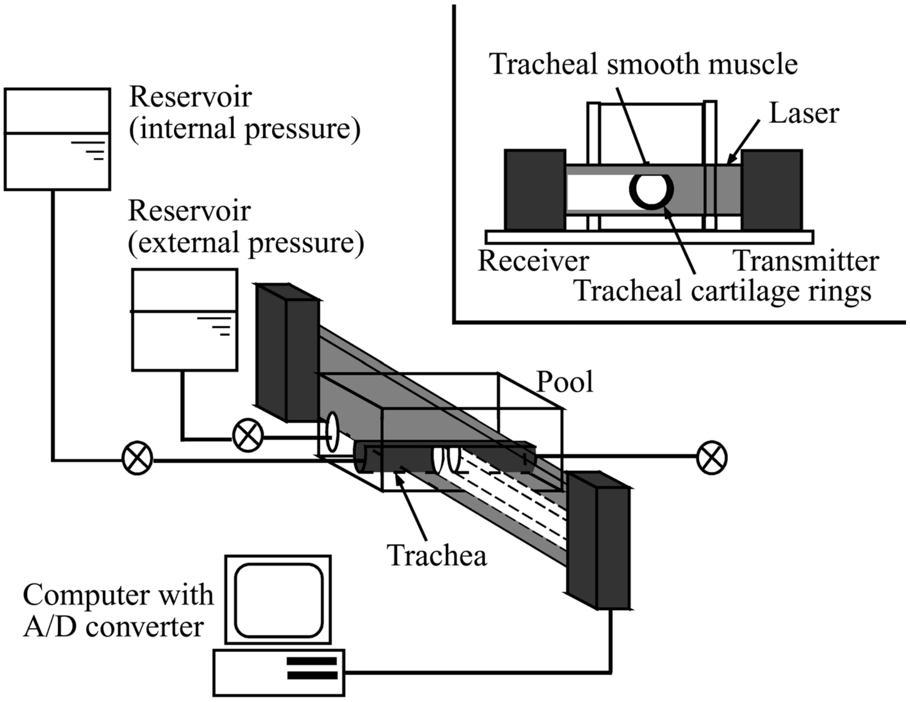

Fig. 2-2 Experimental apparatus for measuring tracheal deflection as a function of transmural pressure. The static shutter was used to measure d_{TS} and d_{TC} individually; when d_{TS} was measured the cartilage rings was not rayed, and when d_{TC} was measured the smooth muscle was not rayed.

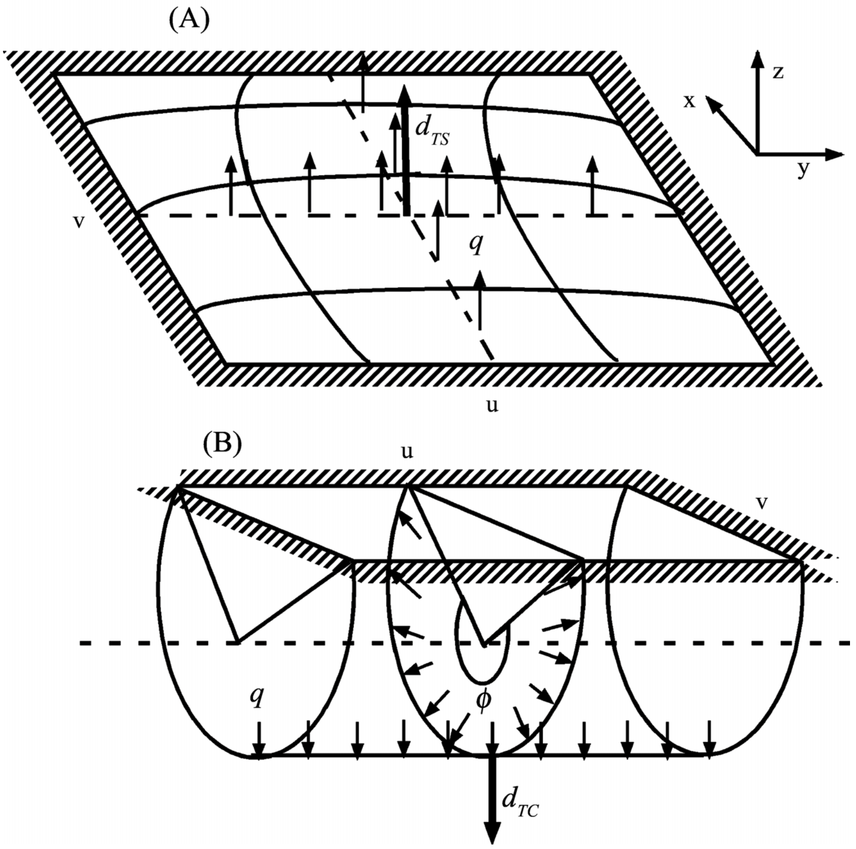

Fig. 2-3 Mechanical models to determinate (A) the Young's modulus of the smooth muscle and (B) tracheal cartilage rings.

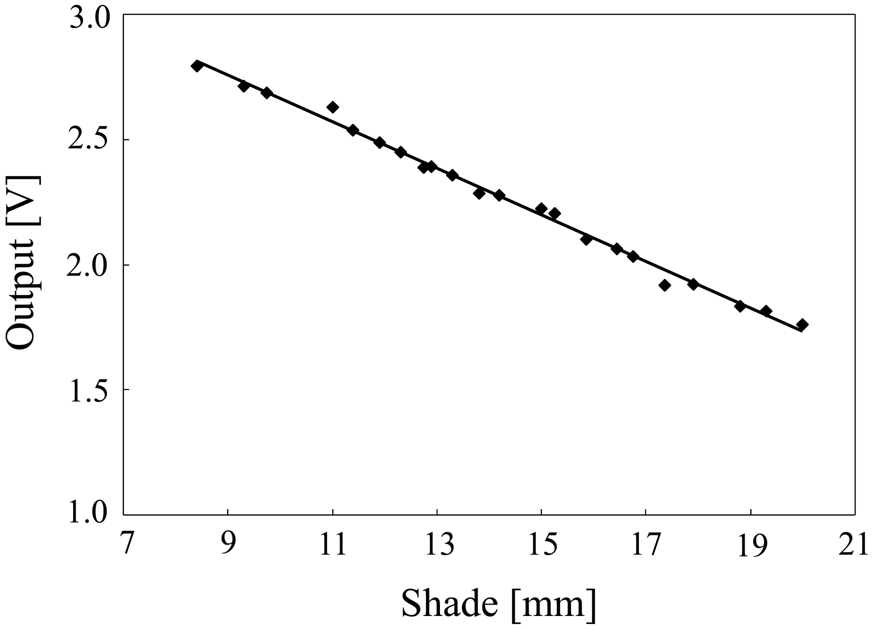

Fig. 2-4 Calibration of a laser displacement meter (LX2-03, Japan).

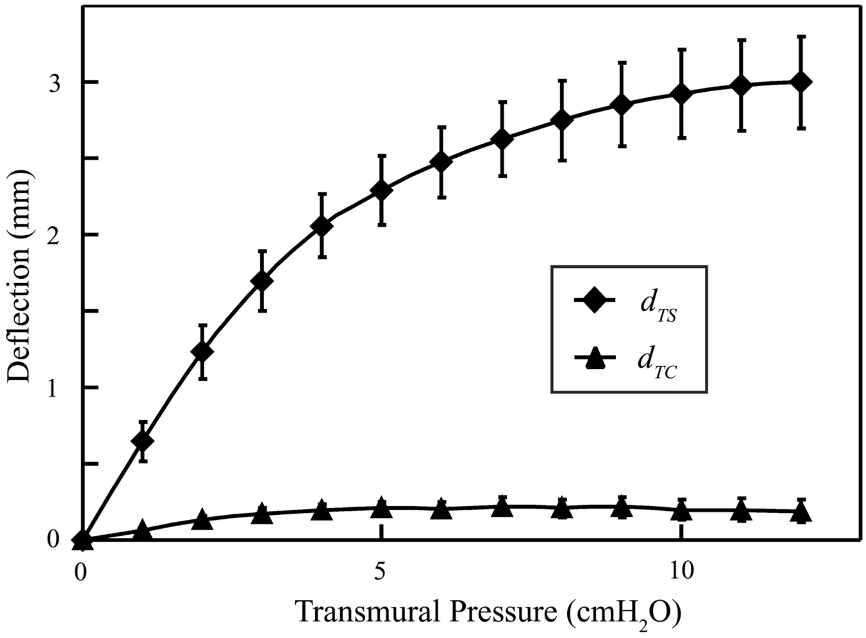

Fig. 2-5 Tracheal deflection (d_{TS} and d_{TC}) as a function of transmural pressure (P_{tp}). Error bars show standard deviation.

Reference

Art T, and Lekeux P. Mechanical properties of the isolated equine trachea. Res. Vet. Sci 51, 55-60, 1991.

Ishida K, Paré PD, Blogg T, and Schellenberg RR. Effects of elastic loading on porcine tracheal muscle mechanics. J Appl Physiol 69, 1033-1039, 1990.

James AL, Paré PD, Moreno RH, and Hogg JC. Quantitative measurement of smooth muscle shortening in isolated pig trachea. J Appl Physiol 63, 1360-1365, 1987.

Jayaraman S, Song Y, Vetrivel L, Shankar L, and Verkman AS. Noninvasive in vivo fluorescence measurement of airway-surface liquid depth, salt concentration, and pH. J. Clin. Invest 107, 317-324, 2001.

Lambert RK, and Baile EM. A method for estimating the Young's modulus of complete tracheal cartilage rings. J Appl Physiol 70, 1152-1159, 1991.

Mitchell HW, Turner DJ, Gray PR, and Mcfawn PK. Compliance and stability of the bronchial wall in a model of allergen-induced lung inflammation. J Appl Physiol 86, 932-937, 1999.

Rains JK, Bert JL, Roberts CR, and Paré PD, Mechanical properties of human tracheal cartilage. J Appl Physiol 72, 219-225, 1992.

Timoshenko SP, Woinowsky-krieger S, Theory of plates and shells. MacGall-Hill. New York, 1959.

Chapter 3

Visualization and Morphometry of Small Airways from Microfocal X-ray Computed Tomography

3-1 Introduction

In this chapter, new method to visualize small airways under "near" physiological condition without dehydration and fixation is presented. Small airways were visualized in detail by staining the lung tissue with a radiopaque solution and then visualizing with a micro-CT. This staining and CT imaging method is called the SCT method. The three-dimensional morphometry was analyzed from these obtained CT images using the three-dimensional thinning algorithm. Generally, micro-CT systems are used to analyze solid preparations (Lerman et al., 1999; Masyuk et al., 2001). Because X-ray imaging depends on differences in density, sodium diatrizoate solution was used as the contrast medium. Sodium diatrizoate, which is generally known as hyperosmotic contrast media, has been used in clinical diagnosis to visualize the urinary tract (Castellino and Marshall, 1970). In the SCT method, a sodium diatrizoate solution was perfused into the pulmonary vessels, thus staining the lung tissue.

First, as a proof of concept, the SCT method was applied to stain excised rat lungs and visualize the airways. Then, the optimum staining time and concentration for the SCT method were determined. To verify the method, the micro-CT images using the SCT method were compared from tantalum dust method. Finally, three-dimensional branching structure was reconstructed from the continuous CT images, and the morphometry was analyzed using the three-dimensional thinning algorithm.

3.2 Materials and Methods

3.2.1 *Animal Preparation*

All animals used in the experiments received humane care and the experimental protocol was approved by the Committee of Laboratory Animals according to Keio University guidelines. Excised rat lungs were prepared as follows. After male fourteen Wister rats (300 ± 30 g) were anesthetized with pentobarmital sodium (50 mg/kg i.p.), an inferior vena cava was cannulated and perfused with a 0.9 % normal saline solution for 5 min at flow rate in the range of 5 - 40 ml/min. The cannulation was done with the chest open and during preparation the lungs were kept inflated at FRC (functional residual capacity; lung volume: 3 ml). When the perfusate draining through the pulmonary veins was free of blood, a 0.2 g/ml KCl solution was injected into the heart to induce cardiac arrest, and the sodium diatrizoate solution was injected into the pulmonary arteries via the cannula for 1 min at flow rate in the range of 5 - 40 ml/min. The powder of Sodium diatrizoate (Sigma Chemical, St Louis, MO) was mixed with distilled water to achieve the appropriate concentration, called *the staining concentration*. The length of time during which the lungs were then exposed to ambient air to allow staining of lung tissue is called *the staining time*. The lungs were then excised and placed into a Plexiglas cylinder to prevent desiccation during imaging. To determine the optimal parameters for the SCT technique, the staining time (15 min, 30 min, 1 h and 2 h) and stating concentration (0.4 and 0.8 g/ml) was varied.

3.2.2 *Imaging*

The small airways were imaged using a cone-beam micro-CT system (MCT-CB100MF, Hitachi Medical Corp., Japan, Tokyo) (Fig. 4-1). The micro-CT system consists of a microfocal cone-beam X-ray source (spot size: 7 μm), x-y-z-θ rotation stage, an image intensifier and a 12-bit CCD camera. To reconstruct the CT images, a summed projection was acquired at 625 rotational positions. The resolution was 480 × 480 pixels, and in one rotation the 200 slice images was obtained. The smallest cubic voxel size achieved was 14 μm, and thus the maximum high-resolved volume was 6.72 × 6.72 × 2.8 mm. Prior to imaging, the lungs were inflated once to TLC (total lung capacity; lung volume: 11 ml) and then deflated to FRC and held at that volume. It took 2.5 min for the cylinder including the excised rat lung to rotate 360°.

3.2.3 *Methodology*

To examine whether the leakage of the radiopaque solution occurred into the alveoli airspace and if any alveoli were collapsed, the stained lungs were investigated by a light microscope. The excised lung using the SCT method was frozen and sliced (5 μm thick) at FRC with Tissue Tek O.C.T. Compound (Sakura Finetek Inc., Torrance, CA). The lung tissue was stained by hematoxylin and eosin, and observed under the light microscope. And to confirm that the SCT method could accurately identify the airways, a rat lung was visualized that was first injected with the radiopaque solution and then insufflated with tantalum dust (325 mesh) by mechanical ventilator from the trachea.

3.2.4 *Three-dimensional Reconstruction and Measurements*

Reconstruction and visualization of the imaged volume was done with the *Visualization Toolkit* (VTK), which is an open-source, object-oriented software system for 3D computer graphics and imaging processing used by many researchers (*Kitware, Inc.*, http://www.kitware.com/). The cross-sections of the small airways were identified using a threshold method. These steps were as follows: 1) Pick up the continuous CT images of the small airway trees. 2) Mark inside the lumen areas of the target airways throughout all images. 3) Find the edges of the marked inside area until the pixel intensity was equal to the threshold value. The pixel intensity of lung tissue varies in the images because lung tissue was not stained entirely uniformly, and the optimum threshold value for individual airways was decided. These continuous cross-section images were analyzed using the three-dimensional thinning algorithm described by Toriwaki et al. (2001). This algorithm makes the Euclidean distance transformation and repeatedly checks deletability of the points in sequence that the Euclidean distance value is small, and finally finds the middle line and the branching point of the airway network without changing the topology. This algorithm left the “false” spurs, and they were removed manually.

The airway has approximately the shape of a hollow cylinder network (starting point A (x_A, y_A, z_A), branching point B (x_B, y_B, z_B), and ending point C (x_C, y_C, z_C)) and the length L, branching angle α, and gravity angle β in Fig. 3-2A & B were calculated as follows.

$$L = \sqrt{(x_A - x_B)^2 + (y_A - y_B)^2 + (z_A - z_B)^2}$$

$$\cos\alpha = \overrightarrow{BA} \cdot \overrightarrow{BC} \big/ |BA| \cdot |BC|$$

$$\cos\beta = \overrightarrow{AB} \cdot n_z \big/ |AB| \quad (n_z\text{: unit vector of } z \text{ direction})$$

A horizontal airway has a gravity angle of 90°. The orthogonal plane Π centred the middle point M (x_M, y_M, z_M) in AB and perpendicular to the hollow cylinder AB was estimated as follows.

$$ax + by + cx = d$$

$$a = x_B - x_A,\ \ b = y_B - y_A,\ \ c = z_B - z_A,\ \ d = a \cdot x_M + b \cdot y_M + c \cdot z_M$$

The point in Π that the Euclidean distance value = 1 was defined as the edge points Pi (x_{Pi}, y_{Pi}, z_{Pi}). The Euclidean distance is the distance from background. The mean diameter D was calculated as follows.

$$\frac{|a \cdot x_{pi} + b \cdot y_{pi} + c \cdot z_{pi} - d|}{\sqrt{a^2 + b^2 + c^2}} = 0 \quad (Pi \in \Pi)$$

$$D = \frac{2 \cdot \sum_i |MPi|}{\sum_i Pi}$$

These morphometry of small airways are presented as the average in each airway generation $\boldsymbol{Z}$

referenced to the branching system of Weibel (1963) (i.e. counting the number of bifurcations from the trachea). To find airway generation, the whole lung was macroscopically imaged using micro-CT (1 cubic voxel: 43 μm).

3.3 Results

3.3.1 *Spatial Resolution*

For evaluation of the effective resolution of micro-CT, nine Titanium-Barium glass beads (300, 200 and 100 μm diameter) (UNION CO., LTD, Tokyo, Japan) were imaged (1 cubic voxel: 14 μm) as the test phantom, and the diameter of the glass beads was calculated from CT images. The depth position, in which the maximum diameter was detected, was defined as $z = 0$ and the center of mass in $z = 0$ was defined as the center of the bead O. Then, the center of mass O' and diameter d in each image were calculated in all slices and the bead diameter from CT images were defined as follows.

$$\text{Beads diameter from CT images} = \sqrt{(d/2)^2 + |OO'|^2} \cdot 2$$

The accuracy of our estimates of glass beads diameter was summarized (Table 3-1). The residual of 300 μm diameter glass beads was 4.5 %, 200 μm diameter glass beads was 4.1 % and 100 μm diameter glass beads was 9.6 %. Because the maximum resolution in this imaging system was achieved that 1 voxel was 14 μm, small diameter phantom not measured with accuracy. In this experiment the small airways over 150 μm were analyzed.

3.3.2 *Optimal Staining Time and Concentration*

Compared the staining concentration, the average pixel intensity of lung tissue at 0.8 g/ml solution was 1.2 times as large as at 0.4 g/ml, suggesting that the average pixel intensity of the stained lung tissue depended on the staining concentration (Fig. 3-3). When the concentration was lower, the small airway lumens could not be clearly identified because only lung tissue around pulmonary vessels was stained.

When the staining time was 15 min and 30 min, neither vessels with strong intensity nor small airways could be identified, indicating that sodium diatrizoate had not yet permeated from the pulmonary vessels (Figs. 3-4A & B). However, when the staining time exceeded 1 h, the intensity of the lung tissue was the same as that of the pulmonary vessels, and diatrizoate had fully permeated into the lung tissue (Figs. 3-4C & D).

In the following experiments, a 1 h staining time and a 0.8 g/ml staining concentration were used.

3.3.3 *Validation*

The alveolar ducts and alveolar sacs were not collapsed and the alveoli surrounding pulmonary vessel were not collapsed (Figs. 3-5A & B). The alveolar ducts and alveolar sacs were not collapsed, and the alveoli surrounding pulmonary vessel were not collapsed. This indicates that leakage of radiopaque solution did not occur. Therefore the SCT method is useful to visualize the small airways under “near” physiological condition.

The SCT method identified airways as the tubes and associated branchings (Figs. 3-5C, tube a) on which tantalum dust was deposited; it also identified the pulmonary vessels as the tubes (Fig. 4-5C, tube b) but not having dust-deposited lumens. Moreover, tantalum dust also deposited on the surfaces of parts that were not stained by the radiopaque solution, indicating that the radiopaque solution did not permeate into the airway lumen. This further confirms that the SCT method can clearly identify airway geometry.

3.3.4 *Visualization of Small Airways*

Using the SCT method, not only small airways but also alveoli were visualized (Fig. 3-6) and the continuous, complex branching airways can be clearly visualized in detail (Fig. 3-7). Using the threshold method the cross-sections of the parent airway and the small bronchus merging into the parent airway were identified (Fig. 3-8). The threshold value hardly affected on this process, because staining of tissues ensures that the tissue X-ray density is far greater than that of the unstained lumenal air spaces. The cross-sections of the associated branching and merging airways were similarly identified in the continuous images. The three-dimensional structure was reconstructed using an isosurface approach in VTK (Fig. 3-9).

3.3.5 *Morphometry of Small Airways*

It was apparent that the middle lines agreed with the outlines (Fig. 3-10). Using these middle lines the average diameter *D* and average length *L* were calculated as a function of ***Z*** (Fig. 3-11). *D* and *L* decreased by an exponential function like Weibel data (1963) and was fitted to the Eq. (3.1) and (3.2).

$$D(Z) = 1.1104 \cdot 2^{-0.1777Z} \qquad (3.1)$$

$$L(Z) = 1.7015 \cdot \mathrm{e}^{-0.0851Z} \qquad (3.2)$$

The average diameter ratio (daughter diameter / parent diameter) in small airways was 0.89 and the average ratio length to diameter (*L*/*D*) was 2.26 ranging from 2.02 to 2.63.

The branching angle α and gravity angle β as a function of ***Z***, and α and β was approximately constant at 133.3 ± 23.8° and 63.9 ± 13.2° over the generations studied (Fig. 3-12). In this study, β was analyzed the only downward airways ($\beta < 90^\circ$). It is well known that the airways branch asymmetrically and therefore the asymmetry of the bifurcation *As* was defined as follows.

$$As = \alpha_1 / \alpha_2 (\alpha_1, \alpha_2 \subseteq \alpha)$$

α_2 was defined as the pair branching angle of α_1, and α_1 was major and α_2 was minor ($\alpha_1 > \alpha_2$). The asymmetry *As* was expressed as a function of ***Z*** and as a function of α_2 (Figs. 3-13A & B). And *As* proportionally decreased with α_2 and was linearly fitted to the Eq. (3.3).

$$As = -0.0131 \cdot \alpha_2 + 2.8791 \quad (3.3)$$

Eq. (3.3) indicated that one branching angle (α_1) decided the other pair branching angle (α_2) and in the case of the symmetric bifurcation ($\alpha_1 = \alpha_2$) the branching angle was approximately 140º.

3.4 Discussion

The SCT method is the first reported method that yields high-resolution images of the small airways in "near" physiological condition without dehydration and fixation. Sodium diatrizoate gradually permeated out of the vessels into surrounding lung tissue via a permeability mechanism that has been controversial for many years (Fig. 4-14). Waldron et al. (1973) injected sodium diatrizoate into the carotid artery of cats and revealed two possible mechanisms: (a) alteration of the tight junctions between capillary endothelial cells and (b) transport across the endothelial cells by pinocytosis. Haller et al. (1997) investigated the cytotoxicity of radiopaque agents on epithelial cells by incubating renal epithelial cells monolayers in diatrizoate agents for 12 h. They found that in the diatrizoate-treated monolayer, apical microvilli were absent and there were numerous cytoplasmic vacuoles in the cells. Moreover, Schick and Haller (1999) analyzed the inulin permeability and distribution of tight-junction-associated membrane proteins, and concluded that the diatrizoate agents disturbed the tight-junction and that its inulin permeability was the highest among the radiopaque agents that they studied. Based on these previous results sodium diatrizoate probably permeated into lung tissue by pinocytosis and through the disturbed tight-junctions.

Using the SCT method, it was easy to distinguish small airways from pulmonary vessels. The vessels were filled with the radiopaque solution, and so the pixel intensity of the lumen areas of the vessels as well as lung tissue was higher than the lumen areas of the small airways (Fig 3-6, white arrows). If the vessels were not filled with the radiopaque solution and the lumen areas (Fig. 3-5C, tube b) could be identified, the vessels were identified as the tubes that did not connect to the airways in the continuous images.

Recently the three-dimensional thinning algorithms for 3D images have been studied (Taso and Fu, 1981; Toriwaki et al., 2001) and they have been improved to automatically remove the spurs. The spurs are left when the surface of the input images is not smooth. In this study 0 ~ 7 spurs per an airway dataset were removed manually, and finally it was apparent that the middle lines agreed with the input images (Fig. 3-10).

The three-dimensional morphometry of small airways was presented in detail for the first time and these data are useful for studying the biomechanical dynamics in small airways, such as airway dynamics (Heil, 1999), airflow structure (Liu et al., 2002), aerosol deposition (Comer et al., 2000; Zhang et al., 2001) and surfactant delivery (Zhang et al., 2003). In their previous study, Phalen et al. (1978) and Phillips et al. (1995) measured the branching geometry of rat bronchial casts as the function of diameter in large airways (diameter range: 0.4~1.2 mm) and reported that the *L/D* in large airways ranged approximately between 2.1 and 1.0, and it was smaller than that in small airways. This tendency is similar to the human conducting airways, and Sauret et al. (2002) reported that the *L/D* increased with ***Z***. Moreover Phillips et al. (1995) reported the asymmetry factor (the ratio of the cross-sectional area of the major daughter branch to that of the minor) in large airways was 4.16, however in small airways the value was 2.02, consistent with the geometry data presented by Phalen et al. (1978). These morphological differences between large airways and small airways characterized the heterogeneous lung function. In small airways *As* decreased with ***Z***, consistent with the geometry data presented by Phalen et al. (1978). The mechanical dynamics strongly depends on the asymmetry and non-planarity of the bifurcation (Nishida et al. 1997; Comer et al. 2000; Caro et al. 2002), and so the branching angle and gravity angle are very important factors in the description of airways.

The SCT method is not applied to human, but has physiological and clinical implications. The respiratory diseases mainly occur at small airways (Tashkin, 2002), and so it is important to that the compliance of small airways is analyzed in "near" physiological condition. For many years the lung compliance has been evaluated from the macroscopic viewpoint (the pressure – volume curve); however using the SCT method the compliance is analyzed at the microscopic local level of small airways. Using the SCT method the same airways were visualized and reconstructed at 1) FRC (Figs. 3-15A and 3-9C) and 2) TLC (Figs. 3-15B and 3-15C). At TLC the airspace clearly increased. Not only small airways but also alveoli were expanded; the diameter of small airways expanded 1.43 ~2.34 times at TLC in comparison with at FRC. This morphometry change during respiration will open the way to new research of the pulmonary dynamics.

3.5 Summary

The SCT method is the first reported method that yields faithful high-resolution images of soft tissue geometry without fixation and the three-dimensional morphometry of small airways is useful for studying the biomechanical dynamics in small airways. Using the SCT method, the three-dimensional structure of small airways was presented for the first time. Physiological geometry of small airways can open the way to new research on the biomechanical dynamics but also the clinical implication. And the compliance abnormality (surfactant abnormality and the deposition of fibrous tissue) occurs at microscopic level of a lung (bronchi and bronchiole), and then it is important to understand the microscopic compliance in small airways. Using the SCT method, the morphometry change and localized compliance of the small airways can be analyzed.

Table 3-1 Summary of the evaluation of the effective resolution of micro-CT. Beads diameter from CT images are average ± S.D. from 9 beads.

Beads Diameter (“Accurate Value”) (μm)	Beads Diameter from CT images (μm)
307.1±4.4	320.7±4.0
203.8±7.3	212.2±7.0
100.8±3.9	110.5+8.6

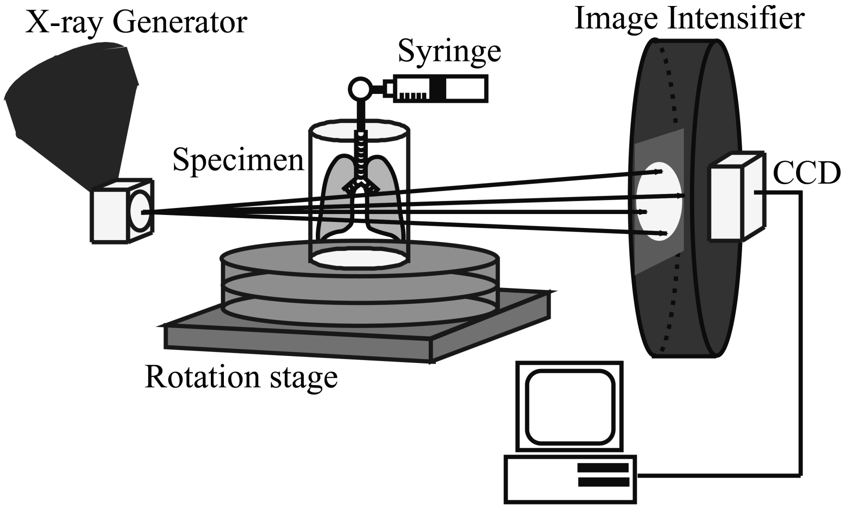

Fig. 3-1 Experimental apparatus of the SCT method. The Plexiglas cylinder containing the stained lungs was mounted on the rotation stage.

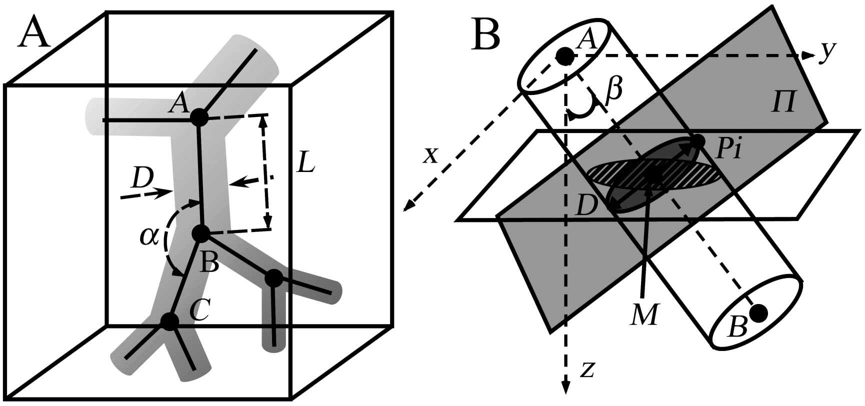

Fig. 3-2 The schematic diagram to calculate the geometry of the small airways. A: The airways were defined as a hollow cylinder network. (length *L*, branching angle *α* and diameter *D*). B: The gravity angle *β* was defined as the angle between the gravity direction *z* and airways *AB.*

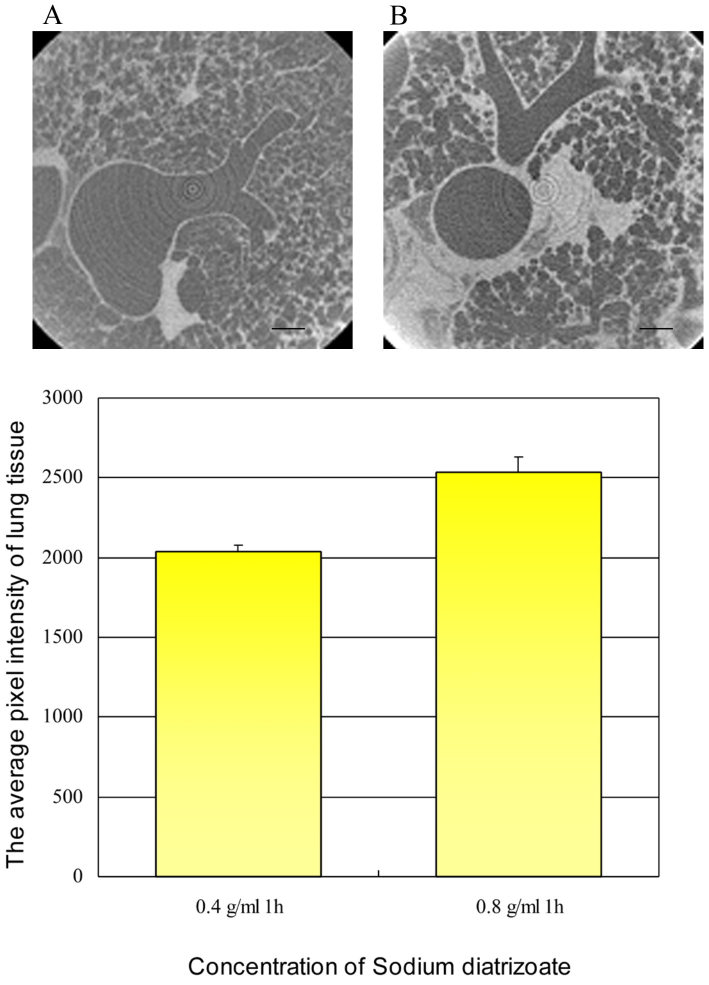

Fig. 3-3 The micro-CT images and the average pixel intensity for lungs stained with various staining concentration. Staining time was 1 h. Top: A: 0.4 g/ml and B: 0.8 g/ml. Bars: 500 μm. Bottom: the average pixel intensity of lung tissue.

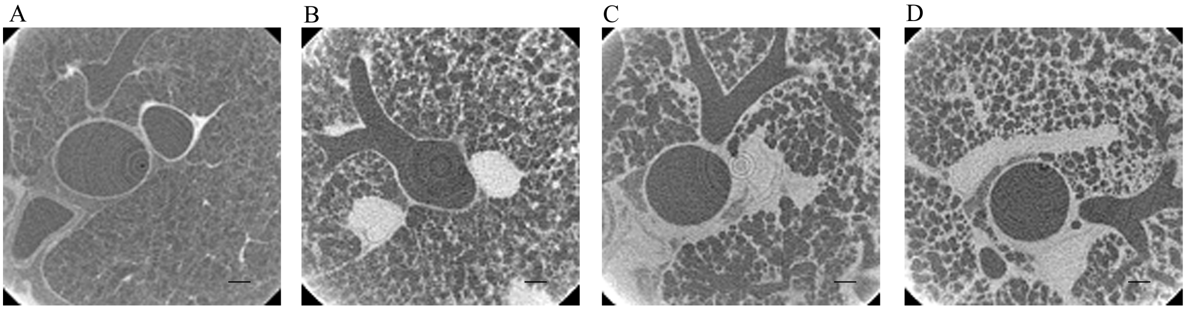

Fig. 3-4 The micro-CT images for lungs stained with various staining time. The concentration of sodium diatrizoate was 0.8 g/ml. Bars: 500 μm. A: 15 min, B: 30 min, C: 1 h, D: 2h.

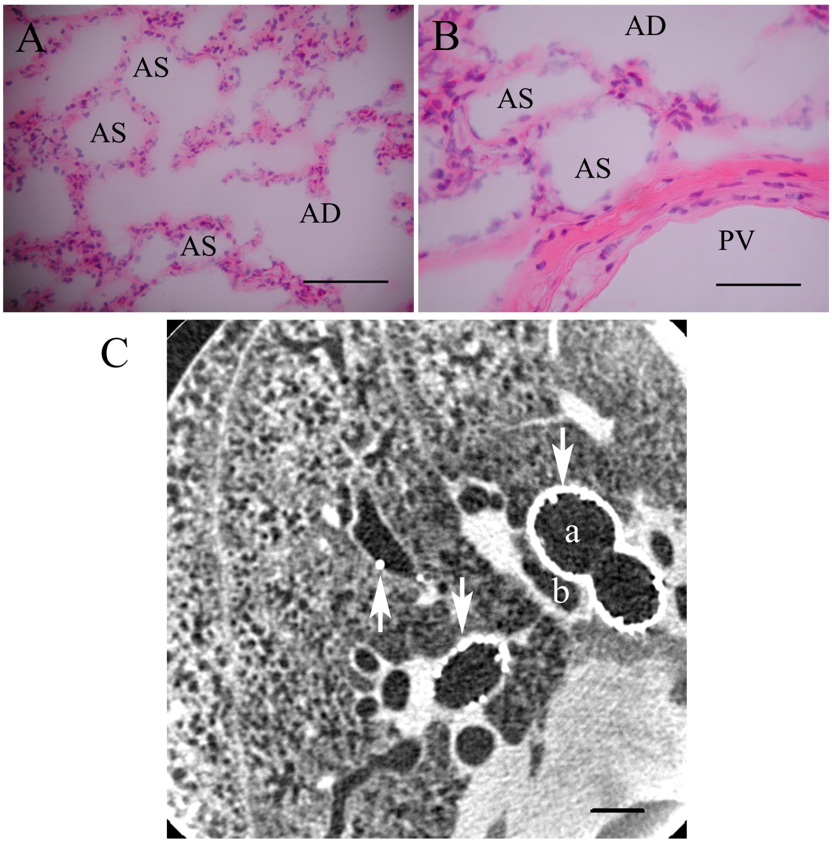

Fig. 3-5 Validation of the SCT method. (A, B) Light micrographs of the excised rat lung after the SCT method. (A): Bar: 100 μm. (B): Bar: 50 μm. AD: alveolar duct, AS: alveolar sac, PV: pulmonary vessel. (C): Comparison of SCT method with tantalum-dust insufflation method. Tantalum dust (arrows) is deposited on the airway surfaces. Tube (a): an airway and tube (b): a pulmonary vessel. Bar: 2 mm.

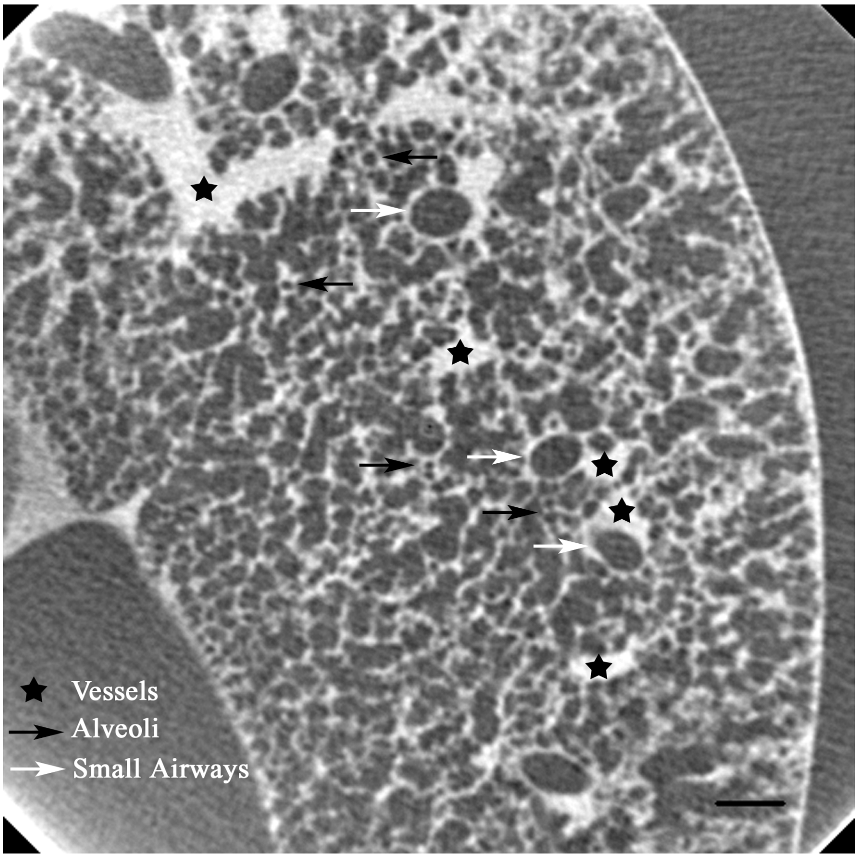

Fig. 3-6 Representative micro-CT image showing many small airways and alveoli at FRC. Sodium diatrizoate stained the lung tissue, and therefore, airway lumens with air had weaker intensity. Arrows indicate airways (white: small airways, black: alveoli) and stars indicate vessels. Bar: 500 μm. (1 square pixel = 16 μm).

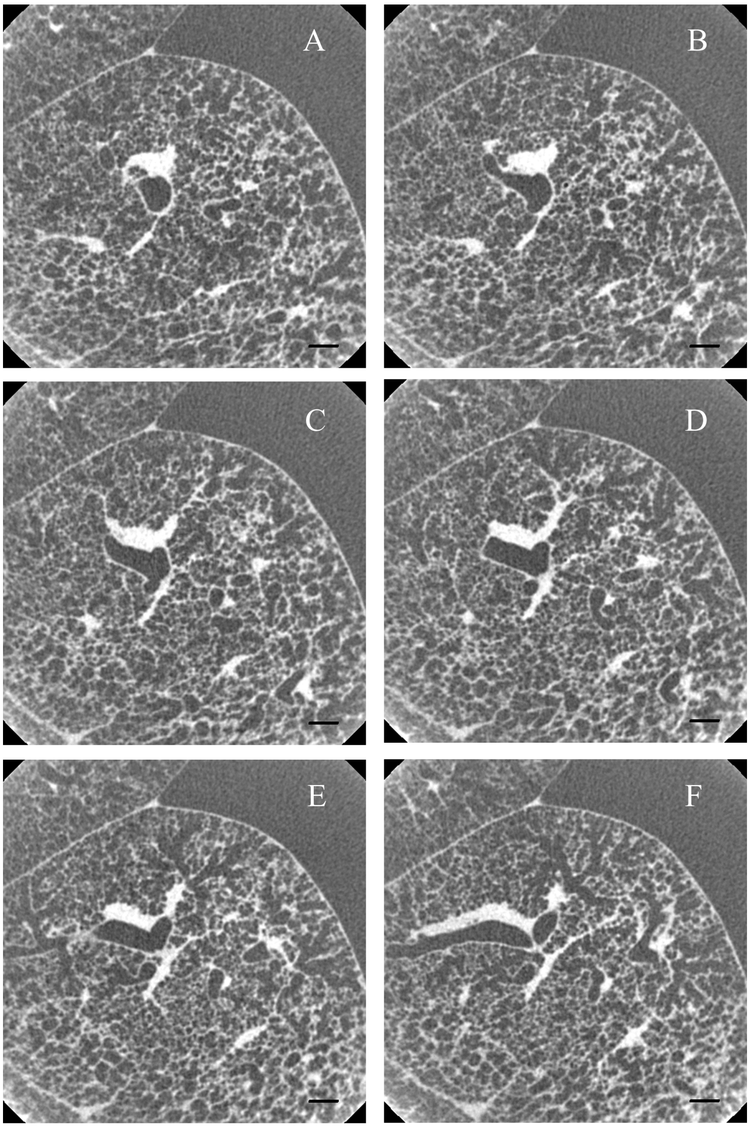

Fig. 3-7 Representative continuous micro-CT images using SCT method. The spacing between each image is 64 μm. Bar: 500 μm.

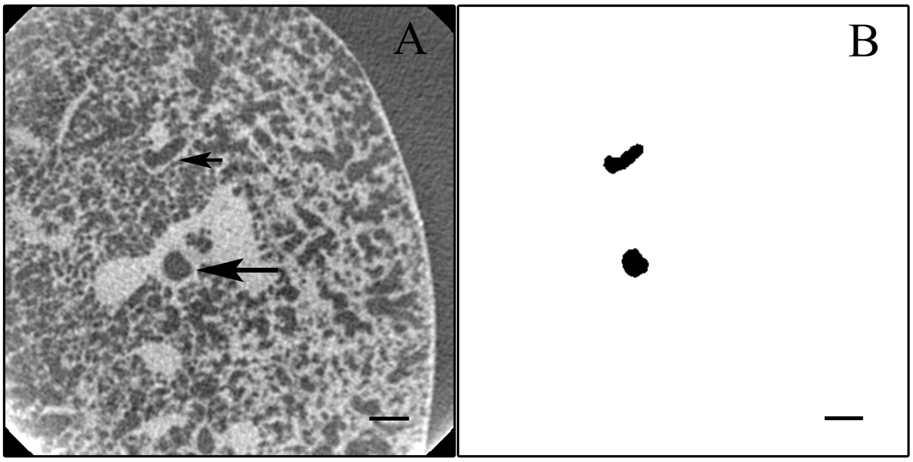

Fig. 3-8 Representative airways cross-sections analyzed using the threshold method; (A): original micro-CT image and (B): airways cross-sections. The parent airway (large arrow) and associated airways (small arrow) only were analyzed. Bar: 500 μm.

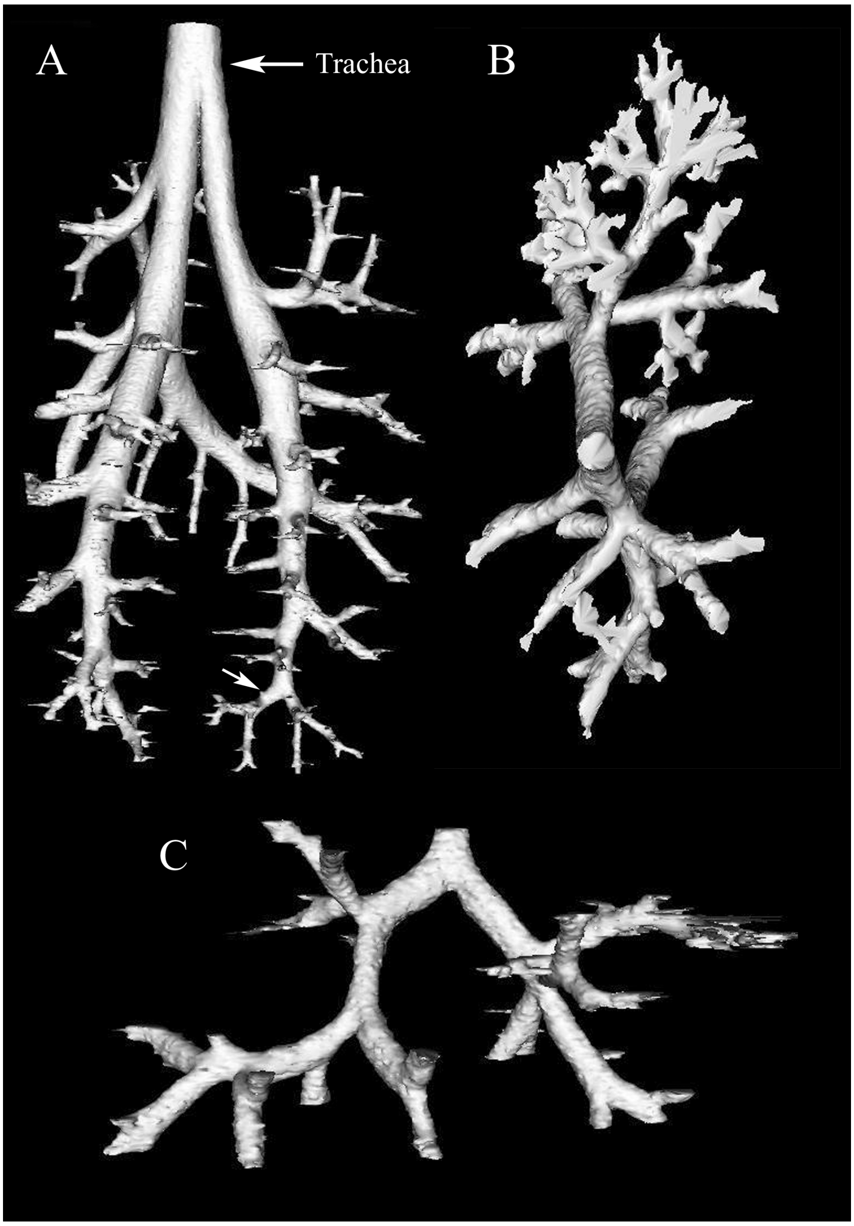

Fig. 3-9 Three-dimensional reconstruction from cross-section images using an isosurface approach in VTK. (A): the whole airway reconstructed the micro-CT images using the SCT method. (1 cubic voxel size: 43 μm). (B & C): the small airway. (1 cubic voxel size: 16 μm, Diameter range: 300 μm ~ 170 μm, ***Z***: 10 ~ 16). Small arrow in (A) shows the starting point of (B) and (C).

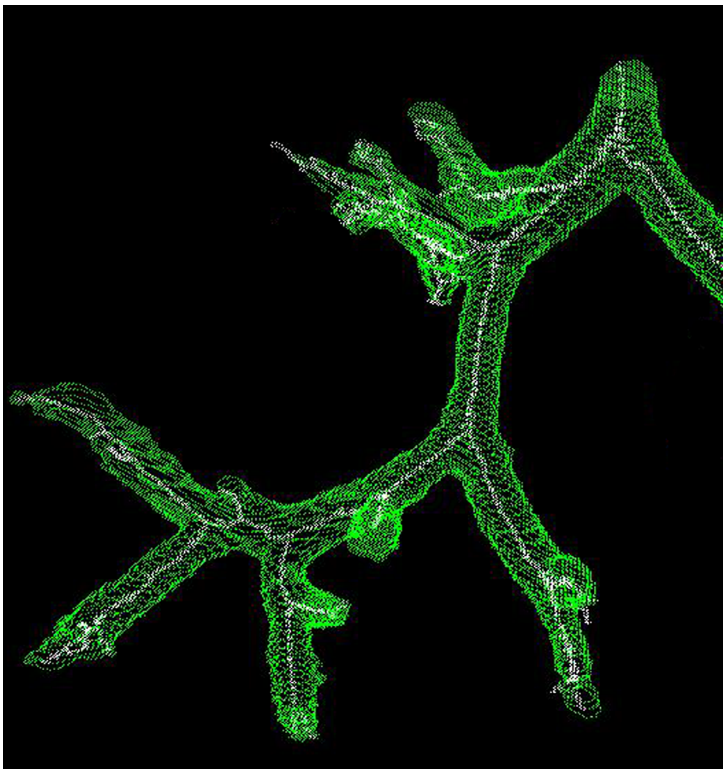

Fig. 3-10 The original outlines of the cross-sections using the threshold method (green) and the middle lines using the three-dimensional thinning algorithm (white).

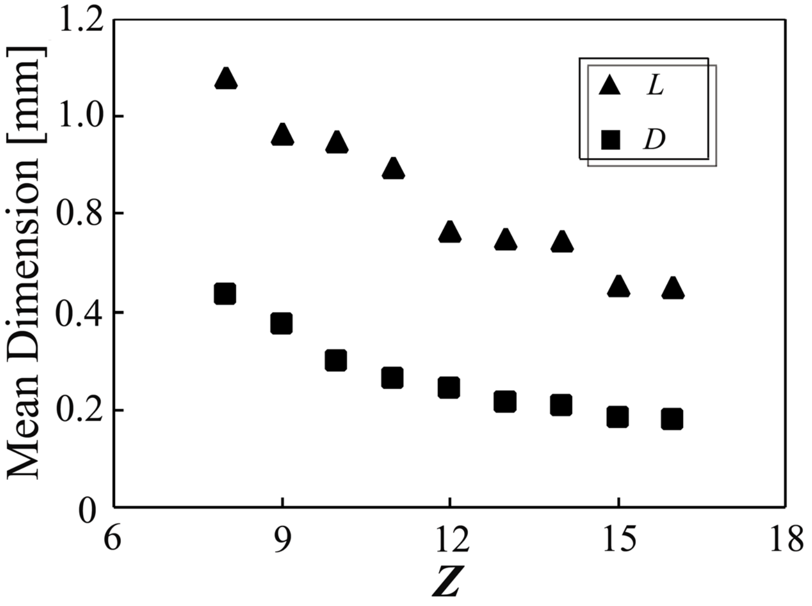

Fig. 3-11 The average diameter *D* (square) and average length *L* (triangle) as a function of ***Z***.

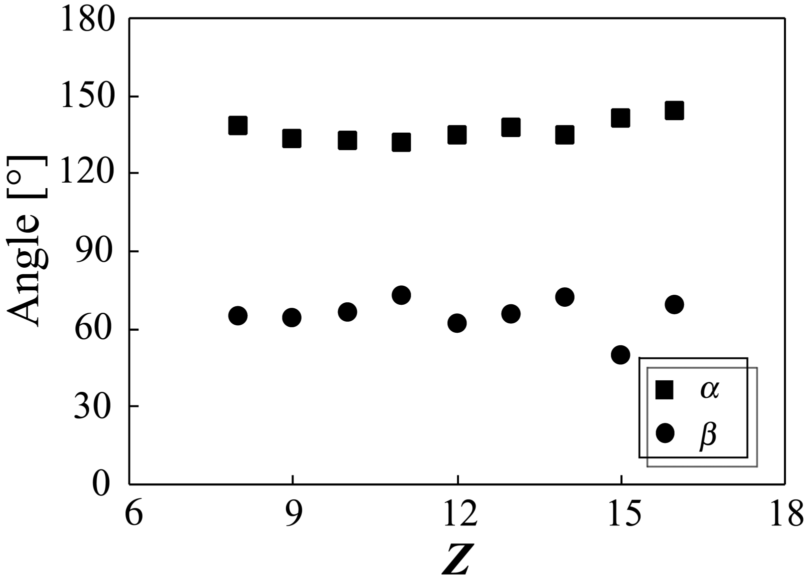

Fig. 3-12 The average branching angle α (square) and gravity angle β (circle) as a function of **Z**.

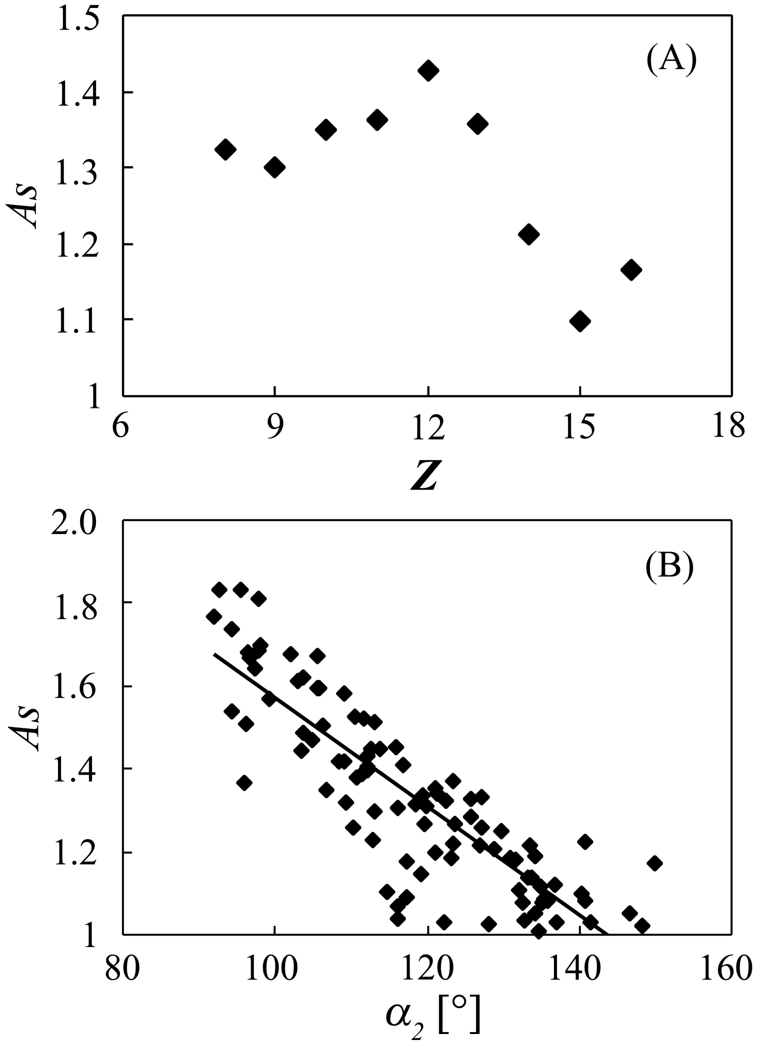

Fig. 3-13 The asymmetry of the branching *As* (A): as a function of *Z*, (B): as a function of α_2. The correlation coefficient R^2 was 0.75.

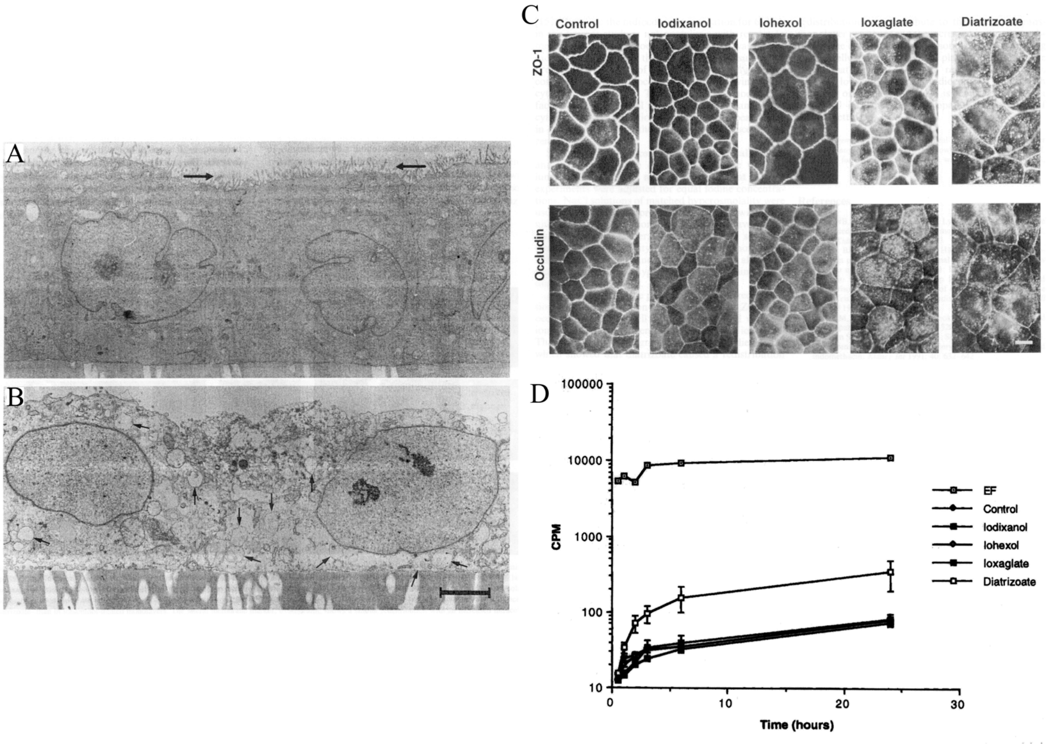

Fig. 3-14 Permeability mechanism of sodium diatrizoate. A & B: TEM images of MDCK (Madin Darby Canine Kidney) cell monolayers (Haller et al., 1997). (A: control, B: after 12 h incubation with 20% diatrizoate. Large arrows: prominent apical microvilli, small arrows: cytoplasma vacuoles. Bar: 2.5 μm.) C: Distribution of plasmalemmal maker proteins (ZO-1 and occluding) of MDCK cell monolayers incubated with radiocontrast agents for 12 h (Schick et al., 1999). Bar: 20 μm. D: Inulin permeability of MDCK cell monolayers (Schick et al., 1999).

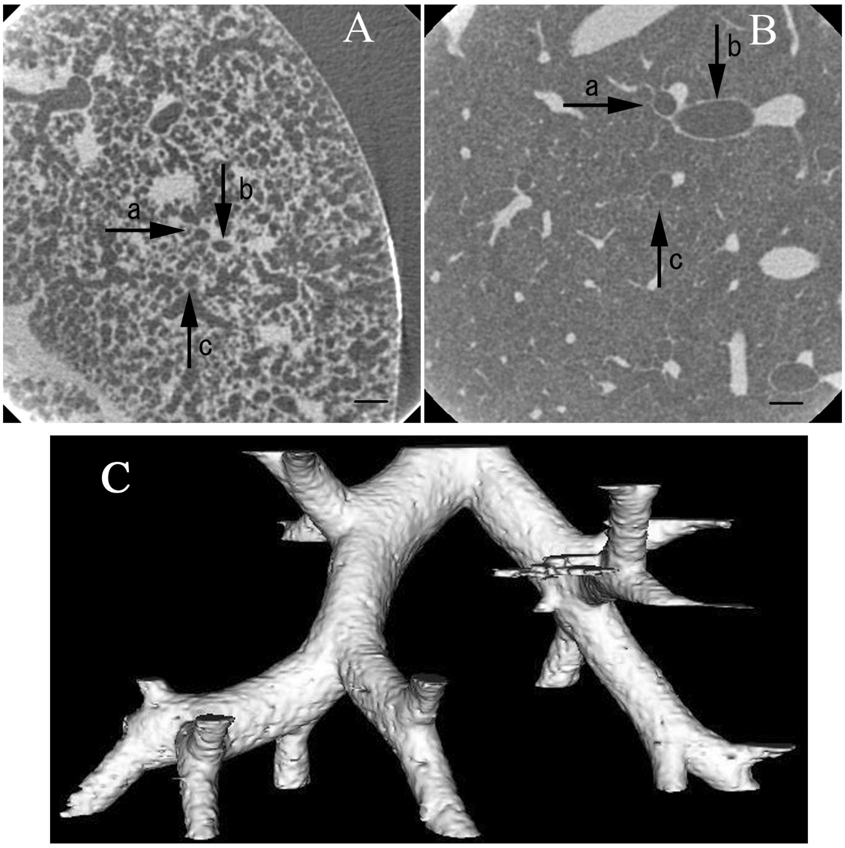

Fig. 3-15 The micro-CT images of the same airways in various lung volumes. (A): the lung volume is FRC and (B): the lung volume is TLC. Same direction arrows (a, b and c) in (A) and (B) indicate the same airways. Bar: 500 μm. (C) 3-D visualization of the same airways as Fig. 4-7C at TLC. The scale is same as Fig. 4-9C. (1 cubic voxel size: 16 μm).

Reference

Castellino RA, and Marshall WH Jr. The urinary mucosal barrier in retrograde pyelography: experimental findings and clinical implications. Radiology 95(2), 403-9, 1970.

Comer JK, Kleinstreuer C, Hyun S, and Kim CS. Aerosol transport and deposition in sequentially bifurcating airways. J Biomech Eng 122(2), 152-8, 2000.

Caro C, Schroter R, Watkins N, Sherwin S, and Sauret V. Inspiratory flow in bronchial airway models: bifurcation plane rotation. In Proceeding of the 4th World Congress of Biomechanics. Calgary, 2002.

Haller C, Schick CS, Zorn M, and Kubler W. Cytotoxicity of radiocontrast agents on polarized renal epithelial cell monolayers. Cardiovasc Res 33, 655-665, 1997.

Heil M, Airway closure: occluding liquid bridges in strongly buckled elastic tubes. J Biomech Eng 121(5), 487-483, 1999.

Lerman A, and Ritman EL. Evaluation of microvessels anatomy by micro-CT. Herz 24(7), 531-533, 1999.

Liu Y, So RMC, and Zhang CH. Modeling the bifurcating flow in a human lung airway. J Biomech 35(4), 465-473, 2002.

Masyuk TV, Ritman EL, and LaRusso NF. Quantitative assessment of the rat intrahepatic biliary system by three-dimensional reconstruction. Am J Pathol 158(6), 2079-2088, 2001.

Nishida M, Inaba Y, and Tanishta K. Gas dispersion in a model pulmonary bifurcation during oscillatory flow. J Biomech Eng 119, 309-316, 1997.

Phalen RF, Yeh HC, Schum GM, and Raabe OG. Application of an idealized model to morphometry of the mammalian tracheobronchial tree. Anatomical Record 190(2), 167-176, 1978.

Phillips CG, and Kaye SR. Diameter-based analysis of the branching geometry of four mammalian bronchial trees. Respir Physiol 102(2-3), 303-316, 1995.

Sauret V, Halson PM, Brown IW, Fleming JS, and Baily AG. Study of the three-dimensional geometry of the central conducting airways in man using computed tomographic (CT) images.

Journal of Anatomy 200, 123-134, 2002.

Schick CS, and Haller C. Comparative cytotoxicity of ionic and non-ionic radiocontrast agents on MDCK cell monolayers *in vitro*. Nephrol Dial Transplant 14, 342-347, 1999.

Tashkin DP. The role of small airway inflammation in asthma. Allergy and Asthma Proc 23(4), 233-242, 2002.

Tsao YF, and Fu KS. A parallel thinning algorithm for 3-D picture. Computer Graphics and Image Processing 17, 315-331, 1981.

Toriwaki J, and Mori K. Distance transformation and skeletonization of 3D pictures and their applications to medical images. In: Bertrand G., Imiya A., Klette R. (Eds.), Digital and Image Geometry, Springer, Tokyo, 412-428, 2001.

Waldron II RL, Bridenbaugh R, Purkerson M, and Dempsey EW. The effect of angiographic contrast media at the cellular level in the brain. Radiology 108, 187-189, 1973.

Weibel ER. Morphometry of the Human lung. New York: Academic, 136-143, 1963.

Zhang YL, Matar OK, and Craster RV. A theoretical study of chemical delivery within the lung using exogenous surfactant. Med Eng and Phys. 25(2), 115-132, 2003.

Zhang Z, Kleinstreuer C, and Kim CS. Effects of curved inlet tubes on air flow and particle deposition in bifurcating lung models. J Biomech 34(5), 659-669, 2001.

Chapter 4

Localized Compliance of Small Airways from Microfocal X-ray Computed Tomography

4.1 Introduction

The intrapulmonay airways, *in situ*, are surrounded by lung parenchyma, and the effective microscopic airway compliance is influenced by the surrounding support (Figs.1-7B & 4-1). The larger intrapulmonary bronchi are surrounded by the peri-bronchial sheath (an invagination of the visceral pleura), which in turn is connected to the alveolar parenchyma. At some anatomically unspecified distance along the peripheral bronchial tree, the bronchi penetrate the peri-bronchial sheath and become directly connected to the parenchyma. As a consequence, the surface pressure acting on the larger bronchi is the pressure within the peri-bronchial space which will be lower (more negative) than the effective pressure exerted by the parenchyma directly as is the case for the smallest airways. Hyatt and Flath (1966) and Takashima et al. (1975) measured diameter and length behavior of large airways (diameter: over 1 mm) and reported that intact airways are stiffer than the excised airways. No accurate measurements have been reported for small intact airways. This chapter hypothesized that small airways were also stiffened in parenchyma and their diameter-volume relationship will not follow that of the surrounding parenchyma. For large airways, the length-volume relationship would be expected to follow the conventional proportionality to $V^{1/3}$ power to reflect the overall need to maintain connectivity and be space filling.

Morphometric changes and "localized compliance" of small airways were determined to establish their mechanical properties. This localized compliance reflects the compliance of restricted regions under “near” physiological conditions in which small airways are embedded in lung parenchyma without dehydration and fixation. The measurements can be used potentially as both a physiological and a clinical index.

In this chapter, the three-dimensional (3D) structure of small airways of an excised rat lung was visualized by using the SCT method (described in chapter 3) and then analyzed the diameter and length of the same small airways at various lung volumes by using a 3D thinning (skeletonization) algorithm, and then evaluated the localized compliance in the airway generation (***Z***) from 8 to 16 was evaluated, where ***Z*** is the number of bifurcations from the trachea to the airway of interest as proposed by Weibel (1963).

4.2 Materials and Methods

4.2.1 *Animal Preparation*

All animals used in the experiments received humane care and the experimental protocol was approved by the Committee of Laboratory Animals according to Keio University guidelines. The excised rat lungs were prepared as following the protocol. Sixteen male Wister rats (300 ± 30 g) were anesthetized with pentobarmital sodium (50 mg/kg i.p.), then inferior vena cava (IVC) was cannulated and perfused with a 0.9% saline solution for 5 min at a flow rate between 5 and 40 ml/min. The IVC was cannulated with the chest open, but during the whole procedure, the lungs were kept inflated at FRC (functional residual capacity). After the saline solution was drained through the pulmonary veins, saline with 0.2 g/ml KCl solution was injected into the IVC to induce cardiac arrest. Sodium diatrizoate solution (0.8 g/ml) (Sigma Chemical, St Louis, MO) was then injected into the pulmonary arteries via the IVC cannula for 1 min at a flow rate between 5 and 40 ml/min. Complete staining of the lungs by the diatrizoate solution was ensured by exposing the preparations to ambient air for 1 h. To prevent desiccation, the moist cotton with a 0.9 % saline solution was put on the lungs. Finally, the lungs were excised, whilst the volume was maintained at FRC and then placed into a Plexiglas cylinder to prevent desiccation during the acquisition of micro-CT images (Fig.4-1).

4.2.2 *Measurements*

The bulk static *P*-*V* curves of the lungs were determined by stepwise inflation of the lungs in 1 ml increments to TLC (total lung capacity) and deflation in 1 ml decrements to FRC. The *P* and *V* of the stained excised lungs in the cylinder could be externally regulated. *P* was measured by using a pressure transducer (Entran, EPI-541-0.35B, NJ), which had been calibrated by using a manometer. The volume TV was defined as FRC plus 2 ml, which approximated the anticipated tidal volume (7 ml/kg). TLC was defined as FRC plus 8 ml, and *P* at TLC was 26.52 ± 2.25 $\mathrm{cmH_2O}$. The lungs were inflated and deflated to various *V* using a 1-ml glass syringe at an accuracy of 0.02 ml, and micro CT images (see next section) were taken.

4.2.3 *Imaging*

The small airways were imaged using a microfocal X-ray CT system (MCT-CB100MF, Hitachi Medical Corp., Japan, Tokyo) (Fig. 4-1). To reconstruct the CT images, a summed projection was acquired at 625 rotational positions. The resolution was 480 × 480 pixels, and 200 slice images per rotation were obtained. To visualize small airway networks, 1 cubic voxel was 16 μm, which meant that 1 square pixel was 16 x 16 μm and the space between each image was also 16 μm. All images of the excised rat lung over a 360° rotation were obtained in 2.5 min. Before taking CT images, the lung pressure was stable for 1 min at each lung volume. If there were air leaks during a sample rotation, the reconstructed CT images had some artifacts due to the high-resolution CT systems. To determine the diameter *D* and length *L* of an airway, the same branching networks were visualized for a *V* ranging between FRC and TLC during a stepwise inflation process in 2 ml increments and the deflation process in 2 ml decrements. The experimental time from the initial to final measurements (including image reconstructions) was less than 2 hours.

4.2.4 *Analysis*

To determine the morphometry of the small airways, the cross-sections of the small airways were identified by using the threshold method (in chapter 3) and then analyzed these cross-sections by using the 3D thinning algorithm of Toriwaki et al. (2002). This algorithm involves the Euclidean distance transformation and repeatedly checks the deletability of points in a sequence in which the Euclidean distance value is small, and finally finds the skeletonized lines and the branching points of the airway network without changing the topology of the airways. However this algorithm left “false” spurs, which was removed “manually” until the middle lines agreed with the input images.

The L and D of the airways were determined by approximating the airway as a cylinder network. The fractions of increase in L and D is δ_L and δ_D, respectively, normalized by L and D at FRC (L_{FRC} and D_{FRC}, respectively) was calculated as follows.

$$\delta_L = \frac{L' - L_{FRC}}{L_{FRC}}, \quad \delta_D = \frac{D' - D_{FRC}}{D_{FRC}}$$

where L' and D' are expressed as L and D at each lung volume.

In this chapter, the localized compliances C_{TV} and C_{TLC} of the airways were evaluated at volumes defined by the volume infused (based on the volume infused by the syringe) to inflate the airways from FRC to TV, and from FRC to TLC as follows.

$$C_{TV} = \frac{(D_{TV}{}^2 \cdot L_{TV} - D_{FRC}{}^2 \cdot L_{FRC})}{\Delta P_{TV} \cdot D_{FRC}{}^2 \cdot L_{FRC}}, \quad C_{TLC} = \frac{(D_{TLC}{}^2 \cdot L_{TLC} - D_{FRC}{}^2 \cdot L_{FRC})}{\Delta P_{TLC} \cdot D_{FRC}{}^2 \cdot L_{FRC}} \qquad (4\text{-}1)$$

To determine ***Z***, the entire lung by using micro-CT (1 cubic voxel of 43 x 43 x 43 μm) was imaged macroscopically and the generation of the airways was identified manually.

4.2.4 *Statistical Analysis*

The size changes and the localized compliance were presented as average values ± SE. as a function of airway generation $\boldsymbol{Z}$ (n = 7 ~ 17 per $\boldsymbol{Z}$) and lung condition (volume V and pressure P) (n = 18 ~ 45 per lung condition). In this chapter, the lungs during inflation process were different from those during deflation process. Differences between inflation and deflation groups and between each lung condition were tested by unpaired t-tests. And differences of δD, δL and compliance between TV and TLC as a function of $\boldsymbol{Z}$ were done by Mann-Whitney U-test. Values of $p < 0.05$ was considered to be statistically significant.

4.3 Results

The 3D structure of the same branching networks at FRC and TCL was reconstructed based on the tomographic images using an isosurface approach in the *Visualization Toolkit* (VTK), which is an open-source, object-oriented software system for 3D computer graphics and imaging processing used by many researchers (*Kitware, Inc.*, http://www.kitware.com/). Figure 4-2 shows the reconstructed 3D structure. The branching networks expanded dramatically in 3D from FRC to TLC. Both D and L of each airway segment were increased at TLC compared with those at FRC, although δ_D was larger δ_L.

4.3.1 *Bronchial Hysteresis*

Figure 4-3 shows the overall pressure – volume relationship for whole lungs with the representative bronchial hysteresis illustrated at a given lung pressure (10 cmH_2O), and Fig. 4-4 shows the same at a given lung volume (TV); the P-V curves and CT images in Figs. 4-3 and 4-4 were obtained from the same lung. By use 1 ml glass syringe, 0.2 ml increments of air were injected into the lungs from FRC to TLC. When P was stabilized, P was measured and further increments of air injected. The entire stained excised rat lung exhibited lung hysteresis in the overall P-V curve (Figs. 4-3 and 4-4, top), and the bronchial D indicated arrows in Figs. 4-3 and 4-4 bottom were larger during deflation than during inflation at the same P and the same volume V. At P = 10 cmH_2O D during deflation (Fig. 4-3D) was 1.28 ~ 1.44 times larger than that during inflation (Fig. 4-3B), and at TV D during deflation (Fig. 4-4D) was 1.21 ~ 1.35 times larger than that during inflation (Fig. 4-4B). These results indicated hysteresis of localized alveolar regions in the vicinity of the small airways.

4.3.2 *Bronchial Diameter*

Figure 4-5 shows the average δ_D at TV and TLC during inflation as a function of $\boldsymbol{Z}$. δ_D increased with $\boldsymbol{Z}$ and δ_{D_TV} and δ_{D_TLC} at $\boldsymbol{Z} = 16$ was statistically larger than at $\boldsymbol{Z} = 8$ ($p < 0.01$) (Fig. 5-5), and δ_D at TLC (δ_{D_TLC}) was significantly larger than at TV (δ_{D_TV}) at $\boldsymbol{Z}$ = 11 ~ 16 ($p < 0.05$). These results are consistent with a previous report (Sittipong and Hyatt 1974).

Figure 4-6 shows the representative changes in the cross-section of a small airway during inflation (A) and deflation (B). During inflation, D remained relatively constant at V between FRC and FRC + 4 ml, and started to increase at V between FRC + 4 ml and FRC + 6 ml. In contrast, during deflation, D remained approximately constant at V between TLC and TLC - 6 ml, and started to decrease at TLC - 6 ml, indicating that the local cross-sectional change shows typical hysteresis observed in the overall lung P-V curve.

Figure 4-7 shows the percentage of average D for the larger ($D > 300$ μm) and smaller airways ($D < 300$ μm) as a function of the percentage of $V^{1/3}$. During inflation process, D for smaller airways was significantly larger at 90 % $V^{1/3}$ than at 80 % $V^{1/3}$ ($p < 0.001$). And D for smaller airways at 80 % $V^{1/3}$ was significantly significantly larger during deflation process than during inflation process ($p < 0.001$). Except for the 90 % $V^{1/3}$ during inflation and 70 % $V^{1/3}$

during deflation for the smaller airways, the percentage of D of smaller and larger airways was appropriate linear function with that of $V^{1/3}$. These results indicated that all airways behaved very similarly and isotropically except a specific lung condition.

Figure 4-8 shows the progressive average δ_D in larger airways ($D > 300$ μm) compared to smaller airways ($D < 300$ μm) during inflation and deflation as a function of P. The localized P-δ_D curves differed between the smaller and larger airways; for smaller airways, D increased by 36% at TV and by 89% at TLC, whereas for larger airways, D increased by 18% at TV and 47% at TLC. The hysteresis for larger airways was fairly moderate, whereas that for smaller airways was more pronounced. For $P = 12$ and 16 cmH_2O, δ_D for smaller airways were significantly larger during deflation process than during inflation process ($p < 0.001$) whilst δ_D for larger airways was statistically not so. During inflation, small airway D increased dramatically at a specific pressure; during inflation process, δ_D for smaller airways was significantly larger at $P = 18$ cmH_2O than at $P = 16$ cmH_2O ($p < 0.001$). This tendency is similar to that previously reported by Naureckas et al. (1994). With further increase in P, small airways D remained relatively constant. During deflation, small airways D gradually decreased as P fell from 23 to 12 cmH_2O, and then decreased dramatically when P reached 12 cmH_2O.

4.3.3 *Bronchial Length*

Figure 4-9 shows the average δ_L at TV and TLC during inflation as a function of $\boldsymbol{Z}$. Although δ_L increased at lower $\boldsymbol{Z}$ as $\boldsymbol{Z}$ increased ($\boldsymbol{Z} = 8 \sim 11$), it remained relatively constant at higher $\boldsymbol{Z}$ ($\boldsymbol{Z} = 12 \sim 16$) at TV and TLC. δ_L at TLC was statistically larger than at TV at $\boldsymbol{Z} = 11 \sim 16$ ($p < 0.05$). This difference was similar to that of δ_D shown in Fig. 4-5, although δ_L was smaller than δ_D in smaller airways (compare Figs. 4-5 and 4-9).

Figures 4-10 show the average δ_L for smaller airways ($D < 300$ μm) during inflation and deflation as a function of (A) $V^{1/3}$ and (B) P. δ_L was not statistically larger during deflation process than inflation process and it changed linearly with *P* during both inflation and deflation, resulting in the absence of hysteresis.

4.3.4 *Bronchial Volume*

Fig. 4-11 shows the average airway volume for smaller airways ($D < 300$ μm) and larger airways ($D > 300$ μm) during inflation and deflation as a function of lung volume. The airways volume was calculated using the formula ($D^2 \times L \times \pi/4$). The values of airway and lung volume were percentage of those at TLC. The airway volume for the larger airways behaved linearly with the lung volume compared from those for the smaller airways, and that differences between inflation and deflation were not statistically so. For the smaller airways, at lower and intermediate lung volume, airway volume was significantly larger during deflation process than during inflation process ($p < 0.001$). And compared from lung volume, during inflation process, the airway volume was smaller under lower lung volume and larger under high lung volume. And, during deflation process, the airway volume was larger under high and intermediate lung volume and smaller under lower lung volume. Similar to *D* as a function of $V^{1/3}$ (Fig. 4-7B), airway volume behaved linearly with lung volume except a specific lung volume.

4.3.5 *Localized Compliance*

The localized compliances (C_{TV} and C_{TLC}) of individual airway segments were determined by using Eq. 4-1. Figure 4-12 shows the average C_{TV} and C_{TLC} as a function of $\boldsymbol{Z}$. C_{TV} and C_{TLC} gradually increased with increasing $\boldsymbol{Z}$, and C_{TLC} was significantly larger than C_{TV} at $\boldsymbol{Z} = 12 \sim 15$ ($p < 0.05$). The average overall C_{TV} and C_{TLC} were calculated as follows.

$$C_{over\_TV} = \frac{TV - FRC}{(P_{TV} - P_{FRC}) \cdot FRC}; \quad C_{over\_TLC} = \frac{TLC - FRC}{(P_{TLC} - P_{FRC}) \cdot FRC}$$

The calculated average C_{over_TV} was 0.06 ± 0.004 and the average C_{over_TLC} was 0.10 ± 0.01, and C_{TV} and C_{TLC} above $\boldsymbol{Z} = 9$ were significantly larger than the overall compliances (C_{over_TV} and C_{over_TLC})

($p < 0.05$).

4.4 Discussion

The localized mechanical properties of small airways are highly affected by surrounding lung parenchyma (Fig. 4-1). In this chapter, the localized airway compliance was defined as the compliance normalized by the airway segment volume at FRC and was found to be similar to normalized lung macroscopic compliance by lung volume at FRC (specific compliance defined as ($\Delta V/(\Delta P$*FRC)). Tiddens et al. (1999) calculated the specific compliance of isolated human small airway segments (average diameter of 1.3 ± 0.39 mm) based on the volume of the segments inflated from 0 to 15 cmH$_2$O in Krebs buffer and reported that the average specific compliance was 0.053. Our results show a smaller compliance; C_{TV} at $\boldsymbol{Z} = 8$ was 0.043 for an airway diameter D of approximately 430 μm (Fig. 4-11). These differences in compliance indicate that the localized compliance is influenced by the surrounding lung parenchyma and surface tension, and that isolated airways are more compliant than intact airways (Hyatt and Flath 1966; Hughes et al. 1972; Takashima et al. 1975). Although compliance is partially influenced by surface tension, in the experiments by Tiddens et al. (1999) the isolated airway segments were placed in an organ bath and were filled with buffer, and thus the effects of surface tension were eliminated. It is well known that a saline-filled lung, which does not exhibit air-surfactant interface or surface tension, is more compliant than a normal lung. Furthermore, small airways in lung parenchyma are surrounded by many alveoli (Fig. 4-1). The alveolar wall acts as a spring, and the localized compliance is determined not only by airway pressure but also by interdependence effects between the airway and alveoli (Menkes et al. 1972; Elad et al. 1988), and therefore isolated airways are more compliant.

The small airways in our study exhibited hysteresis; D was larger during deflation than that during inflation at $P = 12$ and 16 cmH$_2$O ($p < 0.001$) (Fig. 4-8) although L remained relatively constant (Fig. 4-10). The larger airways are inherently stiffer than smaller airways, making diameter behavior of the smaller airways more affected by changes in lung volume of the tissue surrounding them, whereas larger airways are relatively unaffected. Smooth muscle tone and surface tension are important factors in hysteresis (Sakai and Hoppin 1979). Hughes et al. (1972) analyzed the change in bronchial *L* and *D* of excised dog lungs during inflation and deflation by using a tantalum bronchogram technique. They reported that the bronchial segments did not exhibit hysteresis in either *L* or *D*, and explained that the reason was that the surfactant did not completely cover the entire surface of the large bronchi ($D = 0.1 \sim 1.17$ cm). The airway behavior in large airways is hardly affected by airway surfactant, and so exhibits less hysteresis. A saline-filled lung without lung surfactant does not exhibit hysteresis in its *P*-*V* curve. Tiddens et al. (1999) reported that isolated human small airways ($D = 1.3 \pm 0.39$ mm) exhibited hysteresis in the *P*–*V* curve. In their experiments the airway segments were placed in an organ bath and filled with buffer, and the observed hysteresis in the *P*–*V* curve was caused by the behavior of *D*. Shardonofsky et al. (2001) lengthened and shortened dog bronchial segments ($\boldsymbol{Z} = 4$ or 5) in the axial direction in Krebs solution and reported no significant differences in axial strain between the lengthened and shortened airways and reported no hysteresis. Our results are consistent with all of these previous results. However, although Tiddens et al. (1999) reported that *D* gradually increased as *P* increased, *D* changed dramatically at a specific *P* (Fig. 4-8).

This dramatic change in *D* at a specific *P* can be explained as follows. As shown in Figs. 4-8, *D* sharply increased during inflation at $P = 16$ cmH_2O and sharply decreased at $P = 12$ cmH_2O during deflation. This variation in *D* could be closely with the airway opening and closing process. Gaver et al. (1990) studied the airway opening process in experiments using a model and reported that *P* at which *D* sharply increased depended on *D* and surface tension. Naureckas et al. (1994) analyzed *D* of excised rat lungs during inflation by using the tantalum bronchograms obtained by microfocal X-ray imaging, and reported that *D* increased from 400 to 700 μm when the lung pressure was increased slowly from 0 to 25 cmH_2O. Our results showed similar trends (Fig. 4-8) in that *D* gradually increased when the pressure was increased from 0 to 12 cmH_2O, and then the airways appeared to be "pop" open when the pressure was further increased. The opening process of small airways during inflation is determined by tissue elasticity and surface tension. At low *P* before the airways suddenly opened, a balance among tissue elasticity, surface tension, and transmural pressure was maintained, and thus *D* was relatively constant (Fig. 4-8). At a specific *P*, the balance was not maintained, and thus *D* dramatically increased (Fig. 4-8).

All airways did not deform in the same way, the smaller airways expanded and contracted more at lower *P* than did larger airways. In this chapter, early in the inflation, the air space increased but *D* of small airways remained relatively constant, whereas late in the inflation, the air space increased only slightly but *D* dramatically increased (Fig. 4-6A). A key result in our study is that small airways were more compliant at higher $\boldsymbol{Z}$ (Fig. 4-12). Previously, Martin and Proctor (1958) measured the *P*-*V* curve of dog bronchi and reported that peripheral airways were more compliant than central airways. Naurecks et al. (1994) reported that the specific *P* at which the diameter dramatically increased depended on *D* and that *P* was lower in smaller airways. Mercer et al. (1987) analyzed alveolar diameter of fixed rat lungs at various lung pressures, and reported that the diameter increased remarkably between 0 and 10 cmH_2O (between 43.3 ± 2.3 and 100.3 ± 3.3 μm) and was approximately constant above 10 cmH_2O. Their results indicate that, compared with larger airways, the smaller airways opened at lower pressure during inflation. And $\mathrm{d}C_{TV} / \mathrm{d}\boldsymbol{Z}$ increased and $\mathrm{d}C_{TLC} / \mathrm{d}\boldsymbol{Z}$ decreased with increasing $\boldsymbol{Z}$ at higher $\boldsymbol{Z}$ (Fig. 4-12).

Interestingly, the diameter, especially at smaller airways ($D< 300$ μm), did not change linearly with $V^{1/3}$, although as would be expected, the length did (Figs. 4-7 & 4-10). Our results differ from those by Hughes et al. (1972), who reported that there were no differences in *D* and *L* between large and that small bronchi, and that both the diameter and length changed linearly as $V^{1/3}$. And the airway volume for smaller airways did not behave linearly with lung volume, although for larger airways did (Fig. 4-11). Previous studies suggested airways properties were homogeneous. However, the airways wall structure varies along the path. Ma et al. (1997) analyzed the mechanical properties of muscle strips of canine airways of differing generations ***Z*** and demonstrated the heterogeneity of airway smooth muscle, thus indicating that small airways and larger airways may not be expand similarly.

.

4.5 Summary

This chapter is the first to evaluate the localized airway compliance by using the new method described in chapter 3. Compared with the values of *D* and *L* at FRC, *D* was 36% higher at TV and 89% at TLC and *L* was 18% higher at TV and 43% at TLC. All airways did not deform in the same manner. Large airways demonstrated similar inflation and deflation diameter change patterns; however with increasing ***Z***, localized compliance of the small airways exhibited clear hysteresis. During the earlier stages of inflation, small airways inflated similarly to the larger airways, following a path very dissimilar from their deflation path, but above approximately 16 cmH_2O, the small airways experienced a rapid increase in diameter and thereafter followed a path very close to the deflation path at high lung volume.

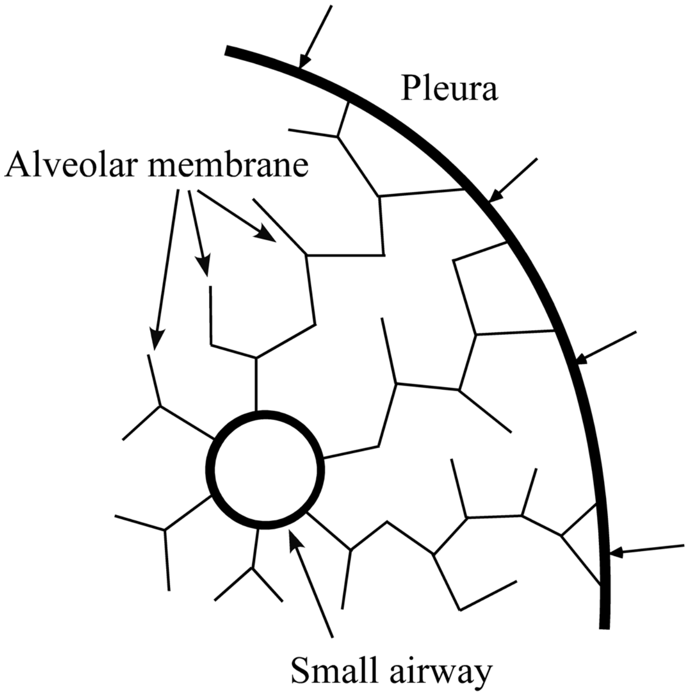

Fig. 4-1 The schematic model of small airway in lung parenchyma.

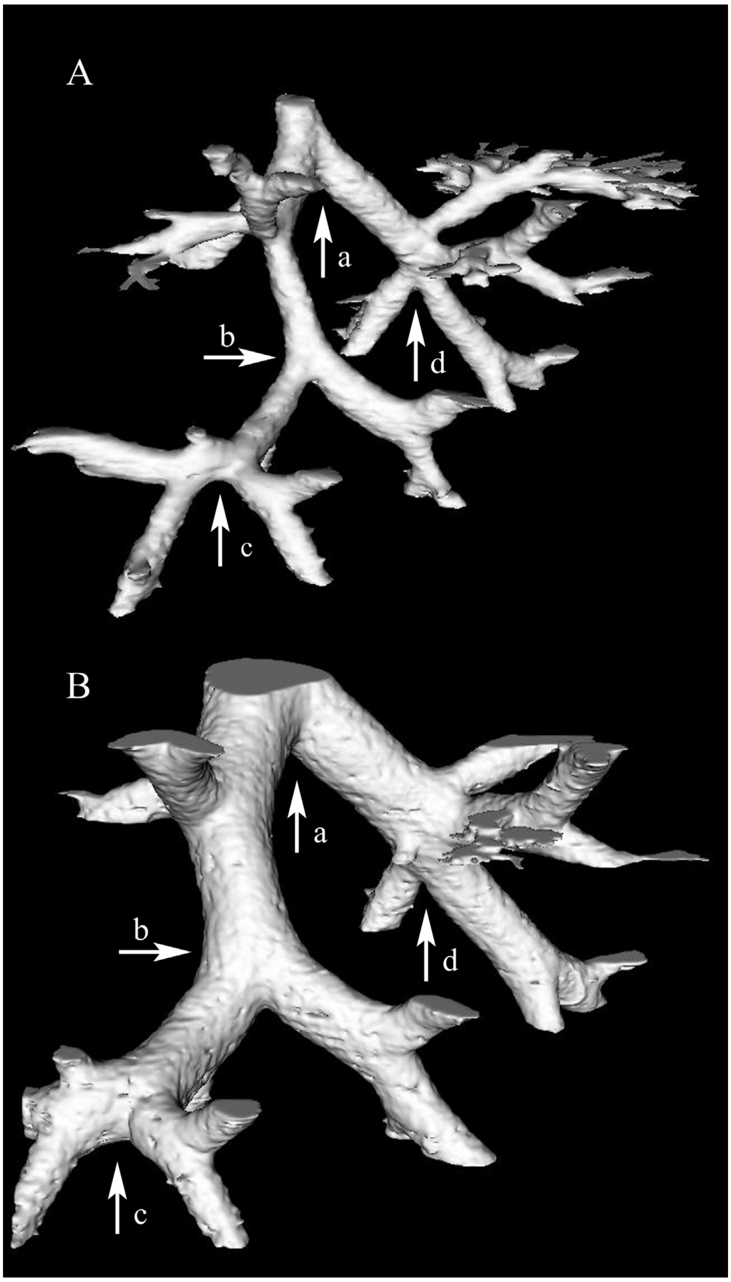

Fig. 4-2 Three-dimensional structures of same branching network at (A) FRC and (B) TLC. Diameter range at FRC: 300 ~ 170 μm. Airway generation ***Z*** range: 10 ~ 16. The arrows (a ~ d) indicated the same dividers in (A) and (B).

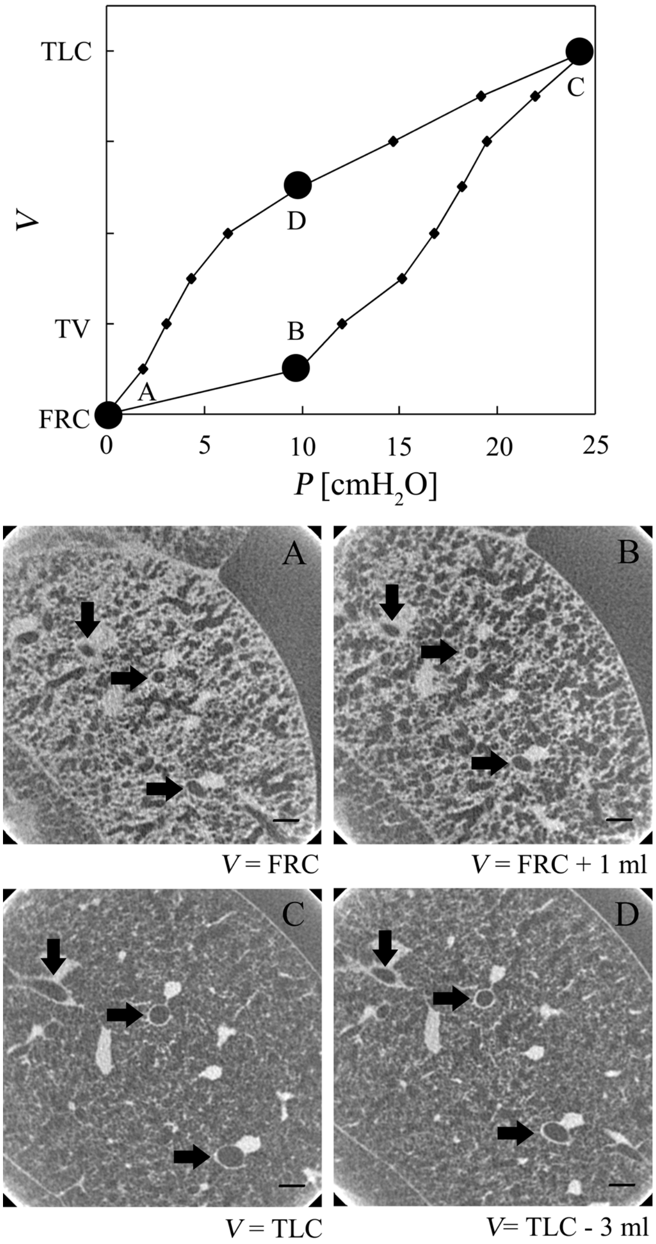

Fig. 4-3 The hysteresis of the small airways against lung pressure (Upper: Pressure-volume curve, Down: micro-CT images.). A: lung volume = 3 ml (FRC), B: lung volume = 4 ml (inflation), C: lung volume = 11 ml TLC, D: lung volume = 8 ml (deflation). The same direction arrows indicated the same airways. The lung pressure at B was approximately equal to at D. Bars: 500 μm.

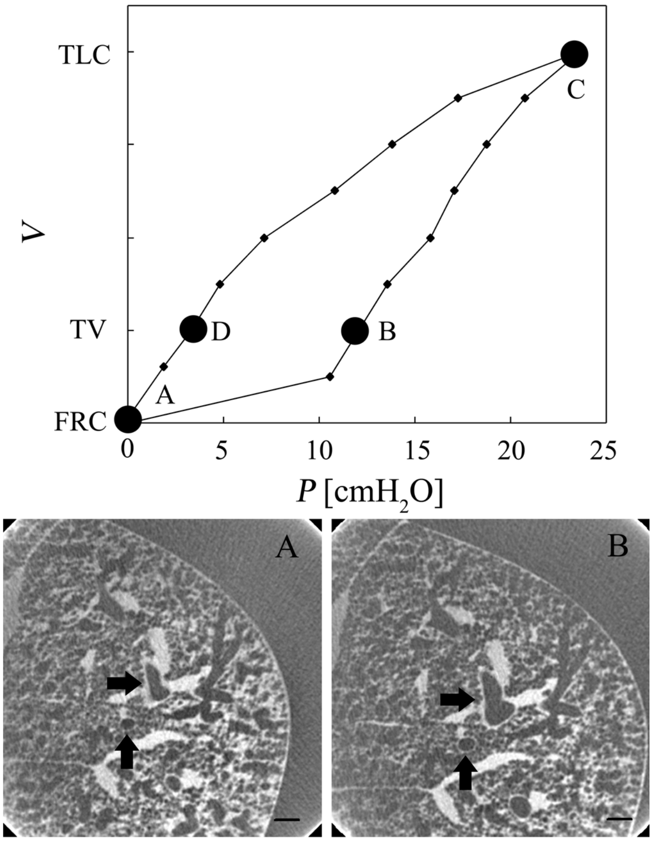

V = FRC V = TV during inflation

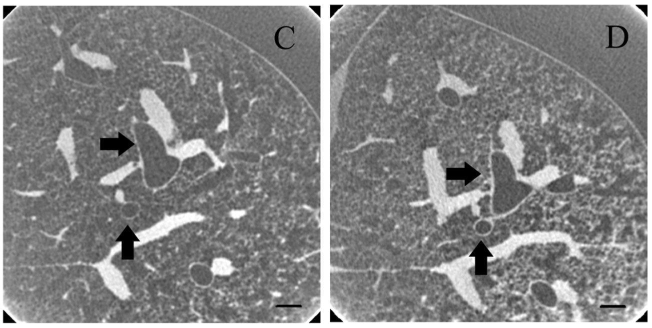

V = TLC V = TV during deflation

Fig. 4-4 The hysteresis of the small airways against lung volume (Upper: Pressure-volume curve, Down: micro-CT images.). A: lung volume = FRC, B: lung volume = TV (inflation), C: lung volume = 11 ml TLC, D: lung volume = TV (deflation). The same direction arrows indicated the same airways. Bars: 500 μm.

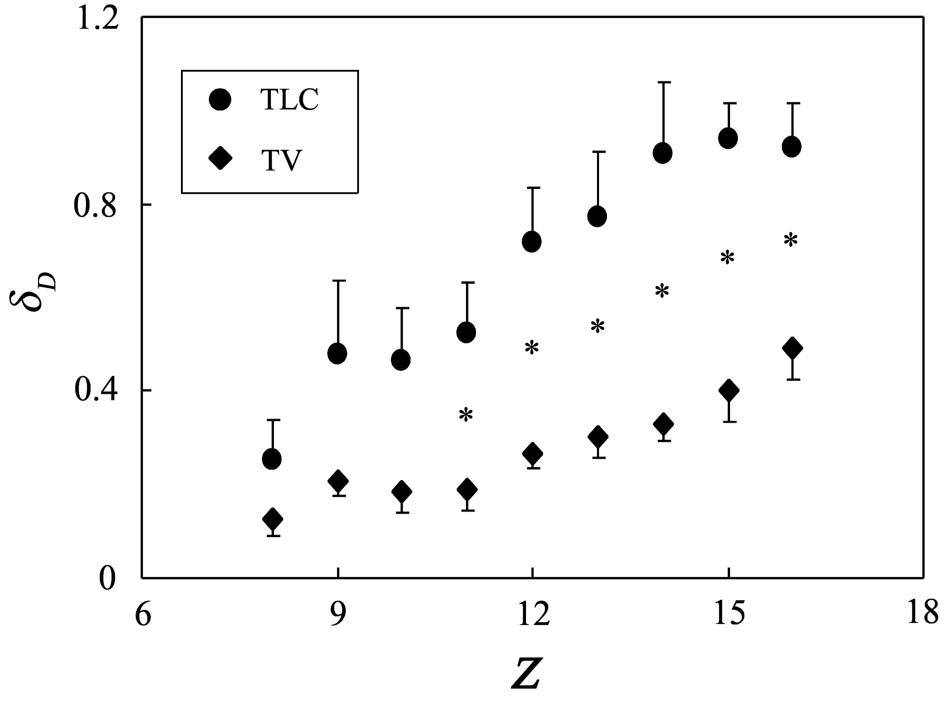

Fig. 4-5 The rate of diameter increase δ_D at TV (diamond) and TLC (circle) as a function of ***Z***. The average diameter at Z = 8 (D_8) was 432 μm and D_{16} was 178 μm. *p (between TLC and TV) < 0.05.

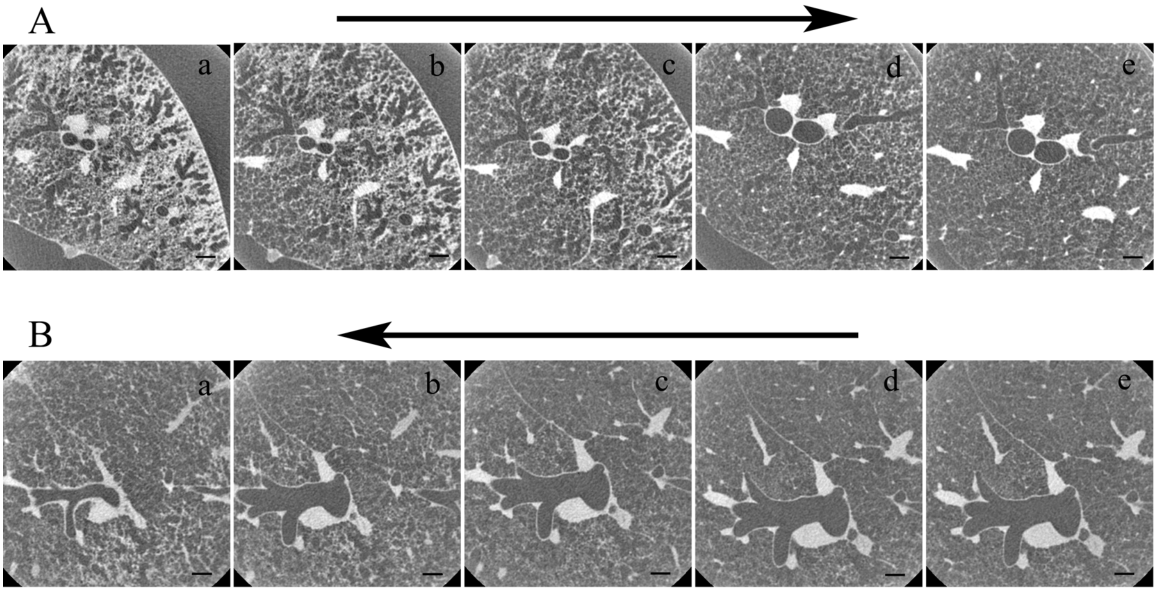

Fig. 4-6 The micro-CT images of the same airways during (A) inflation and (B) deflation. (a: 3 ml (FRC), b: 5 ml, c: 7 ml, d: 9 ml, and e: 11 ml (TLC)). Bar: 500 μm.

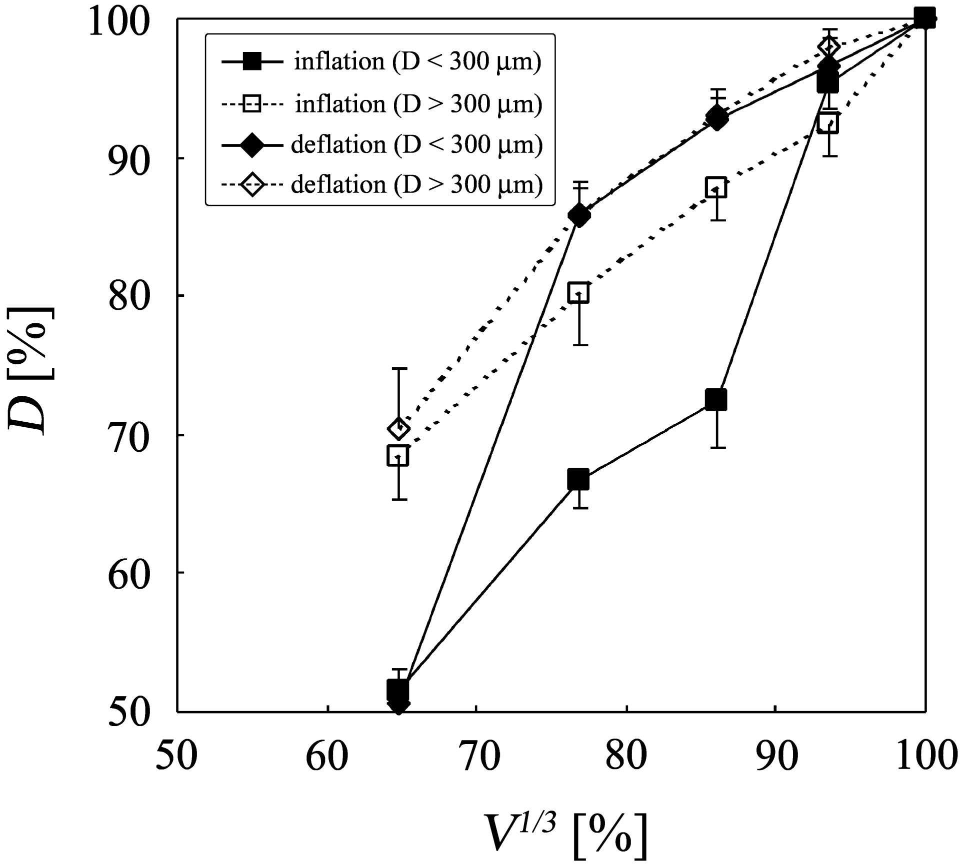

Fig. 4-7 Percentage of diameter (average ± SE.) as a function of $V^{1/3}$ during inflation and deflation. These values were presented average ± SE. FRC defined as 3 ml (10 ml/kg). p (difference of the smaller airways between TV + 2 ml and TV + 4 ml during inflation process) < 0.001.

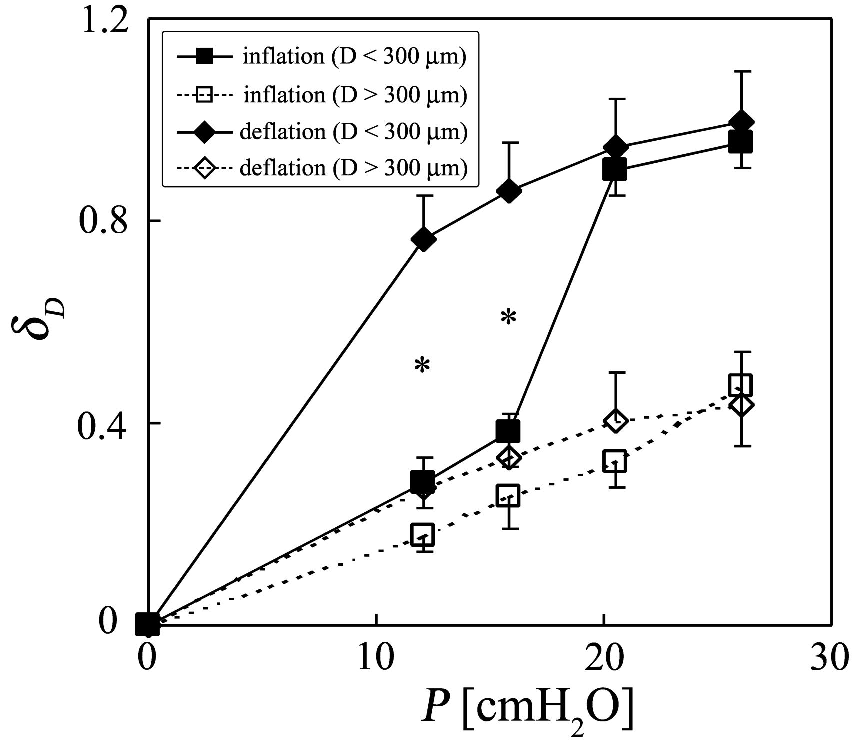

Fig. 4-8 Diameter increase δ_D (average ± SE.) as a function of lung pressure P during inflation and deflation. *p (differences of the smaller airways between inflation and deflation process at 12 and 16 cmH$_2$O) < 0.001 and p (difference of the smaller airways between 16 and 18 cmH$_2$O during inflation process) < 0.001.

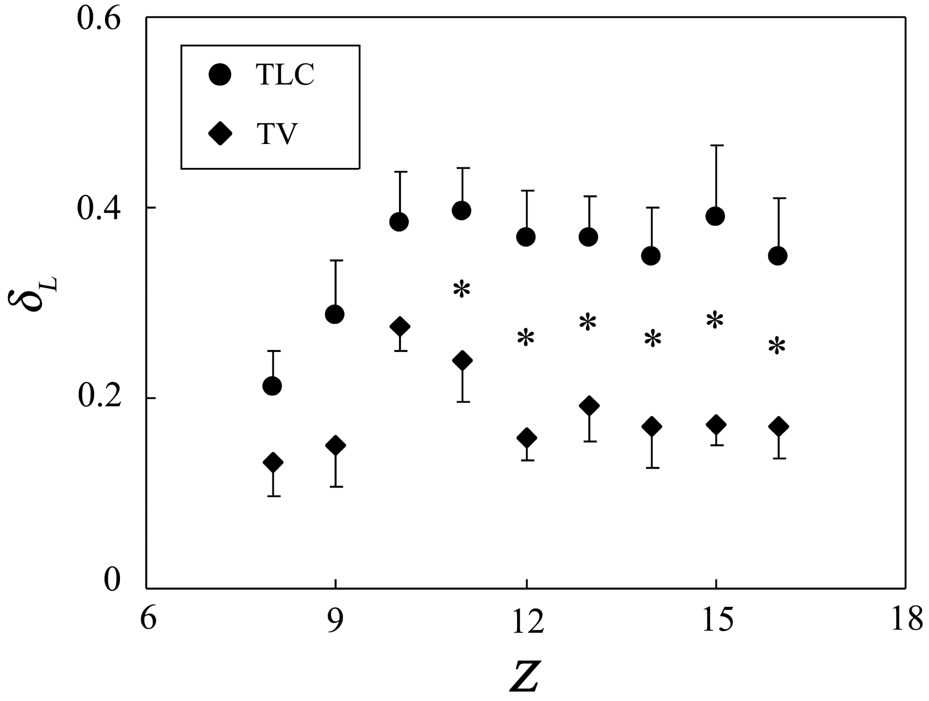

Fig. 4-9 Length increase δ_L (average ± SE.) at TV and TLC as a function of **Z**. Average length at **Z** = 8 (L_8) was 853 μm and **Z** = 16 (D_{16}) was 452 μm (Sera et al. 2003). *p (between TLC and TV) < 0.05.

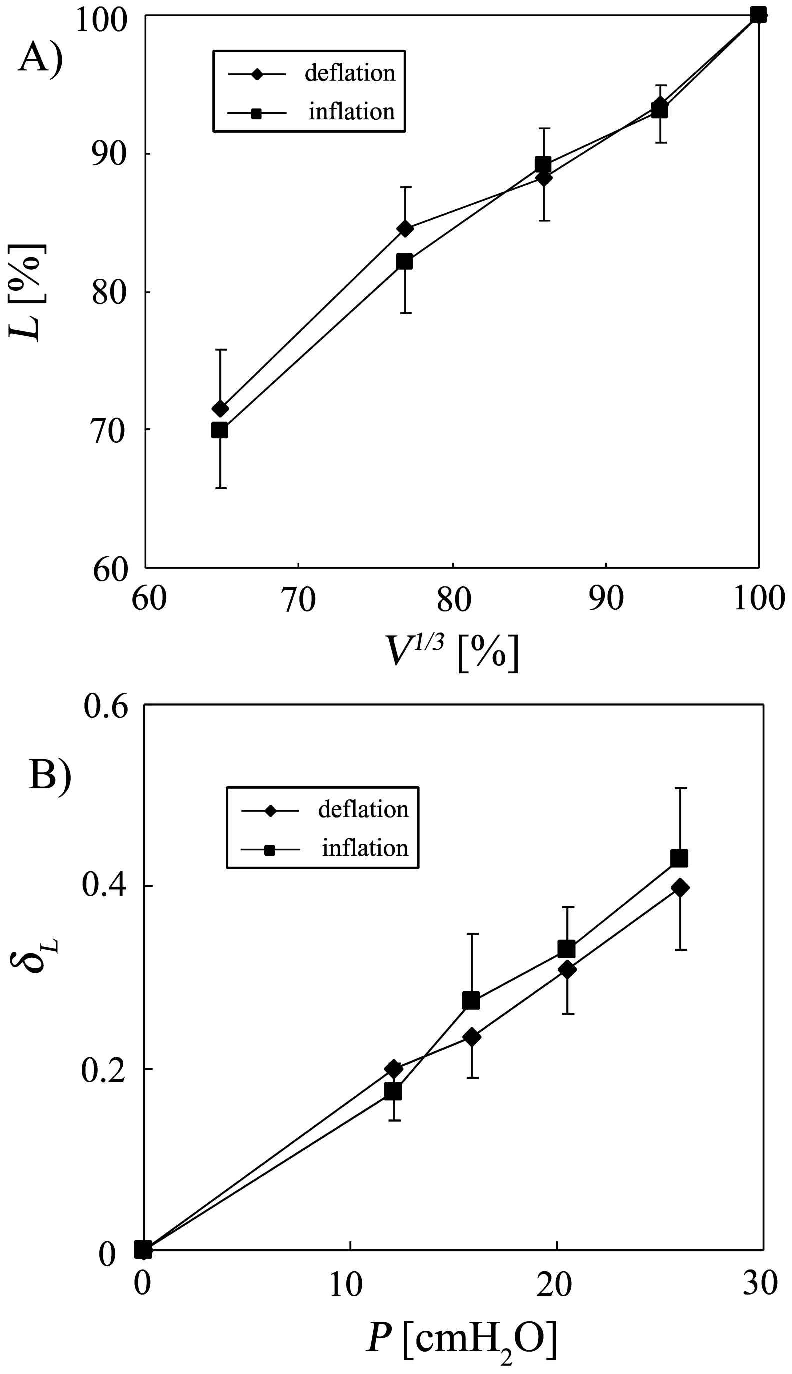

Fig. 4-10 Length behavior for smaller airways (D < 300 μm). (A) Percentage of length (average ± SE.) for smaller airways (D < 300 μm) as a function of $V^{1/3}$ and (B) Length increase δ_L (average ± SE.) as a function of P during inflation and deflation.

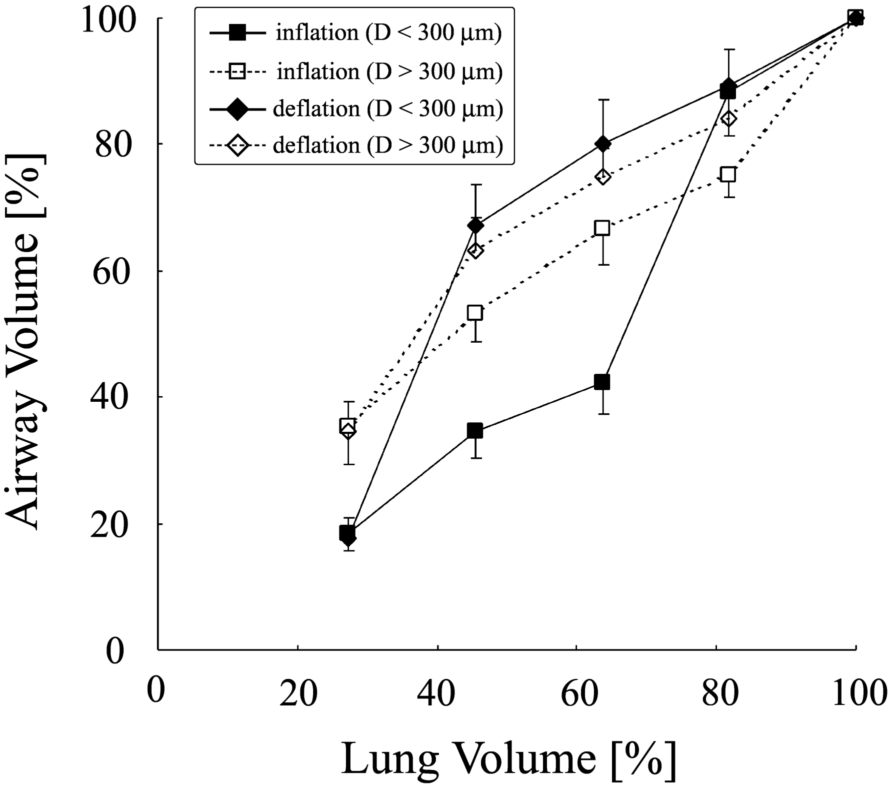

Fig. 4-11 Percentage of airway volume as a function of percentage of lung volume during inflation and deflation. p (differences of the smaller airways between inflation and deflation process at 45 % and 63 % of lung volume) < 0.001 and p (difference of the smaller airways between 63 % and 80 % of lung volume during inflation process) < 0.001.

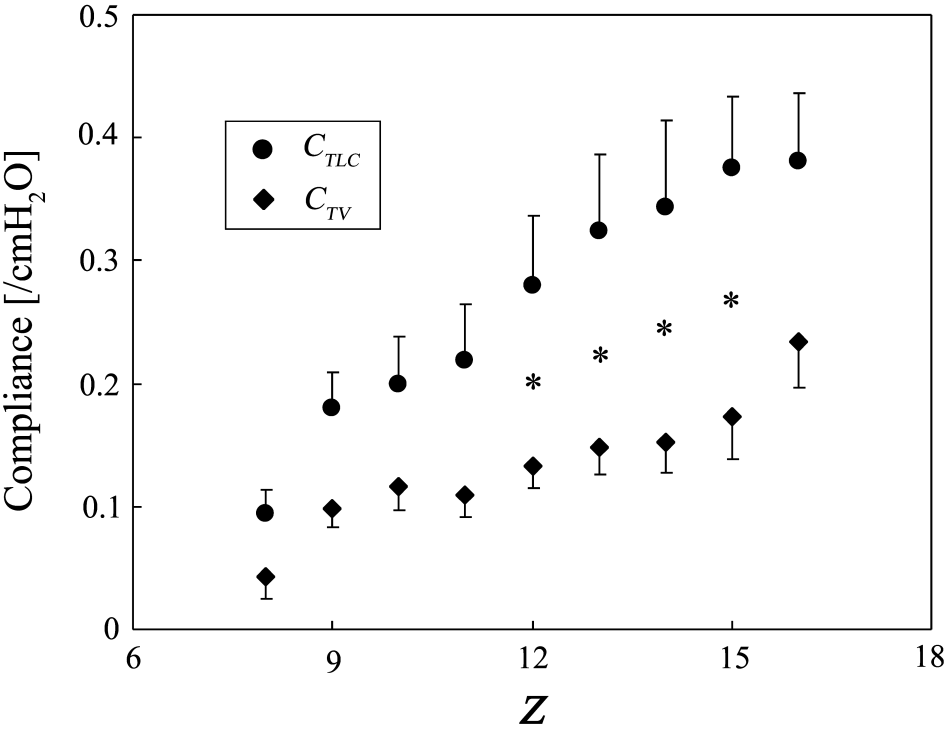

Fig. 4-12 Localized compliance at TV and TLC (average ± SE.) as a function of ***Z***. *p (between TLC and TV) < 0.05.

Reference

Elad D, Kamm RD, and Shapiro AH. Tube law for the intrapulmonary airway. J Appl Physiol 65(1), 7-13, 1988.

Gaver DP 3rd, Samsel RW, and Solway J. Effects of surface tension and viscosity on airway reopening. J Appl Physiol 69(1), 74-85, 1990.

Hughes JM, Hoppin FG Jr, and Mead J. Effect of lung inflation on bronchial length and diameter in excised lungs. J Appl Physiol 32(1), 25-35, 1972.

Hyatt RE, and Flath RE. Influence of lung parenchyma on pressure-diameter behavior of dog bronchi. J Appl Physiol 21(5), 1448-1452, 1966.

Ma X, Li W, and Stephens NL. Heterogeneity of airway smooth muscle at tissue and cellular levels. Can J Physiol Pharmacol 75(7), 930-935, 1997.

Martin HG, and Proctor DF. Pressure-volume measurements on dog bronchi. J Appl Physiol 13, 337-343, 1958.

Menkes H, Gamsu G, Schroter R, Macklem PT. Interdependence of lung units in isolated dog lungs. J Appl Physiol 32(5), 675-680, 1972.

Mercer RR, Laco JM, Crapo JD., Three-dimensional reconstruction of alveoli in the rat lung for pressure-volume relationships. J Appl Physiol. 62(4), 1480-1487, 1987.

Naureckas ET, Dawson CA, Gerber BS, Gaver DP 3rd, Gerber HL, Linehan JH, Solway J, and Samsel RW. Airway reopening pressure in isolated rat lungs. J Appl Physiol 76(3), 1372-1377, 1994.

Sakai H, and Hoppin FG Jr. Hysteresis of contracted airway smooth muscle. J Appl Physiol 68, 1251-1261, 1979.

Shardonofsky FR, Officer TM, Boriek AM, Rodarte JR. Effects of smooth muscle activation on axial mechanical properties of excised canine bronchi. J Appl Physiol 90(4), 1258-1266, 2001.

Sittipong R., and Hyatt RE. Static mechanical behavior of bronchi in excised dog lung. J Appl

Physiol 37(2), 201-206, 1974.

Takishima T, Sasaki H, and Sasaki T. Influence of lung parenchyma on collapsibility of dog bronchi. J Appl Physiol 38(5), 875-881, 1975.

Tiddens HA, Hofhuis W, Bogaard JM, Hop WC, de Bruin H, Willems LN, and de Jongste JC. Compliance, hysteresis, and collapsibility of human small airways. Am J Respir Crit Care Med 160, 1110-1118, 1999.

Toriwaki J, and Mori K. Distance transformation and skeletonization of 3D pictures and their applications to medical images. In: Digital and Image Geometry, edited by Bertrand G, Imiya A, Klette R. Tokyo; Springer, 2001, 412-428.

Weibel ER, Morphometry of the Human lung. New York: Academic, 136-143, 1963.

Chapter 5

Respiratory Flow of Patient with Tracheostenosis

-Effects of Tracheal Compliance-

5.1 Introduction

This chapter focused on respiratory flow of patient with tracheostenosis to investigate the effects of tracheal compliance. Therefore, the flow fields in a mechanical realistic were clarified, especially morphological and distensible, tracheostenosis model by using laser-Doppler velocimeter (LDV) measurements. First, a morphological realistic model was reconstructed, called a "template model", from CT (Computed Tomography) images of a patient with tracheostenosis. Then, this model was used as a template to fabricate two other models: (a) a morphological and distensible realistic test section made of silicone rubber, called a "flexible model", and (b) a morphological realistic test section made of acrylic plastic (Plexiglas), called a "rigid model" to study the effect of the distensibility of airways. Moreover, discussed the possible mechanism of wheeze generation. Wheeze is an important indicator of the degree of obstruction in airways and the generation mechanism is related to flow structure around stenosis.

5.2 Materials and Methods

5.2.1 *Fabrication of test sections*

The template model was a realistic tracheostenosis model based on the CT images of a patient that had with obstructions in the trachea. In the fabrication of this model, contiguous 1.5-mm axial slices (1 pixel = 0.586 × 0.586 mm) of the trachea were taken using a helical CT scanner (GE Yokogawa Medical Systems, Japan). Fig. 5-1 shows (A) typical CT images of a normal trachea,

(B) stenosis trachea and (C) the three-dimensional reconstruction. The stenosis mainly existed at the side of the smooth muscle.

The CT images were digitized and the results were used to form contours of tracheal lumens. To smoothly interpolate tracheal wall profiles, the pixels along the contours were interpolated according to a third-order spline curve in the x-y and y-z planes, and three additional, interpolated layers were inserted between each pair of slices.

After saving the interpolated data to an STL (stereolithography) file, the surface shape of the trachea was determined by forming triangular patches and normal line vectors of each plane, and morphological realistic three-dimensional model was fabricated by using an STL apparatus (SOUP 250GH, NTT DATA CMET INC., Japan). STL is a type of rapid prototyping technology, and arbitrary shapes are formed using an epoxy photopolymer. The pitch of the STL was 0.1 mm.

The template model reconstructed from CT images was about 60 mm long and was from the middle of the trachea to the divider of the bifurcation. Also, the left and right main bronchi were fabricated by using STL. These left and right bronchi at the joints were the same as the CT images at the divider, and so three parts (trachea, left bronchus and right bronchus) matched smoothly at the divider. The radius of each bronchus was only calculated from CT images and the diameter and the angle were based on the Horsfield model (1971). Fig. 5-2 shows a photograph and Table 5-1 shows the geometry of the fabricated realistic model.

Rigid model

The rigid model was fabricated from Plexiglas as follows. First, a realistic cast model made of a low melting point alloy (melting point is 95°C) was created from the template model by first immersing the template model in silicone (RTV–2K(1406), Bayer, Germany). Then the STL model was removed from the silicone and the low melting point alloy was poured into this silicone mold. To eliminate air bubbles trapped in the alloy, the silicone was heated from the outside. Next, the alloy model was embedded in Plexiglas, and the alloy was removed by immersing the

Plexiglas model into a water bath heated to 95°C. Smooth walls were obtained by carefully polishing the test section of Plexiglas.

Flexible model

The flexible model was fabricated from silicon rubber as follows. To simulate the distensibility of actual trachea, local variations of the thickness of the silicone rubber (CX-32-1502, Shinetsu Silicone, Japan) were determined using E_{TS} and E_{TC} that were calculated in Chapter 2. The silicon rubber was transparent enough to measure the velocity fields using LDV and the Young's modulus was 0.53 MPa.

To simulate the motion of the trachea smooth muscle and cartilage rings, a fluid-filled flexible tube was considered. The tube, which is infinitely long, thin wall, isotropic, has the following characteristics: density ρ_0, elastic modulus E, Poisson's ratio γ, wall thickness h and inner radius a, and the density of fluid was ρ. The non-dimensional parameters that describe a flexible tube were described by Dragon and Grotberg. (1991) as

$$P^* = \frac{Mk}{1-\gamma^2} \cdot \frac{W_r^*}{a^{*2}} \tag{5-1}$$

$$M = \frac{\rho_0 h}{\rho a}, \quad k = \frac{Ea^2}{\rho_0 \nu^2} \tag{5-2}$$

Equation (5-1) shows that the displacement of the wall, W_r^*, is linear with the pressure difference between the inside and outside of the tube, P^*, and the behavior of the flexible wall depends on the dimensionless parameter Mk, which includes the wall thickness and Young's modulus of the wall. M is the ratio of the wall mass to the fluid mass and $\sqrt{k}$ is the wave speed ratio, where $\sqrt{E/\rho_0}$ is a characteristic elastic wave speed and ν/a is a characteristic fluid shear propagation speed.

To simulate the motion of the trachea smooth muscle and cartilage rings, the thickness of the silicone was varied so that $Mk = 2.48\times10^8$ for tracheal smooth muscle (Mk_{TS}) and $Mk = 4.89\times10^9$ for cartilage rings (Mk_{TC}). In our model, thickness of the tracheal smooth muscle and cartilage rings was 0.26 mm and 5.1 mm from Eq. (5-2), respectively. In the previous studies the mechanical properties of stenosis is not well known in detail. In this chapter the stenosis existed at the side of the smooth muscle and the wall thickness at the stenosis was set at the same value as the smooth muscle.

The flexible model was fabricated by repeated overlaying and drying of the silicone rubber until the each thickness reached a desired value. The thickness of the cartilage rings and smooth muscle was relatively constant (Fig. 2-1). In this flexible model, although the thickness of the smooth muscle except for the stenosis was uniform (= 0.3 mm), achieving uniform thickness for the cartilage rings and the smooth muscle at the stenosis was difficult because the silicone rubber flowed (due to gravity) during drying and thus collected at the center of the ring. Consequently, the thickness of ring connecting to the smooth muscle was relatively thin (= 3.2 mm), whereas that of the central part of the ring was thick (= 5.2 mm). And the thickness of the smooth muscle at the stenosis, especially at the concavity, was 1.2 mm.

5.2.2 *Measurement of velocity fields and deformation of the cross-sections*

Respiration consists of the two oscillatory flows, inspiration and expiration. However wheezes are generally recorded at low velocity by using a stereoscope for diagnostic purpose (Sano et al., 1995), and in this case the Womersley number is very small, which means that the flow was steady, in both the inspiratory and expiratory directions. Fig. 5-3 shows the flow circuit that was used for velocity measurements. To achieve steady flow, the test sections were placed between the upper and lower reservoir, and flow through the test sections was caused by fluid flowing from the upper to the lower reservoir. The working fluid was a solution of NaI that had the same refractive index as acrylic plastic ($n_a = 1.49$) for the rigid model and as silicone rubber ($n_a = 1.42$) for the flexible model. The velocity profile was measured using LDV as described in the next paragraph, and the seeding particles were TiO_2 with a diameter of 0.63 μm and a density of 4.23 g/cm^3. The wall at the side of the smooth muscle was thin and transparent enough to measure the flow fields in detail using LDV. These seeding particles are hydrophobic, and so they were added with the surfactant into the working fluid. The Reynolds number was 1100, corresponding to a flow rate at the mouth of 0.4 L/s, which is a rate often used for lung sound analysis (Sano et al., 1995). To achieve fully developed inflow, the test sections were connected to straight tubes with a length of 2 m for the trachea and 1 m for the left and right bronchi as entrance region. To ensure realistic physiological flow, the distal branches were connected to linear resistors made of capillary tubes, and the ratio of the flow into the left and right main bronchi was adjusted to 45/55, consistent with the Horsfield model (1971).

Velocity measurements were made by using a two-component LDV (500 mW Ar ion laser: Model 5500A, ILT, Digital Burst Correlator: Model IFA 650, TSI, USA) operated in the backward-scatter mode. The sample volume was a spheroid with a 180-μm major axis and a 34.2-μm minor axis. The fiber-optic probe was mounted on a support that permitted three-dimensional translation and rotation about a vertical axis with an accuracy of 10 μm and 1 deg, respectively. To acquire the maximum intensity of the scattered light, the receiving optics were positioned and focused by hand. The output of the signal processor was digitized with a 12-bit A/D converter at a sampling rate of 1000 Hz. Because an instantaneous velocity was measured by using LDV measurements, the slight dropout in the output signal of the LDV caused deviations from the correct velocity measurements. To remove random fluctuating velocity signals, the averaged velocity w and u were taken. The velocity field around the stenosis was sufficiently complicated that the velocities at 81 locations uniformly positioned over the cross-section of two stations (S_{0a} and S_{0b} shown in Fig. 5-4) were measured. At the bifurcating tubes the velocities at 97 locations positioned over the cross-section of three stations (S_{1c}, S_{1d}, and S_{10e} shown in Fig. 5-4) were measured.

The cross-sections of the flexible model before and after the deformation were obtained by a helical CT scanner (GE Yokogawa Medical Systems, Japan). The pitch between each image was 0.625 mm and 1 pixel was 0.586 × 0.586 mm.

5.3 Results and Discussion

Based on E_{TC}, E_{TS}, and each geometry, the Mk for tracheal smooth muscle and for smooth muscle were calculated from Eq. (5-2). Dragon and Grotberg (1991) assumed that a trachea and all bronchi do not consist of cartilage rings and smooth muscle but a unique flexible tube, and therefore, they plotted k as a function of airway generation for several transmural pressure intervals. Their data were based on the pressure-volume measurements for three different sizes of excised dog bronchi that roughly correspond to the first, fourth, and ninth airway generations. Based on their results, $k = 1.35\times10^8$ and $Mk = 4.9\times10^9$ for a trachea. In our measurements, Mk was larger than Mk_{TS}, but was similar to Mk_{TC}. In real trachea, cartilage rings occupy most but not all of the trachea; however, Dragon and Grotberg determined Mk by assuming that the trachea consists only of one tissue, especially tracheal cartilage rings. However, smooth muscle occupied about 25% of the trachea (Fig. 2-1). Therefore, in our study, Mk was similar to Mk_{TC}. Thus, the flow structure was influenced not only by the cartilage rings but also by the smooth muscle, and thus, Mk_{TS} was much smaller than Mk_{TC} and the smooth-muscle part of the trachea was deformed much more than the cartilage-ring part. In this chapter, to determine the biomechanical characteristics of the cartilage rings and smooth muscle, this localized variation was simulated by varying the thickness of the silicon rubber based on our calculated Mk_{TC} and Mk_{TS}.

5.3.1 *Deformation of the cross-sections of the flexible model*

Figure 5-5 shows photographs of cross-sections at the stenosis and station S_{0b} of the flexible model for a transmural pressure at the entrance of the test section at (A) 0 cmH_2O and (B) 3cmH_2O, both for Re = 1100. The cross-sections of the flexible model expanded, at the part except the stenosis the smooth-muscle side expanded more than the cartilage-ring side. At station S_{0b}, the maximum deformation at the smooth-muscle side was 3.1 mm, whereas that at the cartilage-ring side was 0.3 mm. However at the stenosis the smooth muscle did not expand much and the stenosis constriction hardly changed (from 47 % to 36 %). The smooth muscle at the stenosis, especially at the concavity, was thicker (1.2 mm) than at the part except the stenosis. A stenosis has generally the characteristic of being rigid more than the surrounding tissue, however the mechanical properties of a stenosis, in this study “tumor”, are variable by the place, type and the growth stage and it is not well known in detail. In the flexible model, the mechanical displacement of the stenosis accurately could not be simulated. This causes an uncertainly for describing the flow in stenosis.

5.3.2 *Velocity profiles of inspiratory flow*

Rigid model

Axial velocity profile

In this chapter, w was defined as the axial averaged velocity, u as the secondary averaged velocity component, and $\hat{W}$ as the amplitude of the cross-section average axial velocity. The axial turbulence intensity $\grave{w}_{rms}$ and the secondary turbulence intensity $\grave{u}_{rms}$ are given as

$$\grave{w}_{rms} = \sum_{i=1}^{i=N} \sqrt{(w_i(t) - w)^2} \qquad \grave{u}_{rms} = \sum_{i=1}^{i=N} \sqrt{(u_i(t) - u)^2}$$

For the rigid model, Figure 5-6A shows the contour lines of dimensionless averaged axial velocity ($w/\hat{W}$) and the distributions of dimensionless axial turbulence intensity profile ($\grave{w}_{rms}/\hat{W}$), and Fig 5-6B shows the dimensionless averaged secondary velocity ($u/\hat{W}$) and the dimensionless secondary turbulence intensity profile ($\grave{u}_{rms}/\hat{W}$).

The velocity profile distal to the stenosis (station S_{0a}) was near parabolic. In the post-stenosis region, the asymmetric stenosis induced a recirculation zone and a free shear layer (station S_{0b}). This recirculation zone ended at the bifurcation of the left main bronchus (station S_{1c}). Turbulence energy was generated at the boundary layer (station S_{0b} (a) in Fig. 5-6A) and the free shear layer (station S_{0b} (b) in Fig. 5-6A). The recirculation zone remained in the left main bronchus, and therefore, the turbulence energy induced downstream of the stenosis was mostly transported into the left main bronchus (station S_{1c}). The turbulence energy was greater at the inner of the bifurcation wall, near the divider, than at the outer wall, because the velocity gradient was significantly larger and thus generated more turbulence energy. This turbulence energy that transported into the main left bronchus dispersed over the entire cross-section of the bronchus and then gradually dissipated (station S_{1d}).

Secondary flow profile

The secondary flow, shown in Fig. 5-6B, was influenced by the presence of the stenosis (station S_{0b}) and the bifurcation (stations S_{1c} and S_{10e}). The direction of secondary flow at station S_{0b} was toward the left wall, which was the stenosis side of the trachea. Previous studies report that, in a curved tube, a double secondary vortex is produced (Pedly, 1977; Zhao and Lieber, 1994; Tanaka et al, 1999). In our study, at the left bronchus (station S_{1c}), a helical vortex appeared, similar to results reported by Yoganathan et al. for a pulmonary artery model with asymmetric bifurcation (Yoganathan et al, 1986). Yoganathan et al. measured the velocity profiles for steady flow in arteries with asymmetric bifurcation for various degrees of stenosis (fully opened, 60% mildly stenotic, 80% moderately stenostic and 92% severely stenotic), and found that the flow through moderate and severe stenosis approached a jet and that a large helical flow appeared at a bifurcation with small curvature. In this chpater, this helical vortex decreased in strength at station S_{1d} with increasing distance from the bifurcation.

Flexible model

Axial velocity profile

For the flexible model during inspiratory flow, Fig. 5-7 shows the axial velocity contours and the turbulence intensity distributions (Fig. 5-7A), and the secondary velocity profiles and turbulence intensity distributions (Fig. 5-7B). The axial flow downstream of the stenosis (station S_{0b}) was skewed toward the side opposite the stenosis, and after the bifurcation, the high velocity was skewed toward the inner wall, similar to the high velocity observed in the rigid model. In the post-stenosis region, both a recirculation zone and a free shear layer were formed. The turbulence was generated at the shear layer (station S_{0b} (c) in Fig. 5-7A) and mostly transported to the main left bronchi (station S_{1c}), similar to that observed in the rigid model. The turbulence intensity was much less than that in the rigid model, especially at the smooth-muscle side (maximum intensity was 33% of that in the rigid model). Numerous studies have reported the effects of wall distensibility on the flow field, for example, in an artery or airway model. Schlichting (1979) reported that flow in a distensible tube tended to be stable. Stein et al. (1980) measured (by hot-wire anemometry) the turbulence intensity after the stenosis in steady flow, and reported that the intensity in a distensible tube was 10 ~ 14% lower than that in a rigid tube. Stein et al. also found that, for a Reynolds number between 3000 and 11000, the turbulence intensity in a thick distensible tube (1.6 mm) was less than that in a thin distensible tube (0.8 mm).

Secondary flow profile

The secondary flow downstream of the stenosis (station S_{0b}) in the flexible model differed from that in the rigid model. In the rigid model, the secondary flow at the cartilage-ring side and smooth-muscle side was skewed toward the stenosis side, whereas in the flexible model, the secondary flow reversed its flow at the smooth-muscle side due to the asymmetric stenosis geometry. The smooth muscle at the stenosis did not expand much and the stenosis constriction did not change much, however the turbulence intensity of the secondary flow was 47% of that in the rigid model. At the left bronchus (station S_{1c}), a helical vortex appeared, similar to that in the rigid model, however the intensity was 60% of that in the rigid model. Yoganathan et al. (1986) reported that the turbulence energy and secondary flow motion for mild stenosis were smaller than those for moderate and severe stenosis, results that are consistent with our results, namely, at the right bronchus (station S_{10e}), a Dean-type secondary vortex was observed.

5.3.3 *Velocity profiles of expiratory flow*

Rigid model

Axial velocity profile

For the rigid model during expiratory flow, Fig. 5-8A shows the contour lines of dimensionless -averaged axial velocity and the distributions of dimensionless axial turbulence intensity profile, and Fig 5-8B shows the contour lines of dimensionless averaged secondary velocity and the dimensionless secondary turbulence intensity profile.

The inflows at stations S_{10e} and S_{1d} from the daughter tubes (both the left and right main bronchi) were near parabolic. The maximum axial flow upstream of the stenosis (station S_{0b}) was skewed toward the right wall due to the presence of stenosis in the left wall and to the high flow rate from the right bronchi. The turbulence was produced by the merging flow (station S_{0b} (d) in Fig. 5-8A). In the downstream of the stenosis, a reversed flow appeared and the turbulence intensity was high at the free shear layer (station S_{0a} (e) in Fig. 5-8A).

Secondary velocity profile

In the left and right main bronchi, a weak secondary vortex developed (stations S_{1c} and S_{10e}). At the bifurcation (station S_{0b}), a strong anticlockwise secondary flow developed at the right wall due to the asymmetrical stenosis geometry. When no obstruction is in the trachea, the merging flow from each bronchus creates double vortices in half of the cross-section due to the merging of the secondary vortices induced in each bronchus (Tanaka et al., 1999). A secondary flow downstream of the stenosis (station S_{0a}) in expiratory flow was similar to that observed in inspiratory flow (station S_{0b}).

Flexible model

Axial velocity profile

For the flexible model during expiratory flow, Fig. 5-9 shows the axial velocity contours and the turbulence intensity distributions (Fig. 5-9A), and the secondary velocity profiles and turbulence intensity distributions (Fig. 5-9B). The axial flow upstream of the stenosis (stations S_{0b}, S_{1c}, S_{1d}, and S_{10e}) in the flexible model was similar to that observed in the rigid model. The flow after the bifurcation (station S_{0b}) was skewed toward the right wall, and although turbulence was produced at the boundary layer (station S_{0b} (f) in Fig. 5-9A) because of the merging flow, the maximum intensity was only 77% of that observed in the rigid model. Moreover, in the post-stenosis region (station S_{0a}), the maximum turbulence intensity was only 64% of that observed in the rigid model, and both the flow separation and reversed flow were negligible. Although the velocity gradient at the smooth-muscle side was strong, the turbulence intensity produced at the boundary layer was much stronger at the cartilage-ring (station S_{0a} (g) in Fig. 5-9A), suggesting that the more compliant wall decreased the turbulence production rate that was produced at the boundary layer.

Secondary velocity profile

The secondary flow and the turbulence energy were lower in the pre-stenosis and post-stenosis regions in the flexible model during expiratory flow, similar to that observed during inspiratory flow and that reported previously (Schlichting, 1979; Stein et al., 1980). At the bifurcation (station S_{0b}), anticlockwise secondary flow was observed, similar to that observed in the rigid model, although the intensity was 81% as high as that in the rigid model. Moreover, the secondary flow downstream of the stenosis (station S_{0a}) was negligible. The turbulence intensity downstream of the stenosis (station S_{0a}) decreased, and this decrease was greater at the smooth-muscle side than at the cartilage-ring side.

5.3.4 *Effect of wall distensibility*

In this chapter, the turbulence intensity dramatically decreased, especially at the smooth-muscle side. The wall oscillation of the flexible model was measured by using a laser displacement meter (KEYENCE, LX2-03, Japan) with the sensitivity of 10 μm. No oscillation was observed. The cross section of flexible tube increased due to the pressure (Fig. 5-5) and this geometry change of cross section caused the reduction of turbulence production rate due to the decreased the mean velocity gradient. The maximum intensity in the flexible model in inspiratory flow was 33% of that in the rigid model, and only 64% in expiratory flow. In this chapter, stenosis was in the trachea distal to the bifurcation, and therefore, during the inspiratory phase the turbulence energy produced at the boundary layers and the free layer at stenosis was transported into daughter tubes that were curved. However, during the expiratory phase the turbulence was transported into the straight tube. Because secondary flow produced in a curved tube tends to stabilize the flow (Sreenivasan and Strykowski, (1983)), the turbulence production during inspiratory flow decreased much more dramatically than during expiratory flow.

The secondary flow motion was smaller in the flexible model than in the rigid model. During inspiratory flow in the left bronchus (station S_{1c}), a helical vortex appeared in the flexible model as well as in the rigid model, although the intensity was 60% as large as that in the rigid model. Similar to our findings, Yoganathan et al. (1986) found that the secondary flow motion for mild stenosis was smaller than that for severe stenosis. In the model by Yoganathan et al., the stenosis was upstream of the bifurcation. In this chpater, during expiratory flow the stenosis was downstream, and therefore, our results for this flow cannot be compared with the results by Yoganathan et al. In expiratory flow, the secondary flow intensity at station S_{0b} for the flexible model was 81% as strong as that for the rigid model, and that at station S_{0a} was negligible.

The spatial variation of wall distensibility influenced the flow structure and the turbulence energy. Firstly, the secondary flow direction and intensity was influenced. In inspiratory flow downstream of the stenosis (station S_{0b}) in the flexible model, the secondary flow direction was reversed at the smooth-muscle side and its intensity decreased. Secondly, in the flexible model, the flow separation at station S_{0a} in expiratory flow did not appear, whereas it did appear at station S_{0b} in inspiratory flow. Flow separation in expiratory flow appeared at the smooth-muscle side, whereas in inspiratory flow it appeared at the cartilage-ring side. Thirdly, the turbulence production rate was less in the flexible model than in the rigid model, and this reduction was greater at the smooth-muscle side.

5.3.5 *Mechanism of wheeze generation*

The generation of respiratory sounds, especially “wheezes”, is commonly related to obstructive airway diseases. The generation of a wheeze is related to wall vibration and to flow structure (turbulence), both of which are induced by stenosis. Forgacs (1978) suggested that wheezes are similar to the sound generated by a child’s toy trumpet and that the pitch of a wheeze is determined by the mass and elastic properties of the airway tissue. Gavriely et al. (1984) measured the time and frequency domain characteristics of breath sounds in asthmatic patients and in nonasthmatic patients and measured the frequency of wheezes, and concluded that major causes of wheezes are vortex-induced wall resonance and fluid dynamic flutter. Gavriely and Grotberg. (1988) measured the flow rates and wheezes in excised dog lungs to evaluate the influence of wall distensibility on wheeze generation, and found that the flow rate was limited and thus did not increase, “the critical point”, and that the wheezes were generated at that point in the flexible excised lungs. Gavriely et al. (1989) also studied flutter in collapsible tubes as a possible mechanism for wheeze generation, and found that tube wall oscillations produced loud sounds only when the tubes were buckled and the flow was limited. They compared their experimental results with predictions from flutter theory and from vortex-induced wall vibration mechanisms, and concluded that wall flutter in compliance tubes was the probable mechanism that causes oscillations.

Wheezes are an important indicator of the degree of obstruction in airways, and therefore, many medical groups have recently proposed that wheezes be used as a clinical diagnostic index for obstructive airway diseases (Sachez et al., 1993; Malmberg et al., 1994 & 1995; Sano et al., 1995; Takase and Pasterkamp, 1997), and have suggested that changes in the spectral curves of wheezes could be used as an indicator of the degree of airway constriction. However, before wheezes can be used as a clinical diagnostic index, flow-field patterns around stenosis must be clarified and possible mechanisms of wheeze generation in biomechanical situations (geometry and compliance) must be determined. The stenosis models used in previous studies were ideal; namely, the stenosis geometry was either cylindrical and symmetrical or asymmetrical with uniform distensibility. To accurately identify wheeze generation modes in real lungs, however, more realistic models are needed.

Currently, as described above, this mechanism is explained by the following three factors: (a) vibration of the bronchial walls, which therefore act as resonators, (b) vortex-induced resonators, and (c) wall flutter, which is related to the flow limitation. The mechanism of wheeze generation was investigated by focusing on flow disturbance, namely, the turbulence intensity downstream of the stenosis (station S_{0b}) in inspiratory flow and downstream of the stenosis (station S_{0a}) in expiratory flow. In the flexible model, the maximum turbulence intensity during expiratory flow was 2.1 times higher than that during inspiratory flow. Moreover, the power spectrum of the axial velocity was analyzed at the maximum turbulence intensity during inspiratory flow (downstream, i.e., station S_{0b}) and during expiratory flow (downstream, i.e., station S_{0a}). Figures 5-10A and 5-10B show the power spectra of the axial velocity during inspiratory flow (solid lines) and expiratory flow (dotted lines) for the rigid model and flexible model, respectively. In the rigid model, there was no difference between the inspiratory and expiratory flows. In the flexible model, especially at low frequencies, the power spectrum was significantly stronger during expiratory flow than during inspiratory flow.

Normal breath sound is produced by turbulent flow in a bifurcating network, and the sound intensity during expiration is stronger than during inspiration. Using a microphone, Kraman et al. (1990) measured the sound in a flexible model of canine airways in 31 airways between 2.0 and 19.0 mm in diameter at airflow rates from 0 to 2.5 L/s during inspiratory and expiratory flows. They found that during the expiratory phase, the sound amplitude was approximately linear to the airway cross-sectional area, and during inspiratory phase, the maximum amplitude occurred in airways that were 5 to 8 mm in diameter. They suggested that the predominant lung sounds were produced in the large airways during the expiratory phase and in the medium airways during the inspiratory phase. Using a microphone attached to the neck and over the trachea, Nakamura et al. (1995) analyzed breath sounds during inspiration and expiration, and found that the power spectra were significantly stronger during expiration than during inspiration at any bandwidth above 400 Hz. Kraman et al. (1998) also recorded the breath sounds over the trachea of adults by using contact sensors and measured the airflow by using a pneumotachograph. They analyzed the power spectra of breath sounds for a target airflow of 0.7 L/s, and found that the power was slightly stronger during expiration than during inspiration at any bandwidth under 1000 Hz.

In this chapter, a flow rate at the mouth of 0.4 L/s was used. Wheezes are generally recorded at low velocity by using a stereoscope for diagnostic purposes, although a normal healthy person can generate a wheeze during forced expiratory flow. Sano et al. (1995) analyzed the power spectrographs of breath sounds at airflow rates of 0.3 ~ 0.8 L/s in patients that had pulmonary emphysema, and found that high velocity, such as 1.0 and 2.0 L/s, increased the amplitude of noise, but that this noise was not a wheeze.

To confirm the contribution of the first and third factor mentioned above (i.e., vibration of bronchial walls) to wheeze generation, the wall oscillation of the flexible model was measured by using a laser displacement meter. No oscillation was observed, indicating that wall oscillation did not contribute to wheeze generation at low flow. The third mechanism, "wall flutter, which is related to the flow limitation" is occurred at the high flow and the forced expiratory flow (Gavriely et al., 1987). Gavrielry and Grotberg (1988) demonstrated the relationships between wheezes and flow limitation in normal subjects, and reported that flow did not increase over a critical point (31 ± 3 l/min) even if the pressure increased and wheezes were generated during this plateau of flow. However, wheezes are recognized at low velocity for diagnostic observation (Sano et al., 1995) and so this chapter focused on the wheezes generated at low flow (24 l/min). The wall oscillation of the flexible model measured by using a laser displacement meter with the sensitivity of 10 μm and did not observe the wall oscillation, however the turbulence intensity in expiratory flow was about twice that in inspiratory flow, and larger vortices existed in post-stenosis in expiratory flow. These results indicated that the mechanism of wheezes generation was different between the low flow and the high flow; the mechanism is large vortices at low flow and it is wall flutter and flow limitation at high flow.

In this section, we discussed the airflow structure around stenosis to investigate the possible mechanism of wheeze generation. The sound induced around stenosis may be absorbed and resonated during transmission. This possible mechanism (large vortices) is the initial origin. To investigate this mechanism in detail and use wheezes as a clinical diagnostic index, it is necessary to combine the airflow and the sound transmission into thorax. The acoustic property of thorax will be evaluated in detail.

5-4 Summary

The maximum intensity in the flexible model in inspiratory flow was 33% of that in the rigid model, and only 64% in expiratory flow. The cross section of flexible tube increased due to the pressure and this geometry change of cross section caused the reduction of turbulence production rate due to the decreased the mean velocity gradient. Turbulence intensity during expiratory flow was 2.1 times greater than that during inspiratory flow. The spatial variation of wall compliance influenced the flow in the airway and the turbulence production rate decreased faster at smooth muscles. Turbulence induced at stenosis, such as large vortices, possibly contributes to wheeze generation at low flow.

Table 5-1 Geometry of a template model fabricated by STL apparatus. ([ ] is Horsfield model).

Branch (No)	Diameter (mm)	Angle (deg)	Radius (R/2a)	Flow rate (%)
Trachea (0)	17[18]	-	-	100
Main left bronchus (1)	12[12]	73[73]	4.8[4.5]	45
Main right bronchus (10)	11[11]	35[35]	3.2[3.5]	55

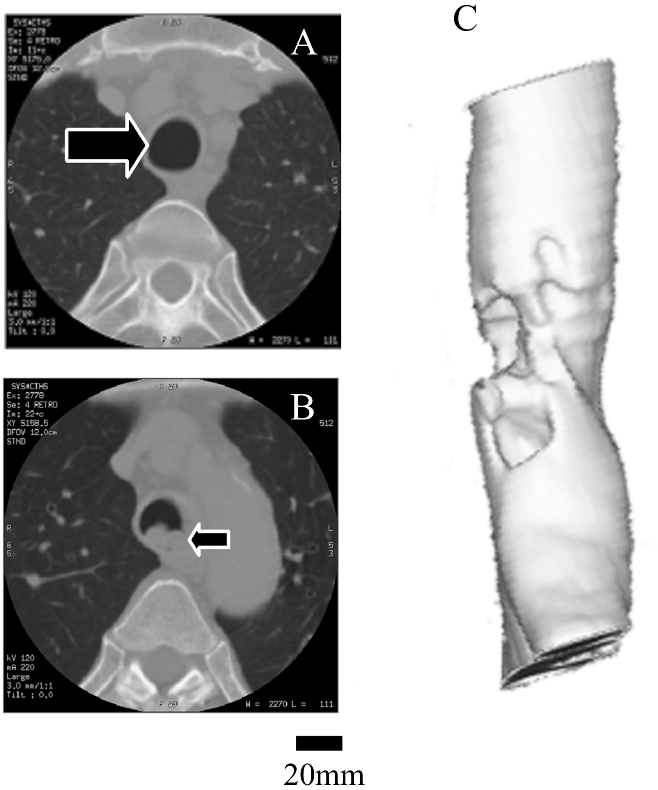

Fig. 5-1　CT images showing normal (A), abnormal stenosis (B) and three-dimensional image (C).　Large arrows show a trachea and small arrow shows a stenosis.　The stenosis constriction was 47 %.　The bottom side of A and B and the left side of C is smooth muscle side.

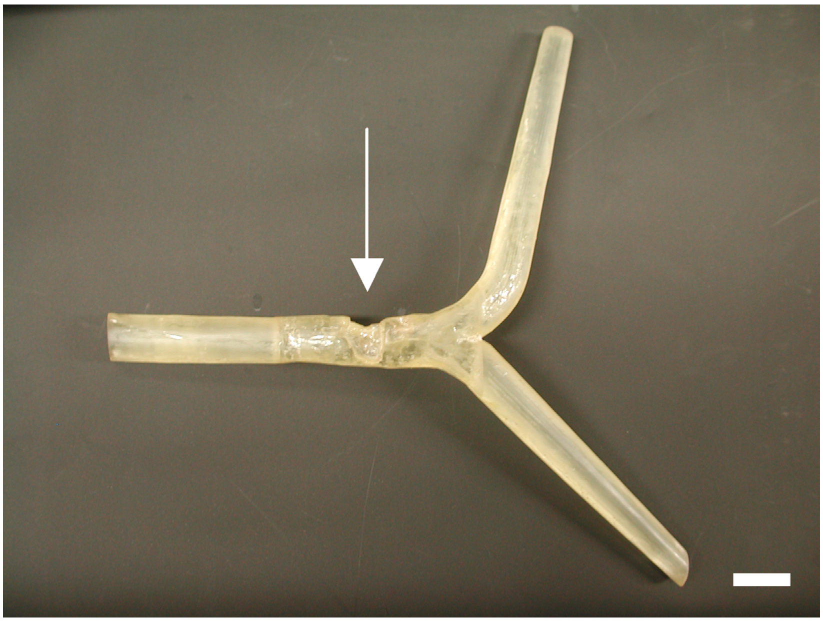

Fig. 5-2 Photograph of the realistic model fabricated by using stereolithography. Arrow indicates stenosis. Scale bar: 20 mm.

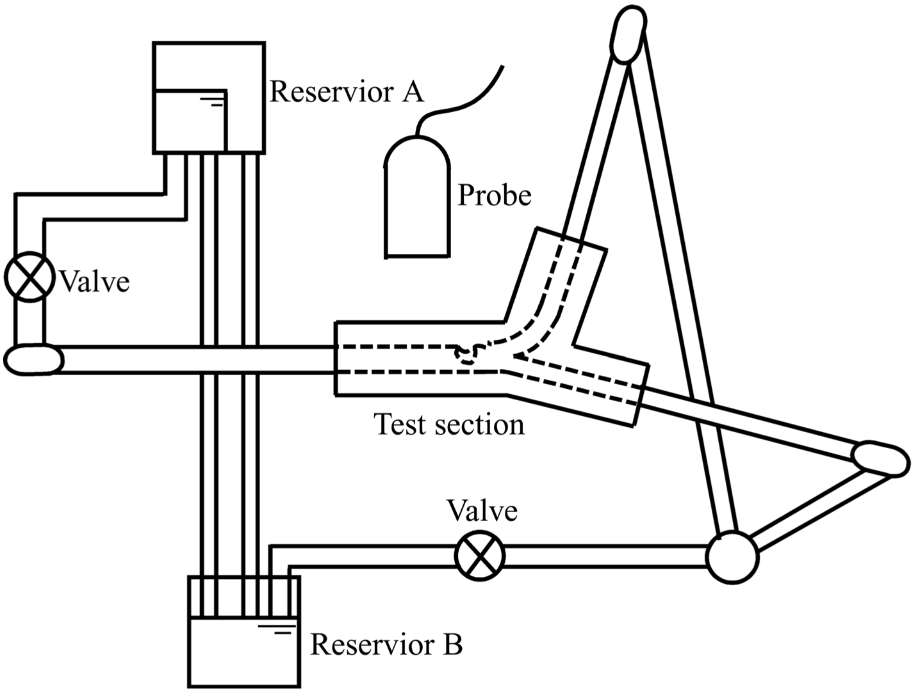

Fig. 5-3 Experimental apparatus for measuring the velocity field. In inspiratory flow the reservoir A was used as an upper reservoir and the other reservoir B was as a lower one, and in the expiratory flow vice versa.

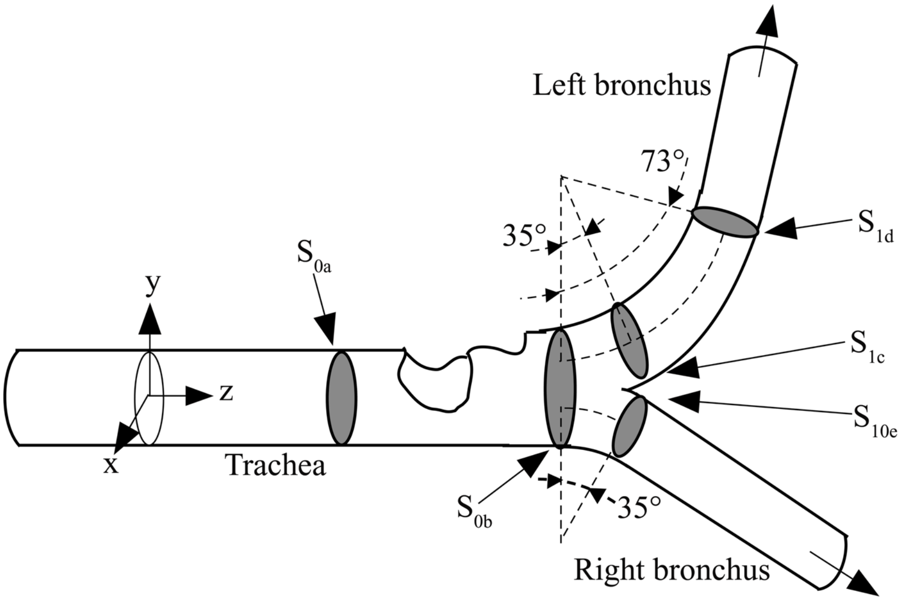

Fig. 5-4 Axial position for the velocity measurement. X direction is the smooth muscle side.

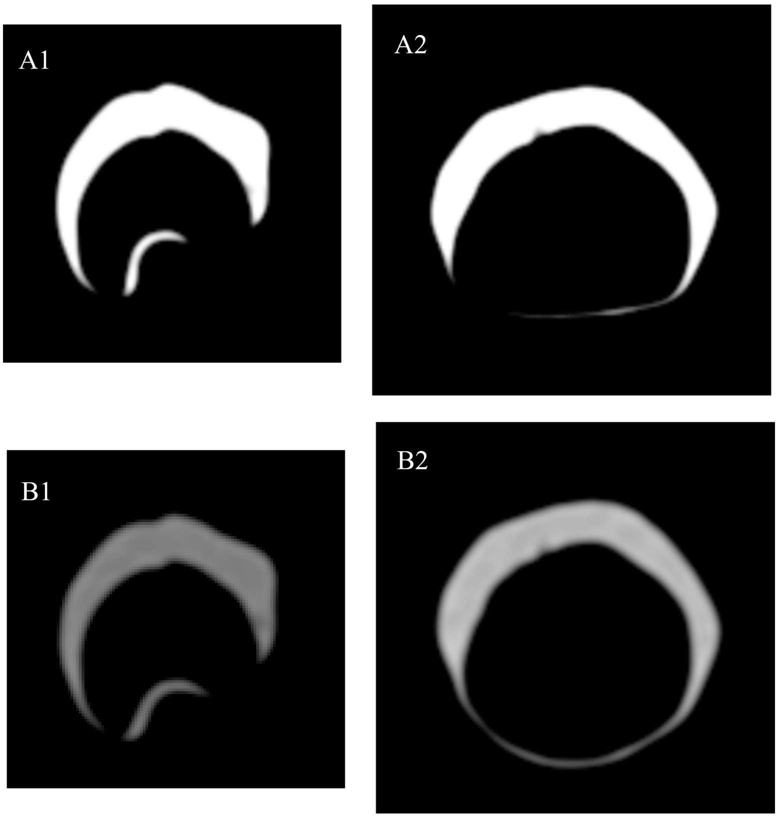

Fig. 5-5 Photographs of cross-sections at (1) the stenosis and (2) station S_{0b} of the flexible model for a transmural pressure at the entrance of the test section at (A) 0 cmH_2O and (B) $3cmH_2O$. Top: the side of the cartilage rings, Bottom: the side of the smooth muscle.

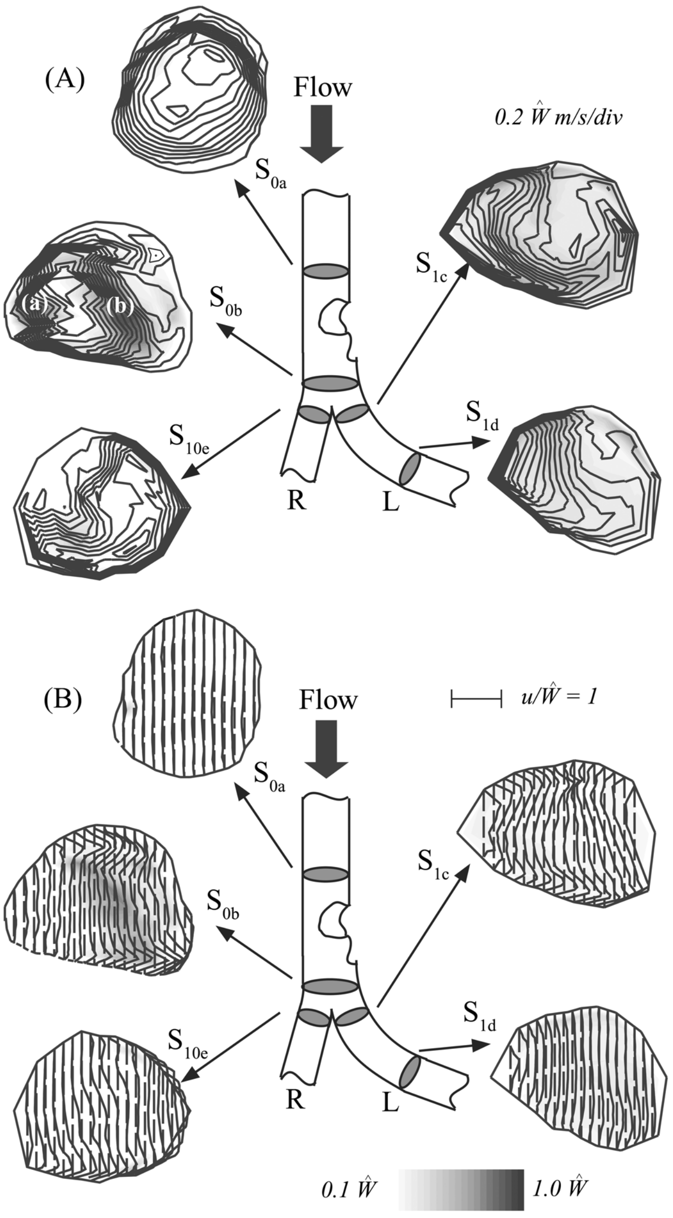

Fig. 5-6 Inspiratory flow in the rigid model: (A) Axial velocity contours and axial turbulence intensity distributions (increment between contour lines is $w/\hat{W} = 0.2$), and (B) secondary velocity profiles and secondary turbulence intensity distributions (the scale bar is ($u/\hat{W} = 1$). The smooth muscle side was shown at the bottom side of all profiles. "L" means the left main bronchus and "R" means the right bronchus. Thin lines at Station S_{0b} in (A) shows the recirculation zone. Turbulence energy was produced at the boundary layer (a) and the free shear layer at station S_{0b} (b).

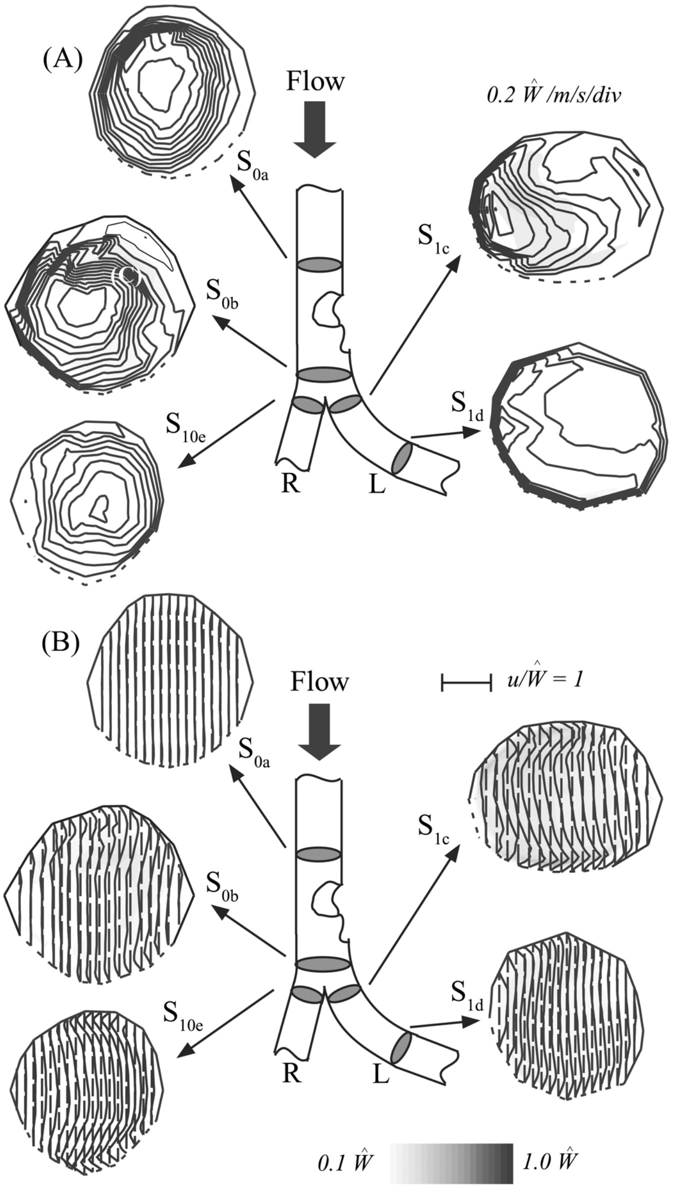

Fig. 5-7 Inspiratory flow in the flexible model: (A) Axial velocity contours and axial turbulence intensity distributions, and (B) secondary velocity profiles and secondary turbulence intensity distributions. Dotted lines, which are the bottoms of the all profiles, show smooth muscle. Thin lines at Station S_{0b} in (A) shows the recirculation zone. Turbulence energy was produced at the free shear layer at station S_{0b} (c).

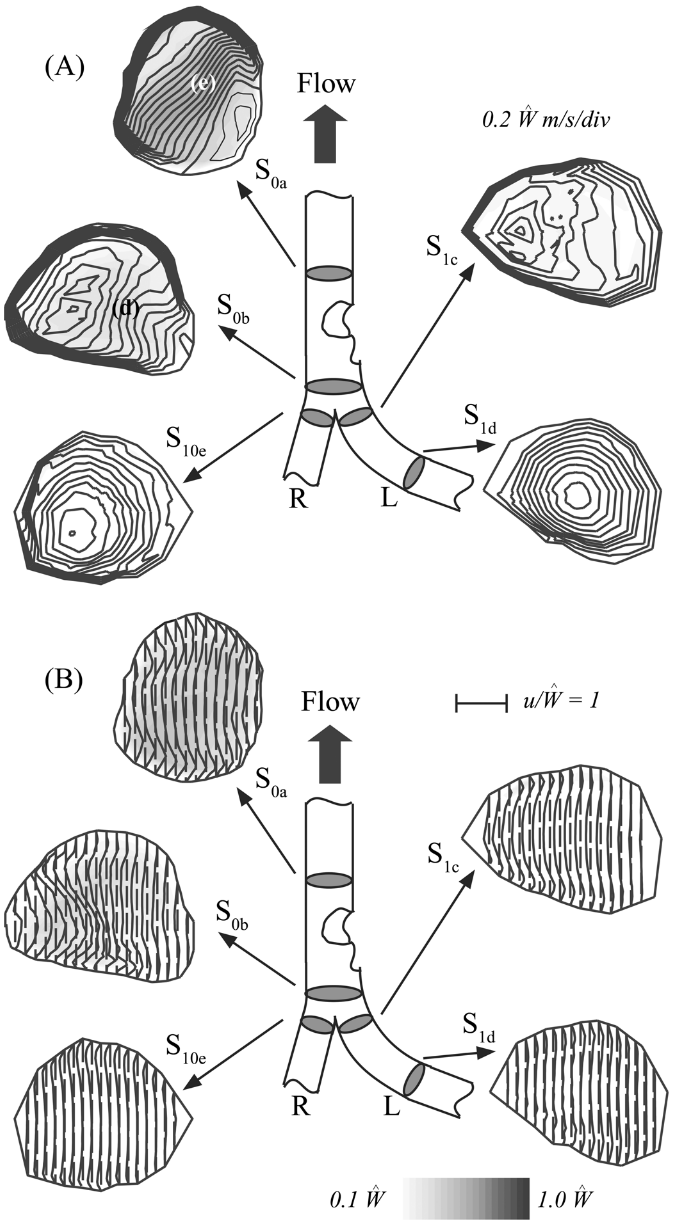

Fig. 5-8 Expiratory flow in the rigid model: (A) Axial velocity contours and axial turbulence intensity distributions, and (B) secondary velocity profiles and secondary turbulence intensity distributions. The smooth muscle side was shown as the bottom side of all profiles. Thin lines at Station S_{0a} in (A) shows the recirculation zone. Turbulence energy was produced at the boundary layer at station S_{0b} (d) and the free shear layer at station S_{0a} (e).

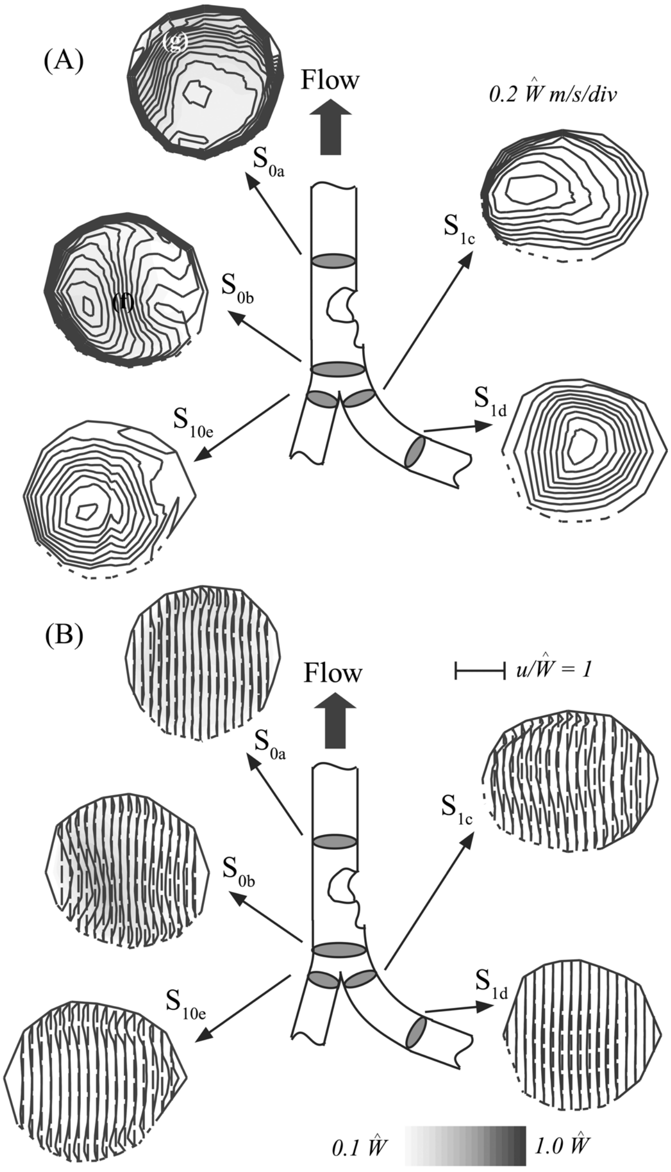

Fig. 5-9 Expiratory flow in the flexible model: (A) Axial velocity contours and axial turbulence intensity distributions, and (B) secondary velocity profiles and secondary turbulence intensity distributions. Dotted lines, which are the bottoms of the all profiles, show smooth muscle. The turbulence energy was produced much at the boundary layer at station S_{0b} (f) and the free shear layer at station S_{0a} (g).

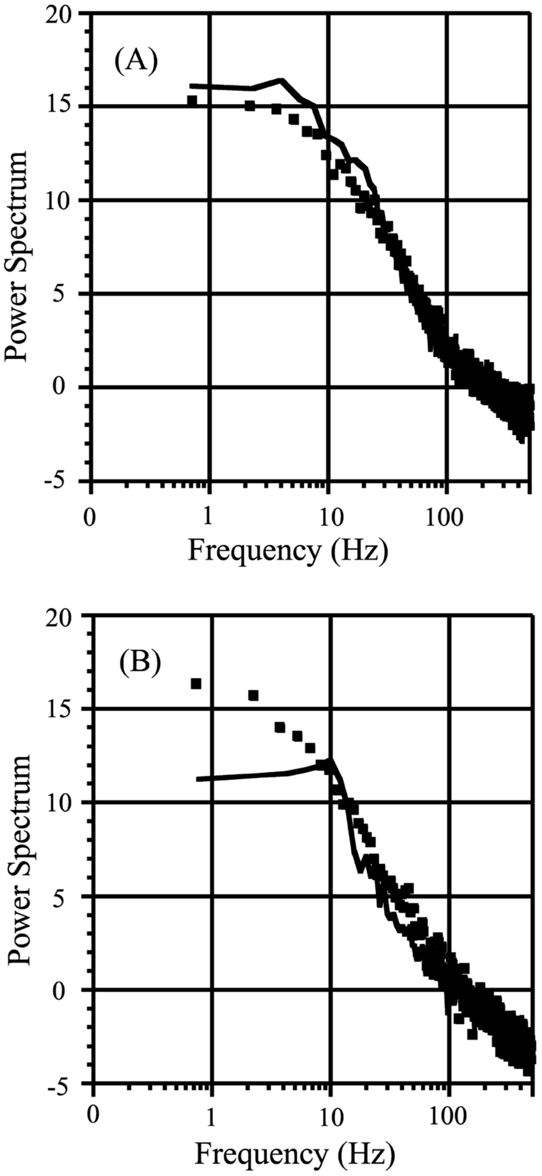

Fig. 5-10 Power spectrum of axial velocity at locations of strong turbulence intensity during inspiratory flow (solid lines) and expiratory flow (dotted lines) for the (A) rigid model and (B) flexible model.

Reference

Dragon CA, and Grotberg JB. Oscillatory flow and mass transport in a flexible tube. J Fluid Mech 231, 135-155, 1991.

Forgacs P. The functional basis of pulmonary sounds. Chest 73, 399-405, 1978.

Gavriely N, Palti U, Alroy G., and Grotberg JB.Measurement and theory of wheezing breath sounds. J Appl Physiol 57, 481-492, 1984

Gavriely N, Kelly KB, Grotberg JB, and Loring SH. Forced expiratory wheezes are a manifestation of airway flow limitation. J Appl Physiol 62, 2398-2403, 1987.

Gavriely N, and Grotberg JB. Flow limitation and wheezes in a constant flow and volume lung preparation. J Appl Physiol 64, 17-20, 1988.

Gavriely N, Shee TR, Cugell DW, Grotberg JB. Flutter in flow-limited collapsible tube; a mechanism for generation of wheeze. J Appl Physiol 66, 2251-2261, 1989.

Horsfield K, Dart G., Olson DE, Filly GF, Cumming G., Models of the human bronchial tree. J Appl Physiol 31(2), 207-217, 1971.

Kraman SS, and Wang PM. Airflow-generated sound in a hollow canine airway cast. Chest 97, 461-466, 1990.

Kraman SS, Pasterkamp H, Kompis M, Takase M, and Wodicka GR. Effects of breathing pathways on tracheal spectral features. Respir Physiol 111, 295-300, 1998.

Malmberg LP, Sorva R, and Sovijärvi ARA. Frequency distribution of breath sounds as Indicator of bronchoconstriction during challenge test in asthmatic children. Pediatr Pulmonol 18, 170-177, 1994.

Malmberg, LP, Pesu, L, and Sovijärvi, ARA, Significant differences in flow standardized breath sound spectra in patients with chronic obstructive pulmonary disease, stable asthma, and health lungs. Thorax 50, 1285-1291, 1995.

Nakamura T, Nakano H, Maekawa J. and Narita N. Influence of Posture and Breathing Root on

Power Spectra of Tracheal Breath Sound. In Proceeding of 19th Lung Sounds Research Conference [in Japanese], Tokyo, 52-57, 1995.

Pedley TJ. Pulmonary Fluid Dynamics. Ann. Rev. Fluid Mech 9, 229-274, 1977.

Sanchez I, Powell RE, and Pasterkamp H. Wheezing and airflow obstruction during methacholine challenge in children with cystic fibrosis and in normal children. Am Rev Respir Dis 147, 705-709, 1993.

Sano K, Nakano H, Maekawa J, and Narita N. Breath sound intensity in patient with emphysema. –relationship between power spectra of breath sound intensity and inspiratory flow rate-. In Proceeding of 19th Lung Sounds Research Conference [in Japanese] Tokyo, 66-71, 1995.

Schlichting H. Boundary layer theory. (7ed ed.) MacGraw-Hill. New York, 1979.

Sreenivasan KR, and Strykowski PJ. Stabilization effects in flow through helically coiled pipes. Expts Fluids 1, 31-36, 1983.

Stein PD, Walburn FJ, and Blick EF, Damping effect of distensible tubes on turbulent flow: Implications in the cardiovascular system. Biorheology 17, 275-281, 1980.

Takase M, and Pasterkamp H. Detection of Mild Airway Narrowing in Children Based on Spectral Characteristic on Normal Lung Sounds. Therapeutic Research [in Japanese] 18, 3015-3022, 1997.

Tanaka G, Ogata T, Oka K, and Tanishita K. Spatial and temporal variation of secondary flow during oscillatory flow in model human central airways. ASME J Biomech Eng 121, 565-573, 1999.

Yoganathan AP, Ball J, Woo YR, Philpot EF, and Sung HW. Steady flow velocity measurements in a pulmonary artery model with varying degrees of pulmonic stenosis. J Biomech 19, 129-146, 1986.

Zhao Y, and Lieber BB, Steady inspiratory flow in a model symmetric bifurcation. ASME J Biomech Eng 116, 488-496, 1994.

Chapter 6

Conclusion

This thesis focused on the localized compliance of airways, especially trachea and small airways, and effects of airway compliance to respiratory flow of patient having stenosis. Localized compliance of trachea affects airway resistance and that of small airways has clinical implication. In chapter 2, tracheal compliance was analyzed. In this chapter, Young's modulus of cartilage rings (E_{TC}) and smooth muscle (E_{TS}) were evaluated to analyze flow structure of patient with tracheostenosis in chapter 5. E_{TC} and E_{TS} were 5.8 ± 2.9 MPa and 0.65 ± 0.32 MPa. In chapter 3, a two-step method was developed to visualize small airways (~ 150 μm) in detail by staining the lung tissue with a radiopaque solution and then visualizing the tissue with a cone-beam microfocal X-ray CT system under "near" physiological condition. This method was the first reported method to visualize small airways in lung parenchyma without fixation. In chapter 4, using this novel visualization technique, the morphometric changes and the localized compliance of small airways was evaluated. The small airways did not behave homogenously. And the small airways were generally compliant with increasing $\boldsymbol{Z}$ and exhibited hysteresis in their diameter behavior. Compared with airways at lower $\boldsymbol{Z}$, those at higher $\boldsymbol{Z}$ deformed at a lower pressure. The Small airways deformed remarkably and inhomogenously during respiration. In transitional and respiratory zones (Fig. 1-3) the airflow is approximately zero and gas transport is traditionally dominated by simple diffusion. However, in chapter 4, the dramatic deformation of small airways during inflation and deflation process may promote complicated diffusion. Tsuda et al. (2002) visualized rat lungs in rhythmically ventilation and demonstrated the complicated mixing (Fig. 6-1 and 6-2). In chapter 5, the respiratory flow of patient with tracheostenosis was clarified to effect localized compliance of trachea. Turbulence production rate decreased in compliant airway model much than in rigid airway model, especially at the more compliant wall, because the cross sections increased due to the pressure. Moreover the possible mechanism of wheeze generation was investigated. Turbulence induced at stenosis possibly contributes to wheeze generation at low flow.

The localized compliance of healthy small airways was evaluated under “near” physiological condition. The compliance abnormality (surfactant abnormality and the deposition of fibrous tissue) occurs at small airways (Fig. 1-8). Compared between localized compliance of normal and abnormal small airways (for example, asthma and acute respiratory distress syndrome), and the localized compliance will be used as a new clinical index. And recently medical imaging device, X-ray CT and MRI have progressively come into worldwide, and the powerful synchrotron radiation, which is provided by third-generation radiation facility, such as SPring-8 (http://www.spring8.or.jp), is useful to visualize and analyze soft tissue. In chapters 3 and 4, lung tissue is stained by radiopaque solution to visualize the small airways. Using μ-CT at SPring-8, small airways and alveoli will be analyzed under physiological condition and the novel phenomena and clinical index will be proposed.

Recently the quantitative and integrated description of the functional behavior of the physiological state of an individual or species, such as “PHYSIOME (http://www.physiome.org)” has been studied. The lung is for gas exchange. Air inspired from nose is transported to alveolar by many mechanisms, such as mixing and diffusion. Previous studies were interested in pulmonary dynamics in simple (Nishida et al. 1997; Fujioka et al. 2001) or multiple bifurcation (Tanaka et al. 1999). However the airway itself consists of many airway segments with continuous branching. Tawhai et al. (2000) proposed the generation algorithm produced conducting airway model with branching characteristic which is close to previous reports (Horsfield and Cumming, 1967) and shown the three-dimensional model of conducting airways. Kitaoka et al. (1999 and 2000) also developed three-dimensional model of human airway tree and pulmonary acinus, and simulate lung ventilation in these models using supercomputer network "BioGrid (http://www.biogrid.jp)". And O_2 transported in alveolar is absorbed in the pulmonary capillary by simple diffusion and carried by hemoglobin, and finally move between the systemic capillary blood and the tissue cells by simple diffusion. To analyze the mechanics of gas exchange, the experimental information into quantitative descriptions of the functioning of lung such, as "morphometry and compliance", will be integrated under physiological condition.

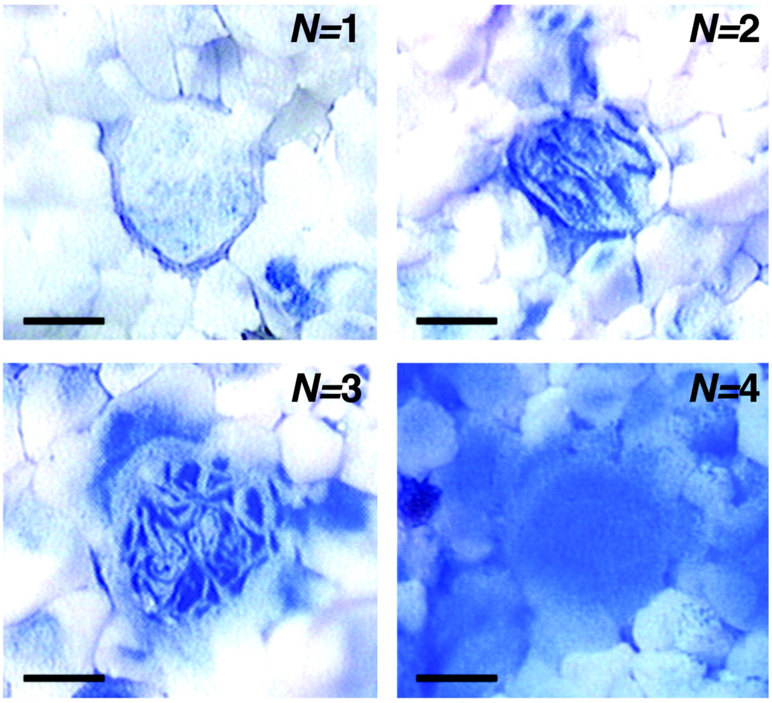

Fig. 6-1 Typical mixing pattern of two colors observed in approximately 200 mm acinar airways of adults rat after ventilatory cycles of N = 1, 2, 3 and 4. Bars = 100 μm. (Tsuda et al., 2002)

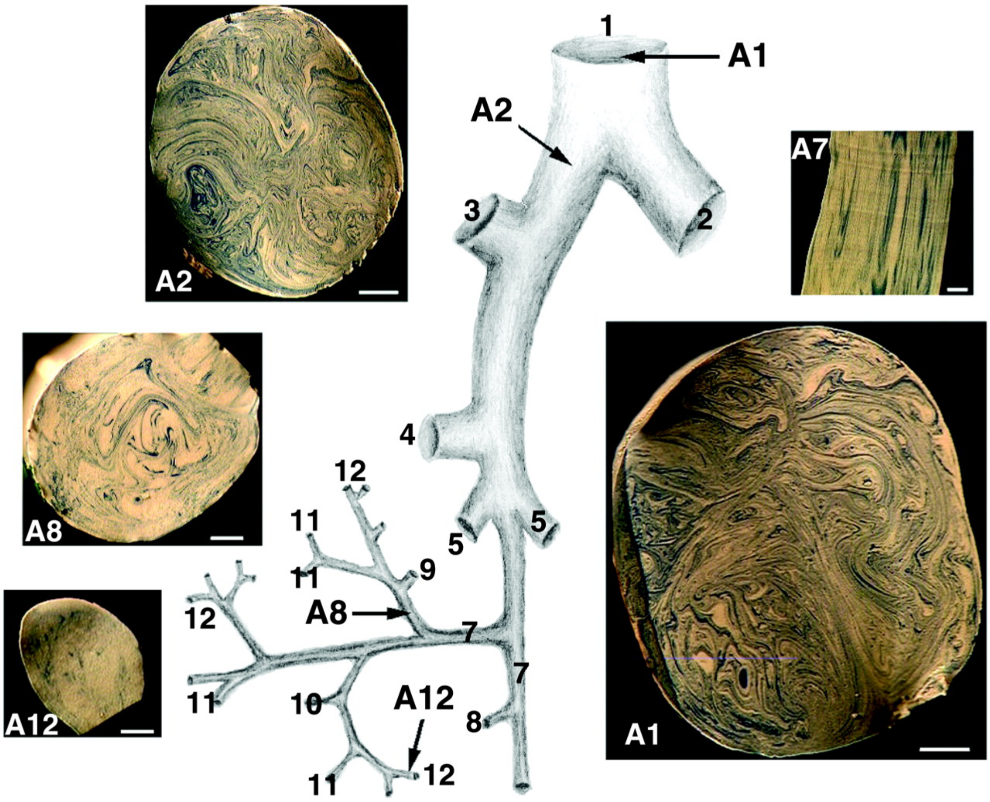

Fig. 6-2 Typical flow patterns observed on airways cross-sections at different locations of adults rats after one vetilatory cycle. Images A1, A2, A8 and A12 show patterns on the transverse section, and A7 shows longitudinal section. Bars at A1 and A2 = 500 μm, at A8 = 200 μm, at A7 and A12 = 100 μm. (Tsuda et al., 2002)

Reference

Fujioka H, Oka K, Tanishita K. Oscillatory flow and gas transport through a symmetrical bifurcation. ASME J Biomech Eng 123, 145-153, 2001.

Kitaoka H, Takaki R and Suki B. A three-dimensional model of the human airway tree. J. Appl. Phsiol 87, 2207-2217, 1999.

Kitaoka H, Tamura S and Takaki R. A three-dimensional model of the human pulmonary acinus. J. Appl. Phsiol 88: 2260-2268, 2000.

Horsfield K, and Cumming G. Angles of branching and diameters of braches in human bronchial tree. Bull Math Biophys 29, 245-259, 1967.

Nishida M, Inaba Y, Tanishita K. Gas dispersion in a model pulmonary bifurcation during oscillatory flow. ASME J Biomech Eng 119, 309-16, 1997.

Tanaka G, Ogata T, Oka K, and Tanishita K. Spatial and temporal variation of secondary flow during oscillatory flow in model human central airways. ASME J Biomech Eng 121, 565-573, 1999.

Tawhai MH, Pullan AJ, and Hunter PJ. Generation of an anatomically based three-dimensional model of the conducting airways. Ann Biomed Eng 28(7), 793-802, 2000.

Tsuda A, Rogers RA, and Hydon PE. Chaotic mixing deep in the lung. Proc Natl Acad Sci U S A. 99(15), 10173-10178, 2002.

BIBLIOGRAPHY

Publications

1. Toshihiro SERA, Sunao SATOH, Hirohisa HORINOUCHI, Koichi KOBAYASHI, and Kazuo TANISHITA, "Respiratory Flow in a Realistic Tracheostenosis Model", ASME Journal of Biomechanical Engineering, 125(4), 461-471, 2003.

2. Toshihiro SERA, Hideki FUJIOKA, Hideo YOKOTA, Akitake MAKINOUCHI, Ryutaro HIMENO, Robert C. SCHROTER, and Kazuo TANISHITA, "Three-Dimensional Visualization and Morphometry of Small Airways from Microfocal X-ray Computed Tomography", Journal of Biomechanics, 36(11), 1587-1594, 2003.

3. Toshihiro SERA, Hideki FUJIOKA, Hideo YOKOTA, Akitake MAKINOUCHI, Ryutaro HIMENO, Robert C. SCHROTER, and Kazuo TANISHITA, "Localized Compliance of Small Airways in excised rat lungs using Microfocal X-ray Computed Tomography", Journal of Applied Physiology, [in press]

Review

1. Toshihiro SERA, and Kazuo TANISHITA, "Anatomical Aspects of Airway Flow and Gas Transport in the Pulmonary System." Medical Imaging Technology, 20(6), 654-659, 2002. [in Japanese]

Proceedings (International)

1. Toshihiro SERA, Sunao SATOH, Hirohisa HORINOUCHI, Koichi KOBAYASHI, and Kazuo TANISHITA, "The Inspiratory and Expiratory Flow in Distensible Tracheostenosis Model", *2000 ASME International Mechanical Engineering Congress and Exposition*, ORLANDO (FLORIDA), November, 2000.

2. Toshihiro SERA, Yuji HASEGAWA, Robert. C. SCHROTER, and Kazuo TANISHITA, "Three-Dimensional Analysis of Small Airway with X-Ray Micro-CT", *ASME 2001 Bioengineering Conference*, SNOWBIRD (UTAH), July, 2001.

3. Toshihiro SERA, Hideki FUJIOKA, Hideo YOKOTA, Akitake MAKINOUCHI, Ryutaro

HIMENO, Robert C. SCHROTER and Kazuo TANISHITA, "NEW METHOD OF THREE-DIMENSIONAL IMAGING OF SMALL AIRWAYS IN RATS WITH X-RAY MICRO-CT", *Forth World Congress of Biomechanics*, CALGARY (CANADA), August, 2002.

4. Toshihiro SERA, Hideki FUJIOKA, Hideo YOKOTA, Akitake MAKINOUCHI, Ryutaro HIMENO, Robert C. SCHROTER and Kazuo TANISHITA, "Three-dimensional visualization and morphometry of small airways from microfocal x-ray computed tomograpy", *ASME 2003 Bioengineering Conference*, Miami (FLORIDA), July, 2003.

5. Toshihiro SERA, Hideki FUJIOKA, Hideo YOKOTA, Akitake MAKINOUCHI, Ryutaro HIMENO, Robert C. SCHROTER and Kazuo TANISHITA, "Morphometric changes of small airways using microfocal x-ray computed tomograpy", *The first Asian Pacific Conference on Biomechanics*, Osaka, March, 2004.

Proceedings (Japanese)

1. Toshihiro SERA, Sunao SATOH, Hirohisa HORINOUCHI, Koichi KOBAYASHI, and Kazuo TANISHITA, "The respiratory flow in distensible tracheostenosis model.", JSME The 12th Bioengineering Conference, Ishikawa, January, 2000.

2. Toshihiro SERA, Sunao SATOH, Hirohisa HORINOUCHI, Koichi KOBAYASHI, and Kazuo TANISHITA, "The respiratory flow in distensible tracheostenosis model.", The 39th Annual Conference of Japanese Society for Medical and Biological Engineering, Tokyo, May, 2000.

3. Toshihiro SERA, Sunao SATOH, Hirohisa HORINOUCHI, Koichi KOBAYASHI, and Kazuo TANISHITA, "The Measurement of the Respiratory Flow in a Tracheostenosis Model (Modeling of Distensibilty and CT images).", 2000 meetings of Japan Society of Fluid Mechanics, Kyoto, July, 2000.

4. Toshihiro SERA, Sunao SATOH, Hirohisa HORINOUCHI, Koichi KOBAYASHI, and Kazuo TANISHITA, "The respiratory flow in distensible tracheostenosis model.", Mechanical Engineering Congress 2000 Japan, Nagoya, August, 2000.

5. Toshihiro SERA and Kazuo TANISHITA, "Three-dimensional analysis of small airway with X-ray micro-CT.", JSME The 13th Bioengineering Conference, Sendai, January 2001.

6. Toshihiro SERA, Yuji HASEGAWA, Robert. C. SCHROTER, Kazuo TANISHITA,

"Three-dimensional analysis of small airways with x-ray micro-CT.", The 40th Annual Conference of Japanese Society for Medical and Biological Engineering, Nagoya, May, 2001.

7. Toshihiro SERA, Hideki FUJIOKA, Hideo YOKOTA, Akitake MAKINOUCHI, Ryutaro HIMENO, Robert C. SCHROTER and Kazuo TANISHITA, "Three-dimensional analysis of small airway with X-ray micro-CT.", The 14th Bioengineering Conference, Tokyo, March, 2002.

8. Toshihiro SERA, Hideki FUJIOKA, Hideo YOKOTA, Akitake MAKINOUCHI, Ryutaro HIMENO, Robert C. SCHROTER and Kazuo TANISHITA, "Three-dimensional structure of small airways using micro-CT.", The 41th Annual Conference of Japanese Society for Medical and Biological Engineering, Kyoto, May, 2002.

9. Toshihiro SERA, Hideki FUJIOKA, Hideo YOKOTA, Akitake MAKINOUCHI, Ryutaro HIMENO, Robert C. SCHROTER and Kazuo TANISHITA, "New method of three-dimensional imaging of small airways with x-ray micro-CT.", The 25th Japanese Society of Biorheology, Nagano, June, 2002.

10. Toshihiro SERA, Hideki FUJIOKA, Hideo YOKOTA, Akitake MAKINOUCHI, Ryutaro HIMENO, Robert C. SCHROTER and Kazuo TANISHITA, "Three-dimensional structure of small airways using micro-CT", The 16th Autumn Conference of Japanese Society for Medical and Biological Engineering, Fukuoka, October, 2002.

12. Toshihiro SERA, Hideki FUJIOKA, Hideo YOKOTA, Akitake MAKINOUCHI, Ryutaro HIMENO, Robert C. SCHROTER and Kazuo TANISHITA, "Effect of lung inflation and deflation on morphometry of small airways", The 42th Annual Conference of Japanese Society for Medical and Biological Engineering, Sapporo, June, 2003.